Dissertation

Optimization of surface area and conductivity of Nb-doped titanium oxides as carbon-free cathode supports in PEFCs

PEFC 用カーボンフリーカソード担体としてのニオブドープ酸化チタンの表面積と導電率の最適化

September 2022

Yongbing MA

马永炳

Optimization of surface area and conductivity of Nb-doped titanium oxides as carbon-free cathode supports in PEFCs

(PEFC 用カーボンフリーカソード担体としてのニオブドープ酸化チタンの表面積と導電率の最適化)

September 2022

Graduate School of Engineering Science

Yokohama National University

Yongbing MA

马永炳

Contents

Chapter 1

General introduction

1.1 Resources and environment

Energy has become the key to the development of human society and the progress of civilization. Woods, hays, and other combustibles which are easily accessible from nature were used for cooking, heating, and other essential purposes by primitive humans. With advances in geology and mining technology, coal has a much higher energy density than traditional animal and plant fuels.

Generally, Karl Marx recognized positive feedback between advanced productivity and technological progress. [1, 2] In 1776, James Watt improved on the Newcomen steam engine with his Watt steam engine, marking the Industrial Revolution's arrival. Until the 1830s, one worker's output was increased around 500 times in mechanized cotton spinning [3]; the needed fuel decreased to 1/5 - 1/10 due to the efficiency of steam energy. [4, 5] In the 1780s, the first transformation was that coal became the largest share of primary energy instead of the woods. [6] In 1876, Nicolaus Otto invented the Neuer Otto-Motor, which used gas as fuel and made the efficiency improvements to 12%, this cycle named as Otto cycle. Then, in 1885, Gottlieb Wilhelm Daimler invented the first gasoline engine. It was one of the features of the Second Industrial Revolution. The second industrial revolution saw another leap forward in manufacturing, such as the construction of railways, large-scale steel production, the widespread use of machinery, the general use of the telegraph, oil, and the beginning of electrification. [7] The second transformation was that the share of petroleum and gas in the primary energy mix improved rapidly, and instead, coal was the most prominent part in 1965. [6] Herein, in the second transformation, the primary energy source is transferred from coal to oil and natural gas.

With the development of the social economy and further improvement of efficiency, the production mode of human society is bound to undergo the third transformation: from traditional fossil fuel to non-fossil new energy is becoming inevitable. Specifically, with the development of information technology, people's demand for electricity is gradually increasing. The total power generation in 1985 was 9826 TWh, of which the proportion of oil, gas, and coal were 1108.76, 1422.36, and 3748.31 TWh, respectively; in 2021, the power generation was 27520.52 TWh, of which the proportion of oil, gas, and coal were 851.7, 10042.2 and 6098.08 TWh,

respectively. [8, 9] A lot of interesting facts could be found in those data. First, in the past 36 years, the power generation increased 2.8 times. This is in line with the global economic development over the past century. Then, in the part of primary energy, oil is decreasing, the position of natural gas is increasing rapidly, and the increment of coal is less than the increment of total power generation, which is related to the reduction of harmful NO_x, SO_x emissions as well as international energy prices, market supply stability. Finally, although the increment of total power generation is enormous, the primary part is decreased. It benefits from renewable energy development and the efficiency improvement of traditional power generation methods, like ultra-supercritical. The importance of non-primary energy is steadily increasing.

With industrialization, various greenhouse or harmful gas emissions increased very quickly and massive, such as NO_x, SO_x, CO_2, CH_4, HFCs, etc. Since the Industrial Revolution, within the unreasonable time of 300 years, greenhouse gas / harmful gas emissions have been several times higher than before. Even worse, the emission still increases with a high growth rate. For example, the CO_2 emission from fossil fuels was 27869 Mt in 2007 and expanded to 30127 Mt in 2017 [8, 10, 11]. The growth rate in 10 years is 8.1%, which is obviously a dangerous acceleration. On the other hand, based on the IPCC-AR5 report, it could be easily found that the CO_2 emission is more about 5682 Mt than the natural absorption amount of 24445 Mt, which means that the carbon cycle balance has been broken.

In Intergovernmental Panel on Climate Change Fifth Assessment Report (IPCC-AR5), they reported the Representative Concentration Pathways (RCPs) model, which is predicted the impact of different conditions of greenhouse gas emissions on the global environment by the radiative forcing value in 2100 (1.9, 2.6, 3.4, 4.5, 6, 7 and 8.5, W/m^2, respectively. In the model, several possible scenarios for greenhouse gas emissions are assumed. From RCP 1.9 to RCP 8.5, the number represents their atmospheric concentrations. Herein, the RCP 3.4 was considered the most reasonable prediction[12], although it is still a strict emission target. In addition, according to the emission reduction plans announced by major countries, RCP 4.5 is also a possible model. The emissions peak would be reached around 2040, which would cause the temperature to rise 2 – 3 Celsius, and many plants and animals will be hard to survive at RCP 4.5 or higher RCPs [11]. The deterioration of the environment is affecting the earth's atmosphere. Sea levels are rising,

extreme climates are increasing, and the living environment of humans and other species is deteriorating. It is increasingly necessary and urgent to reduce greenhouse gas emissions. According to NASA's speculative data [13], if the RCP 4.5 forecast model can be strictly implemented, the global sea level rise will be controlled within two meters, which is still a grim situation for some regions. Meantime if emissions cannot be effectively controlled, the average sea level rise will exceed two meters around 2180 and about 4.7 meters in 2300. This will lead to extremely serious consequences. For example, the area near Yokohama Station with an average altitude of about two meters will disappear, and the coastal industrial area near Isogo will also be seriously threatened or even submerged.

Meanwhile, from the perspective of energy security and stability, renewable energy development is becoming more and more necessary. From the 1973 oil crisis, 1979 oil crisis,1990 oil price shock, etc., to the 2022 Russo-Ukrainian War, which is still ongoing, international energy prices are prone to significant fluctuations due to external factors such as wars. Since the 2022 Russo-Ukrainian War, the global crude oil price has remained above 100 dollars per barrel for a long time; it increases the cost of production and living in many countries and even threatens the security of the energy supply chain.

Not only the environment but energy security problems. To defend the development of human civilization, developing renewable energy is necessary and urgent.

1.2 Renewable energy

Primary energy is energy harvested from nature directly without the human conversion process. [14] In general, there are two primary energy categories: non-renewable energy, like oil, coal, and natural gas, and the other is renewable energy, such as hydro and biofuels. Renewable could be replenished on the scale of human development. It is trusted that resource reserves of renewable energy are never-ending and can be automatically regenerated or recycled under certain conditions. In a broad sense, it includes some traditional, long-term use in human history ways such as faggot and animal power, etc. In a narrow sense, now renewable energy mainly refers to some means of power generation in modern society, like hydropower, wind power, solar

power, bioenergy, geothermal energy, etc. As a common feature of most renewable energy, renewable energy often has the characteristics of low carbon emission or even zero carbon emission. This is of great significance for sustainable social and economic development, reducing environmental pollution, and even diversifying energy sources.

Basic on the BP Statistical Review of World Energy [8], in 2019, there is approximately 37% of electricity generation from low-carbon sources, including nuclear energy, hydropower, and other renewables. Such data is undoubtedly a positive signal. However, there is another aspect to consider, for the total energy, which included electricity, transport, and heat, the part of low-carbon sources was reduced to 16%. We need to notice that transport and heating are harder to decarbonize, which means that the low-carbon electricity will be more critical. Many energy needs that rely on traditional fossil fuels can be replaced by clean electricity, e.g., electric vehicles and electric heating. However, we need to notice that used as energy sources are just only part of the use of fossil fuels. They are also indispensable raw materials in modern chemistry and industry. [16] This means that the use of fossil fuels will not objectively drop to zero.

Unlike fossil energy, which can be conveniently stored in reserve and used on-demand at any time, hydro power, wind power, and solar power are deeply affected by dry& wet seasons, wind speed and direction, sunlight time, etc. Therefore, the electricity that comes from renewable energy is hard to use. Although some energy conversion means can regulate the supply of renewable energy, such as pumped-storage hydroelectricity, the amount and time of power generation that can be adjusted by pumped-storage hydroelectricity are very limited. It is unrealistic to build a giant chemical battery for electricity to store energy like an oil tank. [16] As a solution, more extensive and more efficient energy conversion facilities have been built, such as compressed air energy storage in 300 MWh storage capacity Jintan salt caverns in Jiangsu, China [17]; 40 GWh storage capacity Fengning Pumped Storage Power Station in Hebei, China. [18] Meantime, another way to address this problem is using hydrogen as an intermediary to connect the power generation, storage, and consumer. Thus, hydrogen is on the fortune to the future.

1.3 Hydrogen energy

Hydrogen is the lightest element by relative atomic mass in the world, which is a colorless, odorless, tasteless, non-toxic, explosive, and chemical element in the universe. [19] The most basic reaction of hydrogen is the combustion reaction with air/oxygen, which is expressed as $2H_2(g) + O_2(g) \rightarrow 2H_2O(l) + 572$ kJ; the only product is water. Humans have been using hydrogen for nearly 200 years. Döbereiner's lamp uses zinc metal and sulfuric acid to produce hydrogen [20]. In the early 20th century, hydrogen was widely used in airships and other aircraft, and the Zeppelins had their maiden flight in 1900 [21]. In 1971, the nickel-hydrogen battery was patented by Alexandr Ilich Kloss and Boris Ioselevich Tsenter in the United States [22]. Hydrogen is also widely used in the petrochemical industry, rocket fuel, semiconductor industry, etc. Hong Yong Sohn et al. reported that with the metallurgical hydrogen production by flash ironmaking, the CO_2 emissions would be reduced to one forty of avg. blast furnace. [23, 24] It could be found that hydrogen has been widely used in many fields. Although hydrogen forms explosive mixtures with air in concentrations from 4 – 74%[25], hydrogen remains relatively safe due to its minimal mass and rapid dissipation in open spaces, and it makes hydrogen has huge potential as an energy source in the next generation.

Nowadays, hydrogen production has increased three times since 1975, and in 2015, the global demand for pure hydrogen has reached over 70Mt, of which 36 Mt accounted for refining, 31.9 Mt accounted for ammonia, and 3.8 Mt accounted for others, respectively. [26, 27] Unfortunately, despite the strong growth in demand for hydrogen over the past half-century, hydrogen production still comes almost entirely from fossil fuels, of which 76% from gas and 23% from coal. [28, 29] Existing hydrogen production processes make the potential advantages of hydrogen in low/zero emissions not fully utilized. Meanwhile, electrolysis currently accounts for less than 2% of hydrogen production. Combined with other renewable energy generation methods such as solar energy and wind energy, water electrolysis has great potential for low-carbon hydrogen production. Water electrolysis mainly includes Alkaline Water Electrolysis (AWE), Proton Exchange Membrane Water Electrolysis (PEMWE), and Anion Exchange Membrane Water Electrolysis (AEMWE), etc. Related research has accelerated in recent years. Since the electrolysis process is artificially controllable, the electrolysis of hydrogen production as a

supplement to the unstable renewable energy for power generation is expected.

Centering on the production and utilization of hydrogen, Japan has put forward the concept of "hydrogen society".[30] As shown in Fig. 1.1, in the hydrogen society, excess electricity can be converted between electricity and hydrogen, to realize the regulation of electricity, especially renewable energy such as solar power generation whose power output is not stable. Realize a relatively stable power supply that can be adjusted on demand. In addition, hydrogen can also be used in a variety of production and life scenarios, such as polymer electrolyte fuel cell (PEFC) devices, heating, metal refining, petroleum refining, and other fields. The large-scale utilization of hydrogen is expected to reduce carbon emissions while spawning many new industries.

Herein, in power generation, hydrogen is being used as an effective emission reduction solution. In recent years, not only hybrid combustion/ dedicated combustion equipment for hydrogen but fuel cells that use hydrogen as resources has been researched. Hydrogen and ammonia could be used in power generation as a hybrid resource in gas turbines. At the low capacity factors typical of flexible power plants, hydrogen costing under 2.5 dollars per kilogram has good potential to compete. [31] In addition, similar to natural gas, hydrogen can be transported either as a gas through pipelines or as a liquid through vehicles/ships; it makes hydrogen have the advantage of rapid filling that lithium batteries have not yet achieved. Thus, the PEFC with high efficiency, zero-emission/low emission, and miniaturization, which use hydrogen as fuel, is expected to become a clean power unit for trucks, and passenger cars, ships, etc.

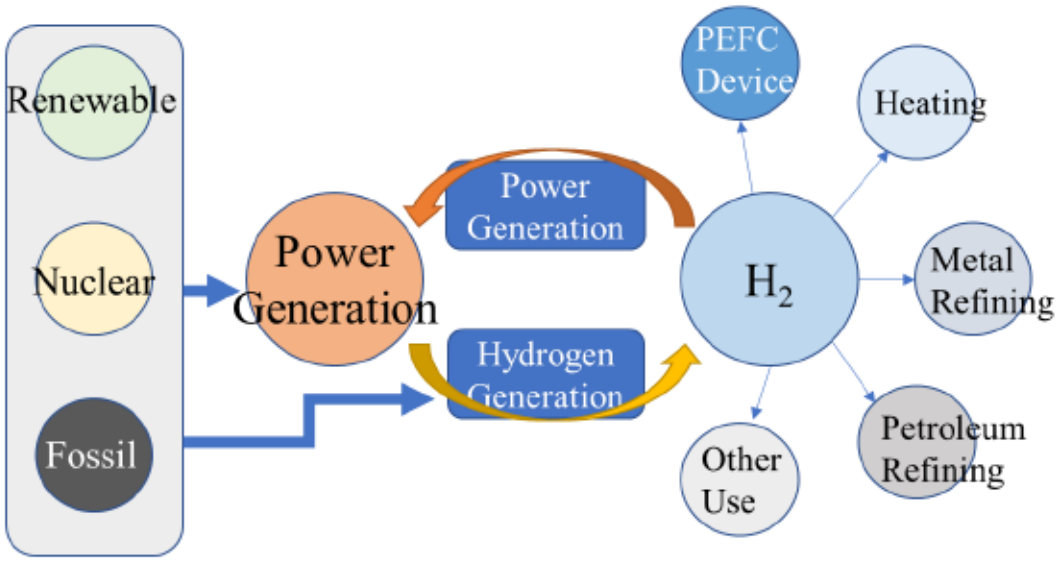

Fig. 1.1 Image of hydrogen society.

1.4 Polymer electrolyte fuel cell

1.4.1 Basic Concepts of fuel cell

The fuel cell is an electrochemical power generation device that converts chemical energy from fuel and oxidants into electric energy. Different from traditional power generation, the fuel cells are quiet, clean, and can generate electricity continuously. [32]

The reaction should be spontaneous in the fuel cell, which means that the Gibbs free energy is negative. The oxidation and reduction reactions occur on the anode and cathode, respectively. [33] The fuel cell is the reverse process of the electrolytic cell. The cathode is the positive electrode in the fuel cell system, and the anode is the negative electrode. Unlike the battery, the energy capacity is determined by the physical dimensions of the fuel storage container and the energy density of the fuel itself. Fuel cells are often used for specific applications, such as residential, vehicles, and mobile equipment, and the power output needs to vary in the range of milliwatts to megawatts. [32] The power is defined as follows:

$$\text{power} = IV_{\text{cell}} \tag{1.1}$$

Herein, the unit of power is watts (W). According to the actual application, the output power can also be expressed in watts/unit mass or watts/unit.

The performance of a fuel cell system is determined by the cell voltage and current density, while the cell voltage reflects the effectiveness of the fuel cell system in extracting the chemical energy stored in the fuel to convert it into electrical energy.

The cell voltage is obtained by the following formula:

$$V_{cell} = \Delta E_e - \eta_a - \eta_c - IR \tag{1.2}$$

ΔE_e is the equilibrium potential difference between the cathode reaction and the anode reaction. Its relationship with the Gibbs free energy of the battery's total reaction is:

$$\Delta G = -nF\Delta E_e \tag{1.3}$$

η_c and η_a are the overpotentials of the cathode reaction and the anode reaction, respectively. The last item in equation (2) is the IR drop through the cell, i.e., the ohmic drop created by the electrolyte, the electrodes, and the electrical contacts between the two electrodes.

The overpotential and IR drop must be regarded as ineffectiveness. Its role is only to reduce the proportion of chemical energy converted into electrical energy and generate heat. Therefore, the energy efficiency of a fuel cell, which is the percentage of the theoretical energy actually obtained, is defined as:

$$\text{Energy efficiency} = \frac{V_{cell}}{\Delta E_e} \times 100\% \tag{1.4}$$

Basically, in all types of fuel cells, the cathode reaction is the reduction of oxygen.

$$O_2 + 4H^+ + 4e^- \rightarrow 2H_2O \tag{1.5}$$

A variety of fuels are being considered, taking hydrogen as an example:

$$H_2 - 2e^- \rightarrow 2H^+ \tag{1.6}$$

The most attractive aspect of H_2 as a fuel for the fuel cell is that the only emission of H_2/O_2 fuel cell working is water. Zero emissions of harmful substances are generated during the entire discharge process. The disadvantage is that hydrogen is not a primary energy source that can be obtained directly and must be prepared by an inevitable chemical process.

In addition, the fuel of anode reaction is not only H_2 but also other types of fuel, such as methanol. The anode reaction that the direct oxidation of methanol:

$$CH_3OH + H_2O - 6e^- \rightarrow CO_2 + 6H^+ \tag{1.7}$$

However, a severe problem with using alcohols such as methanol, or other organic fuels, is that the reaction product will contain CO_2, which we try to reduce in the emission.

Ethanol or hydrocarbons are also usable fuels. The anode reaction process is as follows:

$$C_2H_5OH + 3H_2O - 12e^- \rightarrow 2CO_2 + 12H^+ \tag{1.8}$$

$$CH_4 + 2H_2O - 8e^- \rightarrow CO_2 + 8H^+ \tag{1.9}$$

The thermodynamically estimated maximum equilibrium voltages (ΔE_e) of H_2, CH_3OH, C_2H_5OH, and CH_4 are 1223, 1220, 1140, and 1061 mV, respectively. Table. 1.1 summarizes the total reaction and the thermodynamically estimated maximum equilibrium voltage of the above fuel in the fuel cell system. [14]

1.4.2 Classification of fuel cell

In the world, fuel cells are mainly classified into alkaline fuel cells (AFCs), phosphoric acid fuel cells (PAFCs), molten carbonate fuel cells (MCFCs), and solid oxide fuel cells (SOFCs)

according to fuel types and work methods. Polymer Electrolyte Fuel Cells (PEFCs), direct methanol fuel cells (DMFCs), etc. [32, 33]

For different types of fuel cells, in order to meet the specific work condition and environment, the catalytic performance under the conditions of use, the type of catalyst used, and the performance requirements are also different. For example, the fuel cell catalyst is not only precious metals available in alkaline fuel cells (AFCs). Non-noble metals are also available; platinum and platinum alloys can be deposited on carbon materials as catalysts, nickel-based metals can also be used as anodes, silver-based catalyst powders as cathodes, and for solid oxide fuel cells (SOFCs), cathodes. In addition to noble metals, there are ion-electron mixed conductive perovskite-type composite oxides as cathode materials. Table. 1.2 shows the classification of typical fuel cells and their main features.

PEFCs have already been applied to residential co-generation systems, trains, and vehicles such as passenger cars, buses, and trucks. However, the actual efficiency of the present PEFCs is still low because of the large overpotential at the cathode side of the oxygen reduction reaction (ORR). The operation at higher voltages owing to an enhancement of the ORR activity, as well as at higher temperatures, is expected to improve the efficiency.

It is generally believed that a catalyst with good performance should be able to support O_2 full four-electron reduction at the low overpotential (i.e., near the oxygen equilibrium potential +1.23V vs. SHE) (Equation 1.5). However, even if the best available PEFC electrocatalyst is used, the overpotential of oxygen reduction is more significant than 400 mV, so the oxygen reduction process is the principal energy efficiency loss in the current PEFC. At the same time, in the acidic environment of the PEFC, few materials can remain relatively stable without corrosion or dissolution at the oxygen electrode potential (about +0.8V vs. SHE). Therefore, in the current situation, most cathode catalysts use precious metals. The main content of recent research and development is to reduce the amount of catalyst in the cathode to ensure efficiency. [34] Since the fuel cell cathode is operated under kinetically controlled oxygen reduction conditions, the current density is proportional to the valid area of the catalyst/electrolyte interface, so the key is to increase the specific surface area of the cathode catalyst as much as possible. [35.

36]

Although the current exchange density of the oxygen reduction reaction on the smooth Pt electrode is only about 10^{-9} A cm^{-2}, the standard electrocatalyst used in the industry is still Pt. In fuel cells, the way to improve performance is to make Pt into a form with a very high specific surface area, but even so, the overpotential is still greater than 400 mV at operating current densities. Oxygen reduction overpotentials on other noble metals are even higher. [37] Compared with Pt-Cr, Pt-Fe, and Pt-Mn alloys can reduce the overpotential by about 25mV, but Fe and Mn will all be dissolved out of the alloy in an acidic medium. The interaction between the ions of metal and the sulfonate in the membrane is more proton than the protons. Thus interaction increases the IR drop of the film. [38] There are some exceptions to the Pt-Cr alloy, with a Pt : Cr ratio of 75 : 25 showing slightly better long-term stability. [39]

Table 1.1 The total reaction of the four fuels and the thermodynamically estimated maximum equilibrium voltage

Fuel	Reaction	ΔE_e/mV
H_2	$2H_2 + O_2 \rightarrow 2H_2O$	1223
CH_3OH	$CH_3OH + 3/2O_2 \rightarrow CO_2 + 2H_2O$	1220
C_2H_5OH	$C_2H_5OH + 3O_2 \rightarrow 2CO_2 + 3H_2O$	1140
CH_4	$CH_4 + 2O_2 \rightarrow CO_2 + 2H_2O$	1061

Table 1.2 Common fuel cell classifications and their main features

Type of cell	AFC	PAFC	MCFC	SOFC	PEFC	DMFC
Electrolyte	KOH solution	H_2PO_4	Molten carbonate	Solid yttria stabilized zirconia	Perfluoro sulfate film	Perfluoro sulfate film
Conductive ion	OH^-	H^+	CO_3^-	O_2^-	H^+	H^+
Operating temperature (℃)	50-100	100-200	650-700	900-1000	RT-100	RT-100
Anode fuel	H_2	H_2	H_2, CO	H_2, CO	H_2	CH_3OH
Anode oxidizer	O_2	O_2	O_2	O_2+CO	O_2	O_2

1.5 Reflections on the development of polymer electrolyte fuel cell

1.5.1 Policy guidance

Although PEFC has the advantages of fast filling and zero emissions, the development of fuel cell vehicle (FCV) has not been smooth in the past decade. With Honda announcing its withdrawal from FCVs, the fuel cell vehicle market outlook has become worrisome. There are many reasons for this problem, and I think the main ones are the following: First, the construction of hydrogen refueling stations in various countries, including Japan, is slow. The primary fuel cell vehicle in the Japanese market is a passenger car, so convenience is undoubtedly the number one priority from the customer's point of view. Second, the current hydrogen production still relies on fossil fuels as raw materials, so the low-emission/zero-emission of fuel cells is only a theoretical perspective, and the source emissions in practical use cannot be ignored. Third, in Japan, the construction of hydrogen refueling stations and hydrogen production is mainly carried out by oil companies. In the presence of essential conflicts of interest, individuals are not optimistic about the feasibility of oil companies promoting clean energy. Judging from the actual promotion in recent years, it has not achieved the expected goal of promoting hydrogen by relying on existing gas stations.

Fortunately, governments are now gradually shifting fuel cells to the commercial vehicle market. Commercial vehicles with relatively fixed routes can effectively avoid the shortcoming of the less initial distribution of hydrogen refueling stations, thereby achieving large-scale mass production and cost reduction.

As the world's major economy and carbon emitter, China's decision-making play a crucial role in reducing global emissions. In China, the fuel cell research can be traced back to 1958. The Tianjin Institute of Power Research, formerly the Ministry of Electronics Industry, first researched MCFC [40]; in the 1970s, serving the aerospace engineering, the two kinds of alkaline asbestos models were developed by the Dalian Institute of Physical Chemistry, Chinese Academy of Sciences The fuel cell system (kilowatts class; AFCs) passed the space environment simulation experiment; in 1998, Tsinghua University developed the first fuel cell vehicle in China; in 2001,

Beijing Green Energy Group cooperated with Tsinghua University and Beijing Institute of Technology to jointly develop the fuel cell is a taxi, passenger car and 12 buses of the power system. During the 2008 Beijing Olympic Games, domestic and foreign experts and the media widely acclaimed 20 fuel cell demonstration vehicles independently developed by China. During the 2010 Shanghai World Expo, 173 fuel cell vehicles jointly produced by Tongji University and domestic automobile companies were shuttled within the Shanghai World Expo. On November 13, 2015, Hydrogenic announced that it had reached an agreement with several electric vehicle integrators in China. To ease the current air pollution problem in China. At the beginning of this year, the world's first commercial-type fuel cell/super-capacitor hybrid 100% low-floor modern tram was rolled out in CRRC Tangshan Railway Vehicles Co., Ltd. Based on China's technological foundation and actual domestic market conditions, China proposed the industrialization of fuel cell vehicles: From 2006 to 2010, through demonstration operations, identified weak links, overcame technical difficulties, and conducted trials in small batches; from 2010 to 2020, To strive for mass production of fuel cell vehicles; from 2020 to 2030, the overall technical level of fuel cell vehicles in China will meet or exceed international standards, and mass production of fuel cell vehicles will be realized.

Recently. The government of Shanghai City announced the "Shanghai Fuel Cell Vehicle Development Plan." The immediate target (2017-2020). To build a domestic leading fuel cell vehicle technology demonstration city, form a clustering effect of high-quality industrial chain resources, and achieve the core key technologies of fuel cell vehicles to keep pace with the international industry. At the technical chain level, core technologies such as electric reactors, system integration and control, and key components are tracked at the international level, and key indicators align with international standards. At the industrial chain level, an industrial cluster including key components, electric stacks, system integration, test and certification services, and vehicle development will be established to gather more than 100 fuel cell vehicle-related companies and cultivate hydrogen and fuel with international influence. There is a battery technology R&D center and a fuel cell vehicle inspection and testing center. The annual output value of the fuel cell vehicle industry chain exceeds 15 billion yuan. At the demonstration operation and promotion level, the construction of 5-10 hydrogen refueling stations and 2 demonstration areas for passenger vehicles will be completed, and the scale of operation will

reach 3,000. The fuel cell bus and logistics vehicles will be actively promoted. Medium-term goals (2021-2025). Plan fuel cell vehicle demonstration areas to form a relatively complete infrastructure for the development of hydrogenation facilities in the region and explore the use of batches in areas such as public transportation, official vehicles, and commercial logistics to improve the international competitiveness of the entire industrial chain of fuel cell vehicles. At the level of the technology chain, a series of fuel cell stack products have been formed, and the fuel cell vehicle technology has been synchronized to the international level. At the industrial chain level, there are 1 vehicle company with international influence, 2-3 power system companies, 8 to 10 key component companies, and 2 of the top 3 R&D and public service agencies globally. The annual output value of the entire automobile industry chain exceeded 100 billion yuan.

At the demonstration operation and promotion level, there are 50 hydrogen refueling stations built, no less than 20,000 passenger vehicles, and no less than 10,000 other special vehicles. Based on the successful pilot operation of public transport, commercial buses, and logistics vehicles, Expand the promotion scale as appropriate. Long-term goals (2026-2030). Become an internationally influential city for fuel cell vehicle applications. The overall technology is close to the international advanced. Some technologies have reached the top international level, and the industrialization has been fully matured. It aims to achieve further market promotion for private users, promote hydrogen energy transportation, and radiate the rapid development of the national fuel cell auto industry. At the level of the technology chain, fuel cell vehicle technology and manufacturing have reached the same level in foreign countries as a whole; at the industrial chain level, the annual output value of the entire industrial chain of Shanghai's fuel cell vehicles has exceeded 300 billion yuan, driving the diversified application of fuel cell products across the country. At the demonstration operation and promotion level, Shanghai's fuel cell vehicle industry and value chain will eventually radiate across the country, bringing about future social energy and power transformation. [41]

1.5.2 Problems that may be faced in promotion

From the perspective of general consumers, the cost of use is a very important factor, which will directly affect consumers' willingness to buy. Since Japan is currently the main commercialized country for FCV passenger vehicles, the data on FCV are all from the Japanese market. In addition, due to the influence of government policies and manufacturers' strategies, the penetration rate of electric vehicles (EV) in Japan is still not high, and many problems with the large-scale popularization of new energy vehicles have not yet emerged. While China is vigorously promoting EVs, many new problems have gradually been discovered. For example, EVs have excellent acceleration, which enables ordinary drivers to obtain the acceleration experience that was originally only available in high-end sports cars. However, for ordinary drivers who lack driving high-performance vehicles, this also makes traffic accidents more likely to occur; EV battery packs are mainly lithium batteries, at present, lithium batteries are still lacking in safety, which makes EV spontaneous combustion probability and it is more difficult to put out the fire after a fire than traditional fuel vehicles. Therefore, in the Chinese market, the insurance cost of electric vehicles has been greatly increased compared with that of fuel vehicles of the same class of the car. Since the market share of FCV is very limited so far, it is difficult to predict whether FCV will have accident rate and safety problems with its large-scale popularization in the future. Therefore, in the calculation, FCV calculated the same as the insurance costs of the fuel vehicle and the same insurance costs as EV in the Chinese market.

Considering the price of the Toyota Mirai and the level of luxury created by the interior, it is inappropriate to use more common low-class vehicles such as Toyota Corolla, Nissan Leaf, etc. Therefore, vehicles of similar levels and similar prices were selected for comparison. The gasoline vehicle chose Volvo S60 B5 [42], the EV chose the Tesla Model 3 long-range version [43], and the FCV chose the Toyota Mirai [44] for comparison. The insurance fee is converted according to the exchange rate, about 110,000 yen for fuel vehicles, and about 180,000 yen for electric vehicles.

As shown in Figure 1.2, we first compared the usage costs of various types of vehicles when they travel 10,000 kilometers a year with changes in fuel prices. Here, due to the different maintenance requirements of different manufacturers, the actual maintenance costs are not taken into account; the

vehicle prices are similar, so the price difference can also be ignored. Only insurance and fuel are included in the cost. It can be seen from the figure that with the changes in fuel prices, new energy vehicles do not always maintain a cost advantage. When the price of gasoline is about 180 yen, the hydrogen price needs to remain at about 800 yen to have a cost advantage. Under this calculation condition, it is difficult to significantly reduce the cost of using new energy vehicles until the safety problem is effectively solved. However, as can be seen from the figure, regardless of whether FCV or EV, the cost of insurance accounts for a considerable proportion, which means that when the mileage increases, the average cost is expected to be lower than that of gasoline vehicles.

As shown in Figure 1.3, we used the current average fuel price as a reference, fixed the fuel price and insurance costs (gasoline price is 180 yen, electricity price is 30 yen, hydrogen price is 1000 yen), and calculated for one year Changes in cost corresponding to different forms of mileage. As can be seen from the figure, EVs have a huge advantage at current average fuel prices. However, considering the charging time and other issues, especially in Japan, due to the low voltage, fast charging on the market can only provide charging services at 200 V, and the actual charging experience is not ideal, which is negative for product promotion. In the case of the high insurance costs of FCV, when the mileage exceeds 13,000 kilometers in one year, FCV begins to have a cost advantage, and the advantage becomes larger as the mileage increases. When it reaches the annual mileage of 150,000 kilometers, the cost is about half of the fuel vehicle. This means that in the case of long-term use, such as taxis, FCV will have a greater cost advantage, and for general consumers, this will also be a large advantage for consumers to choose FCV. Longer mileage requires a more durable power unit, it is necessary to improve the durability of the fuel cell system.

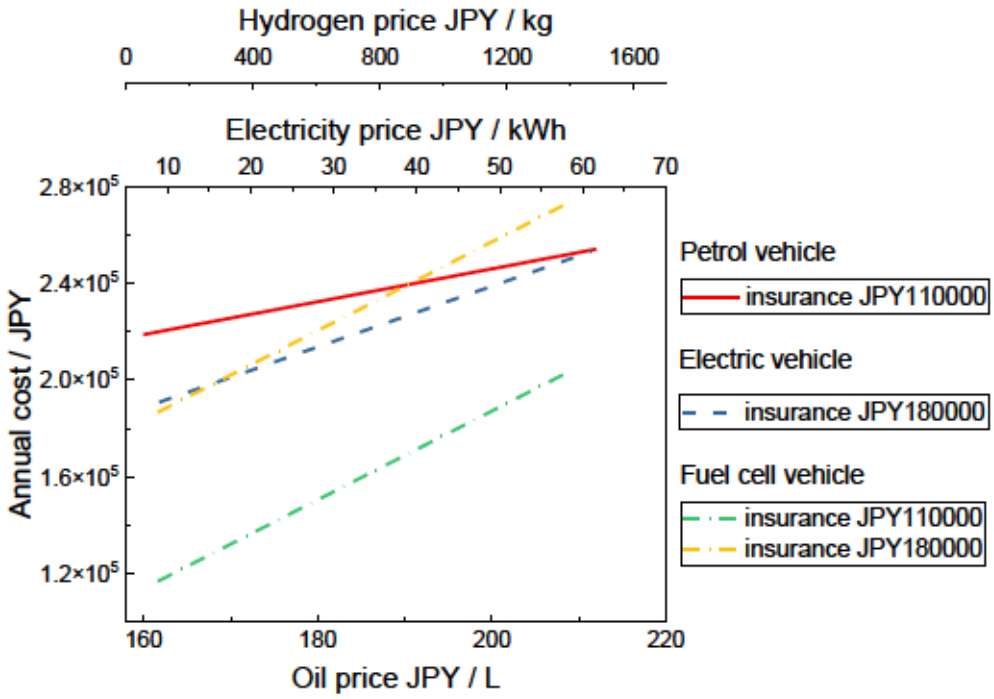

Fig. 1.2 the total cost of gasoline and electric vehicles, under different fuel consumption/power consumption and related insurance costs, the annual cost of 10,000 kilometers of traditional gasoline and electric vehicles.

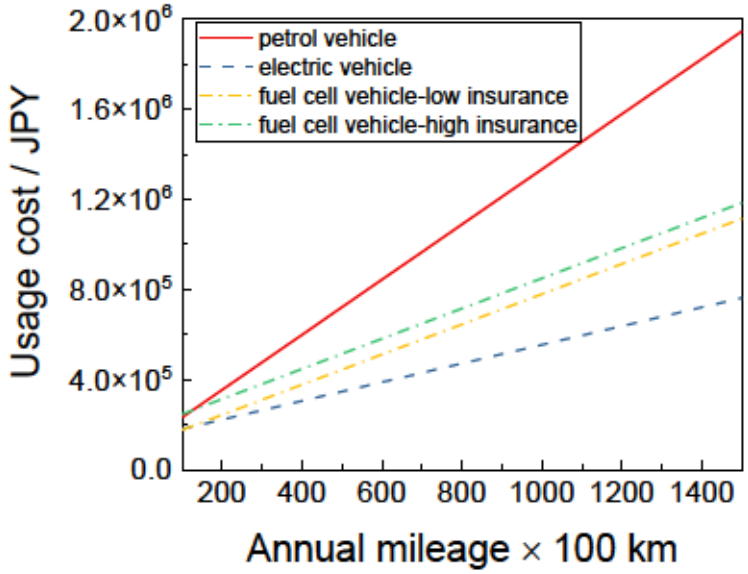

Fig. 1.3 the total cost of gasoline and electric vehicles, under different Annual mileage

1.6 The motivation of this research

Commercial PEFC devices are mainly catalyzed by platinum-supported carbon (Pt/C) on the cathode side. Carbon materials are widely used as support in PEFC due to their high conductivity and surface area. Unfortunately, carbon is unstable in an acidic environment that the standard electrode potential is 0.207 V vs. reversible hydrogen electrode (RHE) [45, 46], which means that the support would be oxidized during the operation of PEFC devices and cause the performance to drop such as in some cases, after 400 hours durability test, the Pt particles which deposited on the surface of the carbon support, would have a severe agglutination. [46] The issue of carbon support led to a short lifespan of PEFC devices and limited business promotion. As a power generation device in a car or small-scale power generation station/equipment, the lifetime is essential; it should not have a significantly shorter overhaul time/lifetime than internal combustion engines, seriously affecting the actual commercial application. In addition, depending on the roadmap via New Energy and Industrial Technology Development Organization (NEDO), which was published in 2017, it required that in 2040, the maximum load point voltage would be significantly improved from 0.6 V to 0.85 V. [47] This means that the operating environment of the PEFC system will be more severe than the existing situation, and traditional carbon materials will be oxidized faster under such harsh conditions, making it challenging to meet the target requirements. New catalyst support materials with high durability need to be developed.

As the solutions to this problem, first, there have been reported that graphite could improve the stability of carbon material. [48] Wang et al. reported that multi-walled carbon nanotube (MWNT) had higher durability than carbon black Vulcan XC-72, which had a 30% lower corrosion current after a 168 h 0.9 V constant voltage accelerated deterioration experiment in 0.5 M H_2SO_4 at 60 ºC with N_2 purged. [49] Second, Pt alloy also improved durability. Some Pt alloys, such as Pt_3Ni/C [50], and Pt-Co/C [51] have been reported to a good stability. Moreover, improving the interaction of Pt-C was also could improve the stability. Burguete et al. reported that the less acidic oxygen groups could improve the interaction between deposited metal and carbon support, which could limit the sintering of Pt nanoparticles. [52] Although many methods to delay the performance decay have been reported, they

have not fundamentally solved the corrosion problem of carbon materials.

As another one of the solution for the problem, carbon-free platinum/metal oxide support catalysts have been widely researched and reported. The conductive metal oxide supports have been researched and reported as an electrode material because of their stability, such as titanium oxides, tungsten oxides, tin oxides, cerium oxides, zinc oxides, nickel oxides, and molybdenum oxides. [53-61] Herein, the test/operation environment of PEFC is an acidic environment, some materials that dissolve easily in acidic conditions are not suitable. As durable materials in acidic media, titanium oxides, tungsten oxides, cerium oxides, and molybdenum oxides have the potential to be cathodic support in PEFCs. [53-58, 61] Compared with other oxide materials, titanium oxide and tin oxide-based materials have been mainly investigated due to their high durability. [55-57, 62-66] Herein, T. Arai et al reported that although both tin oxide and titanium showed high stability in acid, tin oxide is not stable in reducing conditions above 80 °C, and titanium oxide is not stable in oxidizing conditions above 80 °C, which means that the tin oxide should be used as anodic support and the titanium oxide should be used as cathodic support. [67] The reported platinum/titanium oxide support catalysts such as Pt/TiO_2, Pt/Ti_4O_7, and Pt/Nb-TiO_2 show high durability, and the contents are mainly the comparison of catalyst durability and the investigation of the cause. In some instances, Ioroi et al. reported that the loss of voltage in Pt-Ti/Ti_4O_7 membrane electrode after 10000 cycles durability cycles swap between 1.0 and 1.5 V vs. RHE was tiny, and the membrane electrode still showed a good performance after the durability test. [63] Moreover, Morales et al. reported that there was a 30% drop in mass activity of 7Pt/1Ta/SnO_2 catalyst after 6000 cycles ADT from 1.0 to 1.6 V vs. RHE in a half cell with 0.1 M $HClO_4$, which had a more minor of mass activity loss that commercial Pt/C catalyst. [66]

However, it is necessary to combine the optimum platinum and titanium oxide support according to the usage conditions for practical use. Therefore, not only the study of the platinum supporting method but also the properties of the support are essential information. On the other hand, although platinum/titanium oxide support catalysts have high durability, they are not completely degraded. Therefore, to deeply understand and further study the high durability of platinum/titanium oxide support catalysts, platinum on oxides The characteristics are also important information. Unfortunately, as an introductory study of platinum/titanium oxide support catalysts, there are few reports of

systematically obtaining precursor synthesis conditions and conductivity of titanium oxide supports, changes in properties due to reduced heat treatment conditions, and platinum on titanium oxide supports by durability tests. In addition, the performance such as specific surface area and conductivity was still low, the reported case of mesoporous Magnéli phase titanium oxide had a relatively high specific surface area (11 m^2 g^{-1}), and the mesoporous structure could form the electron conduction pass, however, the specific was still low. [68] Moreover, although several cases reported that Pt/titanium oxide-based support catalysts showed good durability and activity, the behavior of Pt, deposited on the surface of titanium oxide has not been cleared yet.

To elucidate the characteristics of changes in the physical properties of titanium oxide by reduction heat treatment and the deterioration principle of platinum on the oxide, in this study, Nb-doped titanium oxide supports were synthesized by hydrothermal method. We evaluated changes in surface area, investigated control factors for conductivity and specific surface area, studied the behavioral characteristics of platinum on a macroporous Nb-doped titanium oxide support with high conductivity, and investigated the cause of high durability.

Chapter 2

Synthesis of Nb-doped titanium oxides with controlled surface area and conductivity as cathodic supports in polymer electrolyte fuel cells

2.1 Introduction

In general, there is a large bandgap in TiO_2 ((approximately 3.2 eV and 3.0 eV for the TiO_2 anatase phase and TiO_2 rutile phase, respectively), which leads the TiO_2 to have a characteristic of a semiconductor. Traditionally, two ways are used to improve the conductivity in Ti-oxides based materials. The first one is the formation of Magnéli phases of titanium oxides (Ti_nO_{2n-1}; $4 \leqq n \leqq 10$) [69. 70], particularly Ti_4O_7, which has high durability in acidic media and a high conductivity which reaches the carbon materials. Up to now, it is unable to synthesize the Magnéli–phase Ti_4O_7 directly by wet chemical method, the reduction heat treatment of TiO_2 precursor such as with hydrogen atmosphere reduction [71], metallothermic reduction [72], or carbon-thermal reduction [73] is necessary. However, the specific surface area would inevitably be decreased because of the agglutination or sintering under the high treatment temperature, which usually reached approximately 1000 ℃.

The other way is dopant of foreigner elements. In general, foreigner element doping introduces defects that increase the carrier concentration and thus improve conductivity. For the dopant of TiO_2, there are lots of cases, such as the transition elements like copper, cobalt, chromium, manganese, nickel, molybdenum, vanadium, niobium, iron, platinum, gold, silver; and non-metal elements such as boron nitrogen, phosphorus, iodine, carbon, sulfur, fluorine-doped TiO_2 have been investigated and reported. [74-77] In those reports, foreign element doping could decrease the bandgap, which means that dopant could increase the conductivity of titanium-based oxides. However, from the practical point of view, it is difficult to prepare single-crystal nanoparticle carriers. In the case of polycrystalline, the band gap that can be reduced by Nb doping is limited. [78] As a support material, electrical conductivity is one of the most important properties, so in actual preparation, reduction heat treatment is still necessary.

Meanwhile, considering the operating environment of PEFC, the dopant elements should be the same as the metal oxide that has good stability in an acidic environment. Herein, as a relatively well-researched conductive metal oxide, niobium-doped TiO_2 has been researched for many years as conductive transition group element metal oxide thin film [79-82]. Niobium dopant could improve both conductivity and the resistance of phase transform from anatase TiO_2 to rutile TiO_2, which could

reduce grain growth at high temperatures, thereby reducing the loss of specific surface area caused by heat treatment. Due to the above-mentioned advantages, Nb-doped TiO_2 has been researched as cathodic support for ORR. [83-88] Elezović et al. reported that the Pt/Nb-TiO_2 catalyst had better mass activity (MA) and specific activity (SA) than the Pt/C catalyst (70 mA mg^{-1} Pt, 0.165 mA cm^{-2} Pt, and 73.8 mA mg^{-1} Pt, respectively), as a comparison, the electrochemical surface area (ECSA) of Pt/C was larger than Pt/Nb-TiO_2 catalyst (96 m^2 $g^{-1}{}_{Pt}$ and 42.5 m^2 $g^{-1}{}_{Pt}$, respectively). [83] Meantime, similar phenomena have also been reported by He et al. The aerogel method synthesized Pt/Nb-TiO_2 had larger MA and SA than Pt/C catalyst, which was 150 mA $mg^{-1}{}_{Pt}$, 349 μA $cm^{-2}{}_{Pt}$, and 124 mA $mg^{-1}{}_{Pt}$, 149 μA $cm^{-2}{}_{Pt}$, respectively. Also, the Pt/Nb-TiO_2 showed good durability after 10000 cycles of accelerated durability test (ADT), which just had a 22% loss of ECSA. Many works have reported the excellent performance of niobium-doped titanium oxide as ORR catalyst support, exceptionally high durability, and good application prospects, but there was little systematic research on changes in the preparation and physical properties of conductive niobium-doped titanium oxide. [84] In addition, Senoo et al. reported that when a large amount of Pt (over 15 wt%) was deposited onto the surface of oxide support, the conductivity would have an increase of 2 – 4 orders of magnitude. [85]

This research focused on synthesizing Nb-doped titanium-oxide as the cathodic support for ORR reaction by the hydrothermal method in the PEFCs. Herein, based on different research purposes, we synthesized Nb-doped TiO_2 and Nb-doped Ti_4O_7 supports. First, we used chemically similar metal-organic compounds to prepare highly doped niobium-doped titanium oxides up to 30 at%. Then, because the priority of specific surface area and conductivity is not the same with different Pt loading, and it is difficult for Nb-doped TiO_2 to have both high specific surface area and conductivity until now, the parameters such as the dopant niobium amount, heat-treatment temperature, and heat-treatment time were attempted to conduct, and its specific surface area, electrical conductivity, crystal structure, and electronic state were evaluated, cleared the effect of surface area, and conductivity of Nb dopant in Nb-doped titanium oxide support. Meanwhile, the silica colloid template was combined with the hydrothermal method, with the doping of an appropriate amount of niobium, high-temperature reduction heat treatment in a pure hydrogen atmosphere, and subsequent removal of the template, the macroporous Nb-doped Ti_4O_7 with both high specific surface area and high conductivity was prepared. We analyzed the role of niobium and discuss the reasons for its high conductivity. Finally, using Nb-

doped Ti_4O_7 as a support, we prepared Pt/ Nb-doped Ti_4O_7 model catalysts to study the behavior of Pt on oxide surfaces during the durability test. The degradation characteristics analysis will be introduced in Chapter 3.

2.2 Experimental

2.2.1 Preparation of nanoparticle Nb-doped TiO_2 support

The preparation of niobium-doped titanium oxide with the hydrothermal method is based on Lü et al. reported synthesis method. [86] Titanium (IV) butoxide ($C_{16}H_{36}O_4Ti$, 97%, Sigma-Aldrich) and niobium (V) ethoxide ($C_{10}H_{25}NbO_5$, 99.95%, Sigma-Aldrich) were used as the sources of titanium and niobium, respectively. 18 mmol of titanium (IV) butoxide, and the given quantity of niobium (V) ethoxide, that from 0 at% to 30 at%, were stirred and mixed at room temperature. Then, 30mL deionized water (DI water) was dripped slowly into the mixture. Third, transferred this solution into a 100 mL Teflon-lined stainless autoclave for the hydrothermal reaction at 180 °C for 20 h, with a heating rate as 3 °C min^{-1}. When natural cooling to the room temperature, the precipitation was rinsed several times with DI water and ethanol to remove the alcohol and vacuum dried at 80 °C for 12 h. In order to altogether remove organics which was unremoved by washing and may remain on the surface of the precipitation, 0.2 g of niobium doped titanium oxide was heated in air at 380 °C for three hours to obliterate the trace organics. Finally, the precursor was done the heat treatment under a given temperature and a given time under 200 cm^3 min^{-1} pure hydrogen flow to synthesize the Nb-doped TiO_2 support.

2.2.2 Preparation of macroporous Nb-doped Ti_4O_7 support

Macroporous Nb-doped TiO_2 precursor was synthesized based on the reported synthesis method [87], and the colloidal crystal template was synthesized based on the previous synthesis method. [88] First, tetraethyl orthosilicate (TEOS, ≥99.0%, Sigma–Aldrich), Tris(hydroxymethyl)aminomethane, (THAM, ACS reagent, ≥99.8%, Sigma–Aldrich), and DI water with a molar ratio of 45 : 1 : 2780, were mixed and aged at 80 °C for 24 h. Second, a partial solution was transferred to another THAM solution and doped TEOS as an above molar ratio. 60 nm silica nanospheres were prepared, and the size of synthesized silica seed nanospheres could be calculated by the equation:

$$\left(\frac{\text{Diameter}_{\text{final}}}{\text{Diameter}_{\text{seed}}}\right)^3 - 1 = \frac{\text{Mass}_{\text{TEOS,doped}}}{\text{Mass}_{\text{TEOS,seed}}} \tag{2.1}$$

Third, to obtain the colloidal crystal template, the solution was evaporated at 50 °C and calcinated in the air at 550 °C for 6 h. Then, 2 mL $TiCl_4$ (16–17% as Ti, Wako), 7 mL DI water, and 20 μL conc. HCl (35.0–37.0%, Wako) was mixed with an ice bath. 5.0 g prepared template doped into 33 mL, 15 mM $TiCl_4$ diluted solution, which was prepared by diluting the previously prepared mixture with DI water and aged to 70 °C for 1 h. Finally, the Ti–containing template was collected by suction filtration, rinsed several times with DI water, and heated in air at 550 °C for half an hour.

0.72 g of the Ti–containing template was doped into a solution that contained 0.8 mL Titanium(IV) butoxide, 120 μL $NbCl_5$ (99%, Sigma–Aldrich). 28 mL DI water, and 28 mL conc. HCl. Then, transferred the mixture into a 100 mL Teflon-lined stainless autoclave for a hydrothermal reaction at 150 °C for 12 h. When natural cooling to the room temperature, the precipitation was washed several times with DI water and ethanol and dried under vacuum at 80 °C for 12 h to obtain the Nb-doped TiO_2 with the template. Third, Nb-doped TiO_2 with the template did the heat treatment under 200 cm^3 min^{-1} pure hydrogen flow to synthesize the Nb-doped Ti_4O_7 with the template. Finally, in order to remove the hard template, the product was heated in a 2 M NaOH aqueous solution at 80 °C for 2h.

2.2.3 Evaluation of the number of oxygen vacancies with thermal gravimetric

After hydrogen reduction heat treatment, the samples were calcined at high temperatures in the air to obtain titanium dioxide without oxygen vacancies. The number of oxygen vacancies could be calculated by calculating the weight difference of the samples before and after calcination. Since the sample will inevitably adsorb water in the air, we plotted the relative relation between the specific surface area and the change of mass caused by evaporation adsorbed water on the surface of titanium oxide and compensated for the mass error before and after calcination caused by the adsorbed water. Due to it being different from buying or preparing the Nb-doped TiO_2 with different Brunauer–Emmett–Teller (BET) surface areas, and dopant did not generate $Nb_xTi_yO_z$ compounds (described later), we used commercial TiO_2 powders with various crystalline phases and BET surface areas. The information is shown in Table 2.1. The plot of specific surface area versus mass change at 1000 °C is

shown in Fig 2.1.

The amount of Ti was calculated by the equation:

$$m_{Ti} = m \times \frac{n_{Ti}}{n_{TiO2}} \tag{2.2}$$

Here, m_{Ti} is the mass of Ti in the sample, m is the weight after calcined, n_{Ti} is the standard atomic weight of Ti, and $nTiO_2$ is the standard atomic weight of TiO_2.

The amount of Ti was calculated by the equation:

$$m_O = m^* - m_{Ti} \tag{2.3}$$

Here, m_O is the mass of O in the sample, and m^* is the compensated weight before calcined.

Finally, the molar ratio of Ti and O could be calculated, and the calculated chemical composition and amount of oxygen vacancy could be estimated.

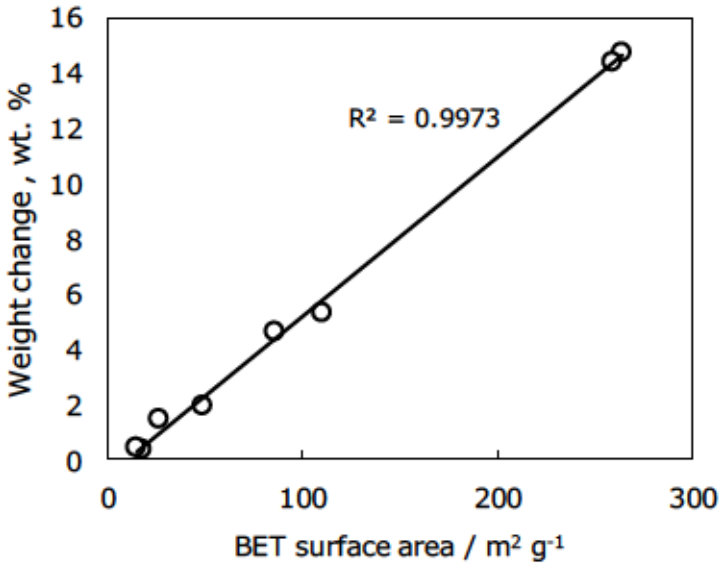

Fig. 2.1 Relationship between the BET surface area and the change of weight which was caused by the desorption of the adsorbed water.

Table 2.1. List of TiO_2 particles with various crystalline structures, BET specific surface areas, and weight loss

Crystalline structure of sample	BET surface area (m^2/g)	Weight loss (wt. %)
Anatase	264	14.70
Anatase	86	4.62
Anatase	49	1.89
Anatase	18	0.31
Rutile	27	1.43
Rutile	14	0.40
Amorphous	259	14.39
Rutile	110	5.27

2.2.4 Physico-chemical characterization of supports

The crystalline phases of the supports were recorded by power X-ray diffraction (XRD; Rigaku Ultima IV) with Cu Kα radioactive source (λ = 0.15406 nm). The measurement of BET specific surface area was N_2 adsorption (BELSORP-mini, Microtrac BEL). The number of oxygen vacancies was calculated by thermal gravimetric (TG; Thermo plus EVO, Rigaku) analysis as the above method. The electrical resistance of the support was measured with a DC resistivity analyzer (RM3545, Hioki); the support was placed in a cylinder holder and gave a vertical pressure that reached 60 MPa. Figure 2.2 is a schematic diagram of the resistance test. The electrical conductivity (σ) is calculated according to the following equation:

$$\sigma = \frac{t}{AR} \tag{2.4}$$

Here, t is the sample thickness with a given pressure, A is the bottom area of the DC resistivity analyzer stainless steel electrode (0.196 cm^2), and R is the value of resistance read from the analyzer. The surface electronic state of the prepared metal oxide supports was investigated by X-ray photoelectron spectroscopy (XPS; PHI Quantum-2000). Herein, the C1s peak spectrum attributed to free carbon at 284.8 eV was used for compensation of surface charge. Observation of surface morphology characteristics via scanning electron microscopy (SEM, SU8000, Hitachi High-Technologies) and transmission electron microscopy (TEM, LEM-2100F, JEOL).

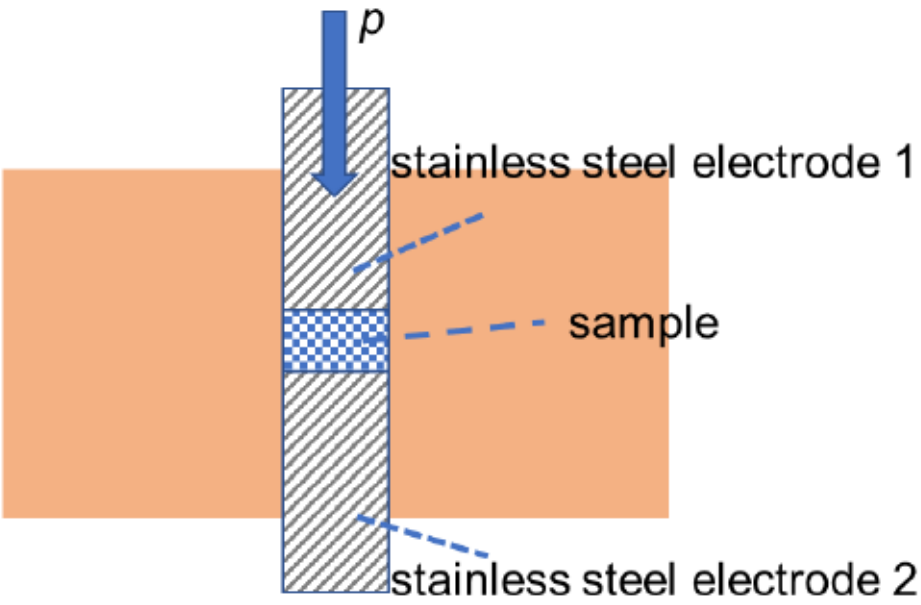

Fig. 2.2 Sectional schematic diagram of powder conductivity test.

2.2.5 Electrochemical measurements

2 mg prepared support was dispersed into a mixture of 300 μL hexanol (Wako, Ltd.) and 5 μL of 0.5-wt% Nafion® aqueous solution (Sigma-Aldrich), ultrasonic under an ice bath for 40 min to prepare the support ink. Then, cast 10 μL ink onto the polished top surface of the glassy carbon (GC; φ = 5.2 mm, Tokai Carbon Co., Ltd.) rod, and dried the rod at 60 °C for 1 h in air. As a control comparison, ink of 1 mg of carbon support (KB; Ketjenblack EC-300J) was also prepared, and the amount of hexanol and Nafion® solution were 350 and 5 μL, respectively.

Electrochemical tests were covered in a 3-electrode cell, in 300 mL 0.1 M $HClO_4$ electrolyte via a potentiostat (PS08, TOHO Technical Research). An accelerated durability test (ADT) with the swap rate of 0.5 V s^{-1} from 1.0 to 1.5 V vs. the RHE at 60 °C by the start/stop accelerated durability cycle test was recommended via the Fuel Cell Commercialization Conference of Japan (FCCJ) [89].

Cyclic voltammetry (CV) was recorded under saturated N_2 at 60 °C with a swap rate of 50 mV·s^{-1} from 0.05 to 1.5 V vs. the RHE. The charge of the electrical double layer was calculated from the anodic side current at 0.8 - 1.0 V vs. RHE.

2.3 Results and discussion

In order to discuss the effect of niobium doping on titanium oxide, first, we compared the changes in the surface morphology of nanoparticle supports with different doping amounts after reduction heat treatment at 600 °C, 5 h, under a pure hydrogen atmosphere. As shown in Fig. 2.3, It can be found that with the increase in doping amount, the sintering of the samples after reduction heat treatment was significantly suppressed. The undoped sample (Fig. 2.3 (a)) was sintered into larger spherical particles after reduction heat treatment, while the 30 at% doped sample (Fig. 2.3 (e)) still maintained the morphology of fine particles. Figure 2.3 (f) compared the value of the specific surface area after heat treatment. With the increase of the doping amount, the sintering resistance was effectively improved, so that a relatively higher specific surface area can be obtained after the reduction heat treatment. The BET specific surface areas of the samples were 12, 26, 30, 66, and 66 $m^2 g^{-1}$, respectively. As a comparison, the BET specific surface areas of the Nb-doped TiO_2 precursors with 0, 5, 10, 20, and 30 at% of R_{Nb} were 132, 157, 150, 123, and 101 $m^2 g^{-1}$, respectively. In general, the doped impure element would have a solid solution strengthening effect. [74] The dislocation propagation will be hindered, impending plasticity, and increasing yield strength proportionally with solute concentration, which thus makes the material stronger. [69, 97] As conductive oxide support, the surface area was also important. It could be found that without dopant, the undoped TiO_2 particles showed sintering and growth obviously, while just a little sintering in 5at% and 10at% Nb-doped TiO_2. Moreover, almost no sintering and growth could be found in 20at% and 30at% Nb-doped TiO_2. The effect of solid solution strengthening by Nb dopant was observed clearly. Specifically, as shown in Fig. 2.4 (a), when undoped, the macroporous of the outermost layer almost disappears due to the excessively fast crystal growth rate. For comparison, as shown in Fig. 2.4 (b), when the doping amount is 2 at%, it is difficult to connect with each other to form a macroporous structure due to the slow growth rate of grains. Moreover, it can be speculated that if the doping amount is further increased, the morphological characteristics may tend to be nanoparticle-like, and the macroporous structure cannot be synthesized. When the doping amount was 1 at%, as shown in Fig. 2.4 (c), the Nb-doped TiO_2 with a uniform macroporous structure can be obtained by the hydrothermal synthesis method and after removing the template. Thus, 1 at% was the relatively optimal doping amount in this experiment. Since other doping amounts could not obtain uniform macroporous morphology, only 1 at% doped sample was subjected

to reduction heat treatment. The SEM of the sample after reduction heat treatment was shown in Figure 2.4 (d). After removing the template, the macroporous structure was still clear and intact. The specific surface area was as high as 46 $m^2 g^{-1}$ after the reduction heat treatment, indicating that the use of seed crystal and hydrothermal preparation, and the method of removing the template after the reduction heat treatment, can successfully prepare a macroporous structure with high specific surface area Nb-doped Titanium oxide support.

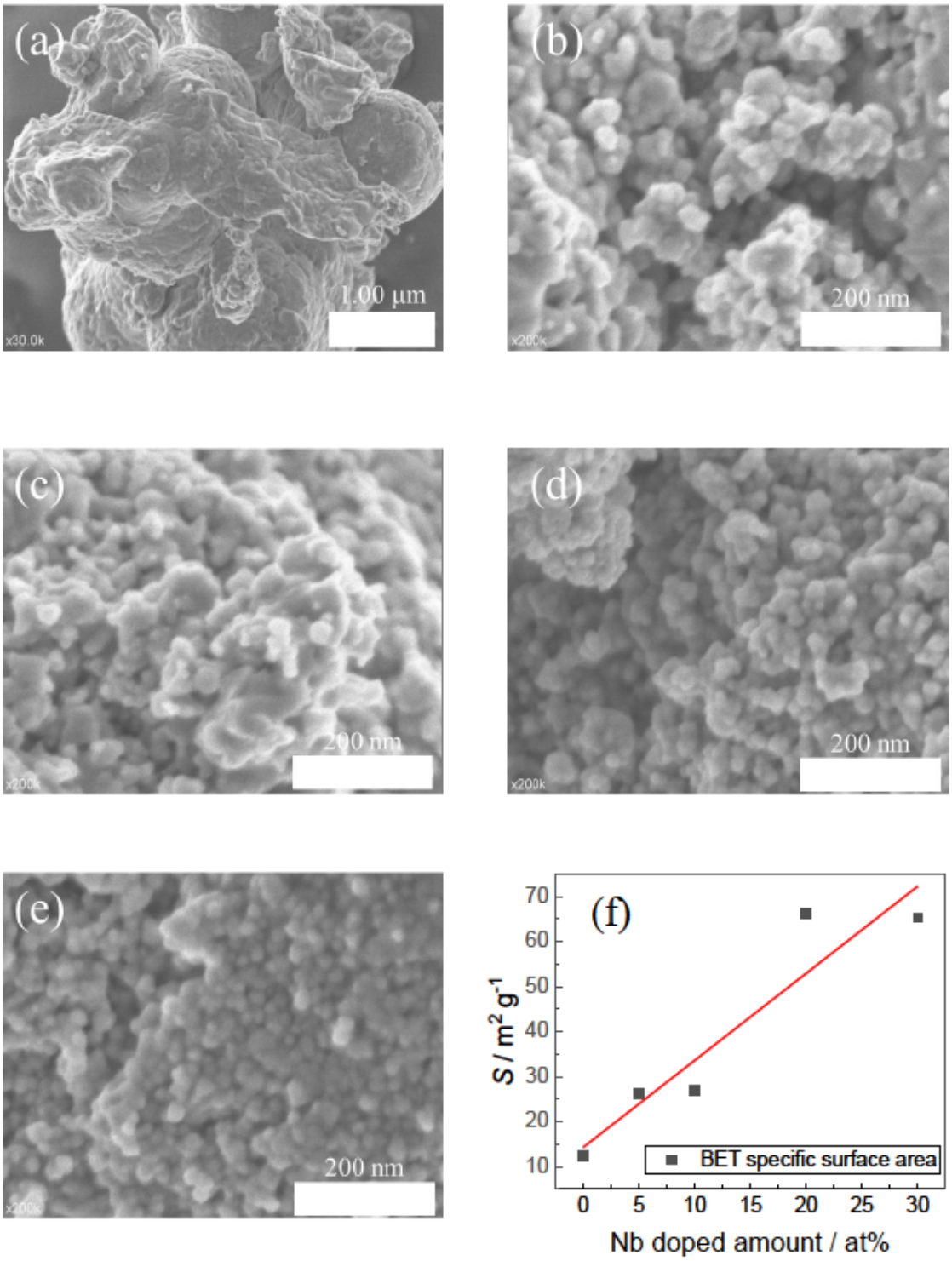

Fig. 2.3 FE-SEM images of nanoparticle Nb-doped TiO_2 after heating at 600 °C for 5 h under H_2 atmosphere, (a) 0 at% Nb doped, (b) 5 at% Nb doped, (c) 10 at% Nb doped, (d) 20 at% Nb doped, and (e) 30 at% Nb doped, (f) relationship between Niobium Doping Amount and Specific Surface Area after Reduction Heat Treatment

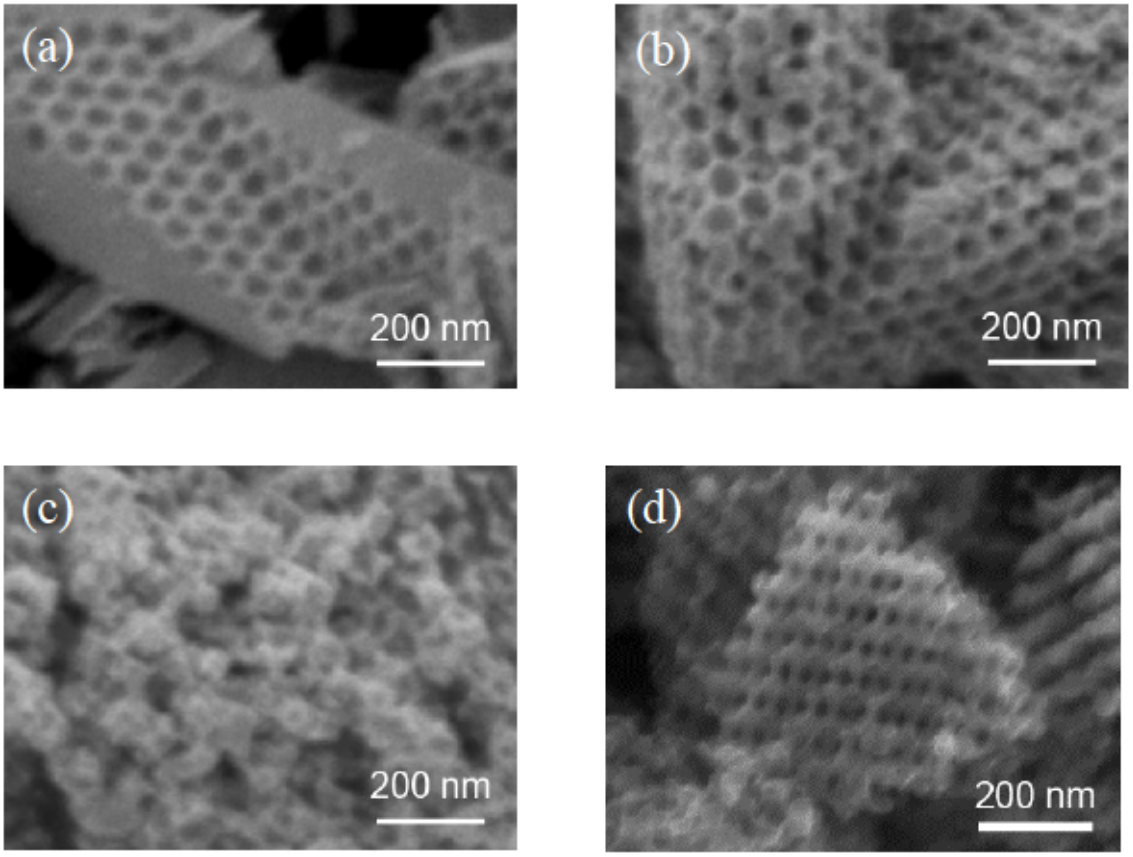

Fig. 2.4 FE-SEM images of macroporous Nb-doped TiO_2 and 1 at% Nb doped TiO_2 after heating at 900 °C for 5 h under H_2 atmosphere, (a) 0 at% Nb doped, (b) 1 at% Nb doped, (c) 2 at% Nb doped, (d) macroporous 1 at% Nb doped TiO_2 after heat treatment.

Figure 2.5 shows the XRD diffraction patterns of nanoparticle Nb-doped titanium oxide support and microporous Nb-doped titanium oxide support after heat treatment at 600 °C, 5 h, under pure hydrogen atmosphere and 900 °C, 5 h, under a pure hydrogen atmosphere, respectively. The crystal phase of nanoparticle supports were anatase TiO_2, rutile TiO_2, or the mixture, and the macroporous supports was mainly of Ti_4O_7, with some γ-Ti_3O_5 and anatase TiO_2. For the nanoparticle Nb-doped TiO_2 support, rutile ratio (R_r) was calculated as the followed equation:

$$R_r = 1 - (1 + \frac{\frac{I_{rutile}}{0.79}}{I_{anatase}})^{-1} \quad (2.5)$$

Where I_{rutile} and $I_{anatase}$ were the intensities of the TiO_2 rutile phase (1 1 0) and TiO_2 anatase phase (1 0 1) peaks in the XRD patterns, respectively.

From the XRD pattern that for nanopartocle Nb-doped TiO_2 support, the amount of niobium doping will affect the phase transfer after heat treatment. When the doping amount is higher than 20 at%, the niobium doping will inhibit the phase transfer, the reason for which will be discussed in detail later. For macroporous Nb-doped Ti_4O_7 support, γ-Ti_3O_5 may be caused by the excessive reduction of the oxide surface due to the long-term high-temperature reduction heat treatment. As opposite, because of the large size of Nb-doped Ti_4O_7 support, there might be insufficiently reduced parts at the inside the crystal, which was preserved as anatase TiO_2.

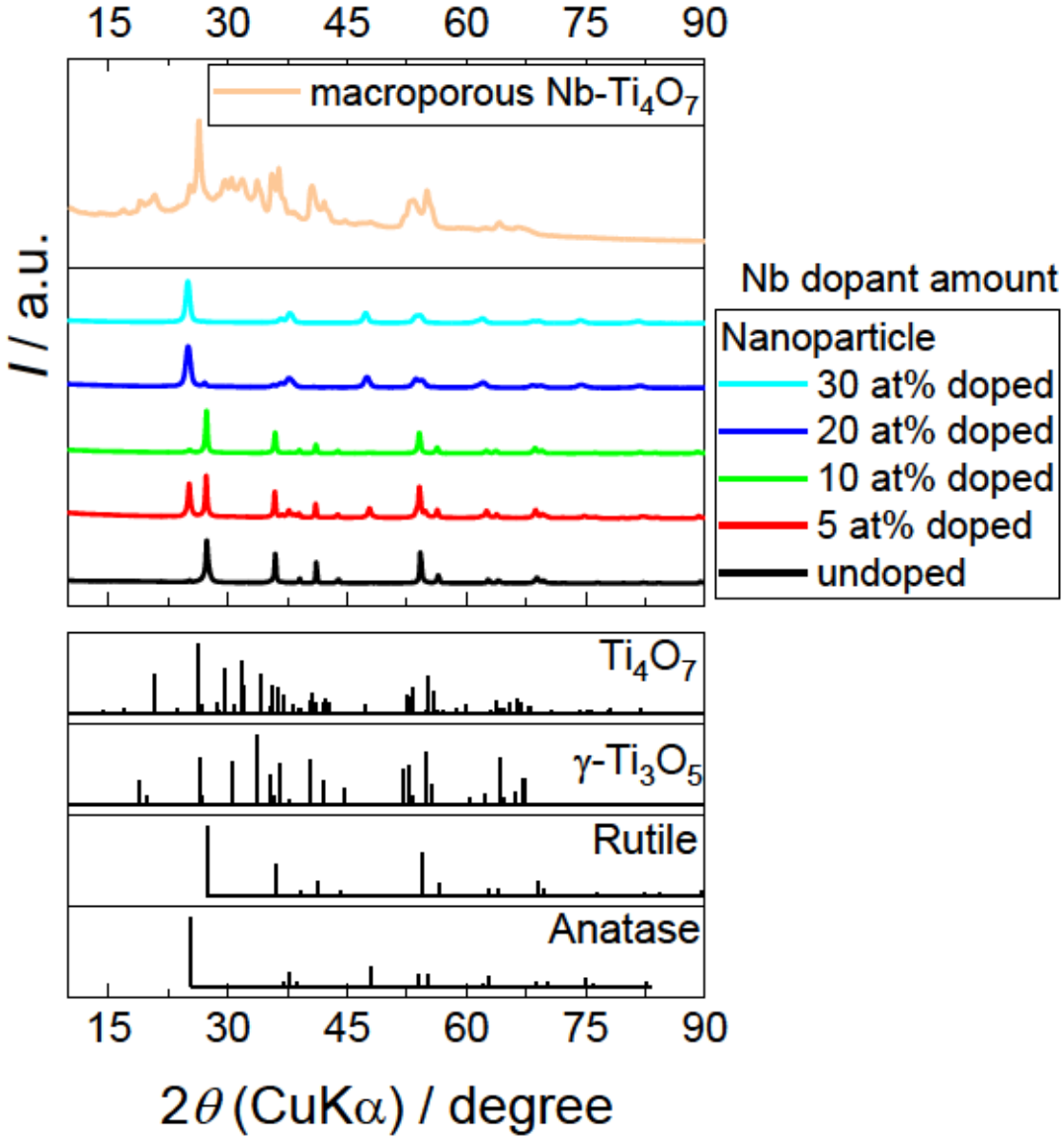

Fig. 2.5 XRD patterns of nanoparticle Nb-doped TiO_2 powders which was done the reduction heat treatment at 600 °C for 5 h under pure H_2 with various amounts of Nb dopant, and macroporous Nb-doped Ti_4O_7 which was done the reduction heat treatment at 900 °C for 5 h under pure H_2.

Herein, to confirm the above description, the amount of oxygen vacancies in the samples was quantified using TG-DTA. Figure 2.6 shows the relationship between the number of oxygen vacancies in the Nb-added TiO_2 heat-treated at 600 °C for 5 h under H_2 and the ratio of doped Nb. As predicted, the oxygen vacancies decreased with an increase in R_{Nb} from 0 to 5 at%. This was responsible for the Nb^{5+} incorporation into TiO_2 with electroneutrality. The oxygen vacancies increased almost linearly with an increase in R_{Nb} at above 5 at%. Therefore, the phase transformation was promoted as R_{Nb} increased above 5 at%. In fact, the phase transition completely proceeded for 10 at% Nb-added TiO_2. From the viewpoint of the amount of oxygen vacancies, the phase transformation accelerated at above 10 at%. However, as described above, the segregated niobium oxide inhibited the transition for 20 and 30 at%. The previous experimental results on the effect of Nb dopant on crystal phase transitions are summarized. [91-97] Dopant of Nb^{5+} -substituted for Ti^{4+} in the crystal cell, which reduced oxygen vacancies because of electroneutrality. [93, 97] in generational, oxygen vacancies would lead to a phase transfer via the increase of lattice relaxation. [80, 91, 92, 95] Arbiol et al. reported when the dopant amount was low (~ 4 at%), the decrease of oxygen vacancies would inhibit the phase transfer. [67] Moreover, the Nb^{5+} ionic radius is larger than Ti^{4+}, and the slight stress in the titanium oxide lattice would also inhibit the phase transformation. [80, 91, 92, 96, 97] Further, when lots of Nb-doped in TiO_2, the NbO_x would be segregated at the surface of TiO_2 nanoparticles and form the strong Nb-O-Ti bands, which would also restrain the phase transformation. [80, 92, 93] Regarding the inhomogeneity of the macroporous Nb-doped Ti_4O_7 crystal phase, it could be considered that due to the high temperature and reduced atmosphere, Parts of the surface were over-reduced, and phase transfer to γ-Ti_3O_5, on the other hand, due to the large size of the oxide, the average size of the narrowest part between two adjacent pores was about 14 nm, resulting in an insufficiently reduced part inside, which was still retained in the crystalline phase of anatase TiO_2.

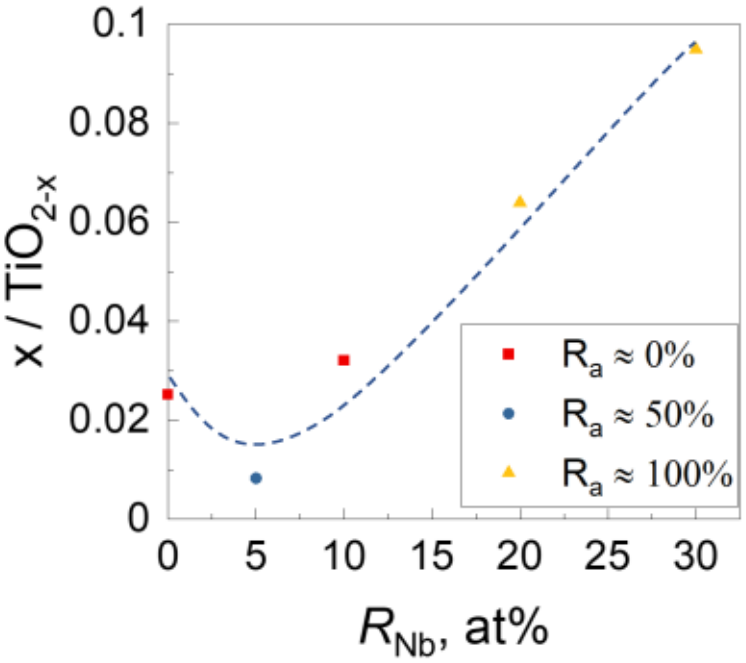

Fig. 2.6 Relationship between oxygen vacancies in Nb-doped TiO_2 after the reduction heat treatment at 600 °C for 5 h under H_2 atmosphere, and the Nb ratio, R_{Nb}.

In order to discuss the influence of heat treatment time and temperature on the specific surface area and electrical conductivity of the support, we compared the difference of the support under various conditions. As shown in Fig. 2.7, the effect of different heat treatment time and different doping amounts on the specific surface area for nanoparticle supports at 600 °C. The horizontal axis of the graph is the heat treatment time, and the vertical axis is the ratio of the remaining specific surface area after heat treatment compared with the untreated sample. It can be seen from the figure that after heat treatment, the specific surface area of all samples decreased to varying degrees. Among the undoped samples, only about 10% of the specific surface area was retained after 5 hours of heat treatment. As the SEM image in Figure 2.3 (a), the particles were severely sintered. With the increase in the doping amount, the anti-sintering ability had also been significantly improved. When the doping amount was 30 at%, about 53% of the initial specific surface area remains after 15 h heat treatment. It showed that with the increase in doping amount, the anti-sintering ability of support would be significantly improved.

Figure 2.8. compared the conductivity of all Nb-doped titanium oxide supports after the heat treatments, including nanoparticle and macroporous structural supports. In the figure, the horizontal axis is the heat treatment time, and the vertical axis is the electrical conductivity. The sample doping amount and heat treatment temperature are distinguished by different marking shapes and colors. As Fig. 2.8 shows that, macroporous Nb-doped Ti_4O_7 has the highest conductivity, reaching 0.1 S cm^{-1}. For nanoparticle Nb-doped TiO_2 support, the change of conductivity was discontinuous. The conductivity did not change significantly under the same heat treatment temperature with the same doping amount, but with the change of heat treatment temperature, the conductivity changes significantly. For Nb-doped TiO_2 supports with the same doping amount, the effect of reducing heat treatment temperature on electrical conductivity is greater than that of heat treatment time on electrical conductivity.

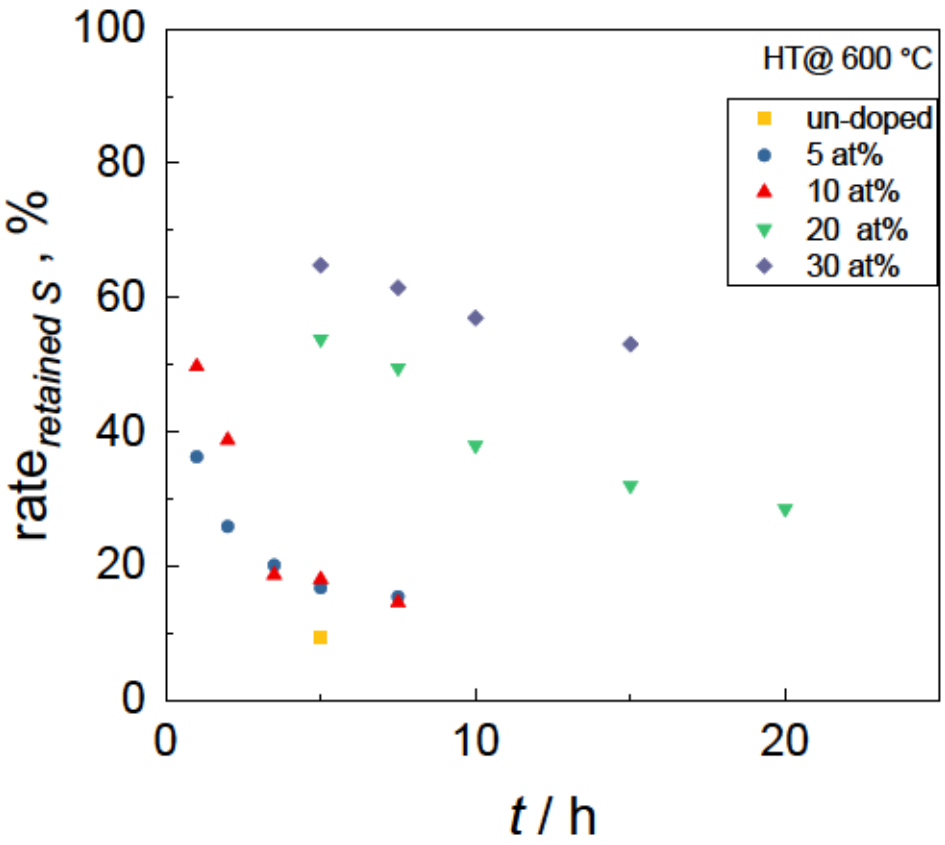

Fig. 2.7 Relationship between specific surface area retention rate and heat treatment time after heat treatment of nanoparticle Nb-doped TiO_2 after heating at 600 °C for 5 h under H_2 atmosphere.

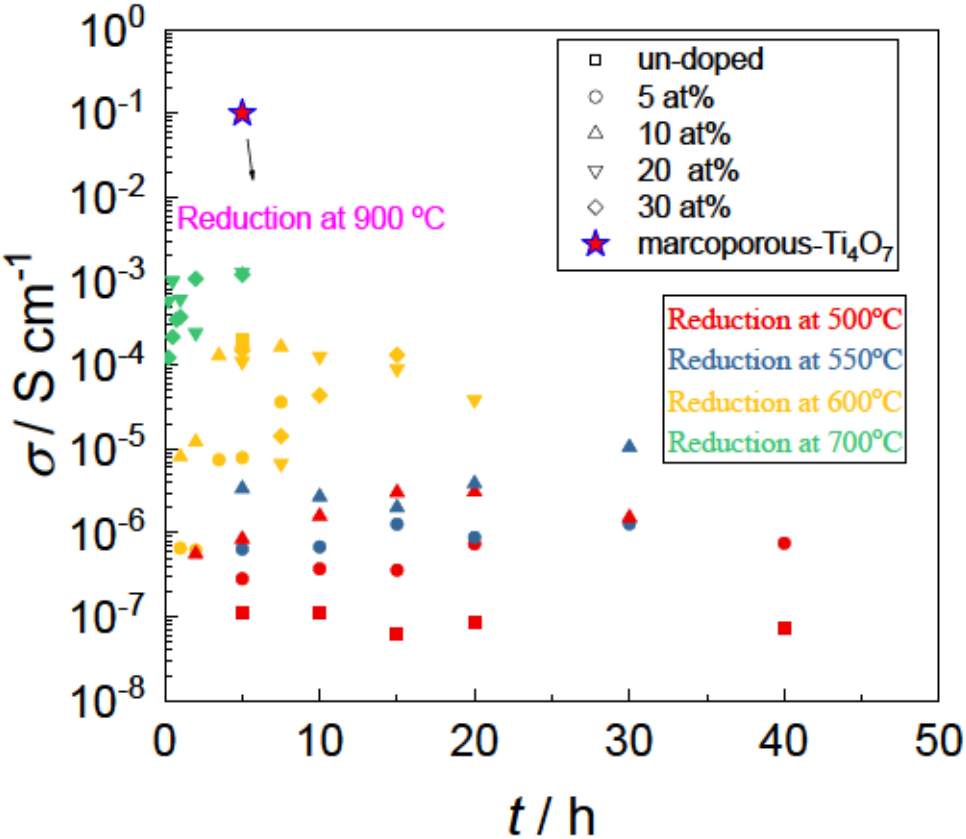

Fig. 2.8 Relationship between conductivity and heat treatment time after heat treatment of nanoparticle Nb-doped TiO_2 after heating at 600 °C for 5 h under H_2 atmosphere and macroporous Nb-doped Ti_4O_7 which was done the reduction heat treatment at 900 °C for 5 h under pure H_2.

To further explore the reasons for the high conductivity of Nb-doped Ti_4O_7, we analyzed the samples using TEM. Figure 2.9 (a) was the TEM image of nanoparticle 10at% Nb-doped TiO_2 support which was treated at 600 °C for 5 hours under a pure hydrogen atmosphere and Figure 2.9 (b) was the macroporous Nb-doped Ti_4O_7 support which treated at 900 °C for 5 hours under a pure hydrogen atmosphere. The integrity of the macroporous Nb-doped Ti_4O_7 support structure after heat treatment was further confirmed by TEM. In the electron diffraction patterns, It can be found that the crystal structures of the two were significantly different. The diffraction pattern of nanoparticle 10at% Nb-doped TiO_2 support showed a circular ring, which means it was polycrystalline. The ED pattern result is shown in table 2.2. In contrast, the diffraction pattern of macroporous Nb-doped Ti_4O_7 support was a few dots and did not form a ring. On the other hand, unlike the traditional single crystal diffraction pattern, the number of points here was large, indicating that it was not a large and uniform single crystal structure. Therefore, it can be inferred that the crystalline structure of macroporous Nb-doped Ti_4O_7 support was a large single crystal with several different crystal planes. Such a structure can effectively reduce the interface between crystals, thereby reducing contact resistance. Further, from the perspective of macroporous structure, the interconnection between oxide particles greatly reduced the contact surface, thereby reducing the contact resistance and forming an effective conductive path.

Figure 2.10 shows the BET specific surface area and conductivity of both two methods of prepared support. It could be found that the support prepared by the hydrothermal method exhibited a gradient distribution which is related to the doping amount. When the dopant amount was low, the specific surface area exhibited a wide variation range, and the conductivity was generally at a low value; as the doping amount increases, the variation range of the specific surface area is gradually narrowed, and the conductivity is gradually improved. This means that the amount of doping will affect the final properties of the support. The gradually narrowing specific surface area variation range also again showed that Nb doping can improve the anti-sintering ability. Combined with the experimental results of Senoo et al., considering that the overall conductivity of the catalyst will be greatly improved after a large amount of Pt is loaded, we think that in general, when the conductivity is above 10^{-4} S cm^{-1}, it is a usable range. [85] As Hussain et al. reported that, platinum sputtered on Nb-doped TiO_2 films prepared by ALD exhibited excellent activity and durability. At 0.9 V vs. RHE, the mass activity reached a level similar to that of Pt/C, 55 and 53 A g^{-1}, respectively. In terms of durability, after 10,000

durability cycles, $E_{1/2}$ only increased by 4 mV, showing excellent durability. [98] Therefore, without considering the difficulty of Pt deposition, the effect of specific surface area on ORR activity is less than that of electrical conductivity. The support synthesized by the template method with a macroporous showed the high specific surface area and conductivity in a particular case. Unfortunately, such a structure is not suitable for use in single-cell testing, and the macroporous structure is easily damaged due to processes such as hot pressing during the process of making the membrane electrode, which reduces its performance. However, the characteristics of high specific surface area, high electrical conductivity, and low contact resistance help to characterize the intrinsic properties of the supported catalyst metals by expelling some of the factors inherent in oxide particles under half-cell test conditions. Therefore, the support was used to make model catalysts and study the catalysts' degradation characteristics. The related content will be introduced in the third chapter.

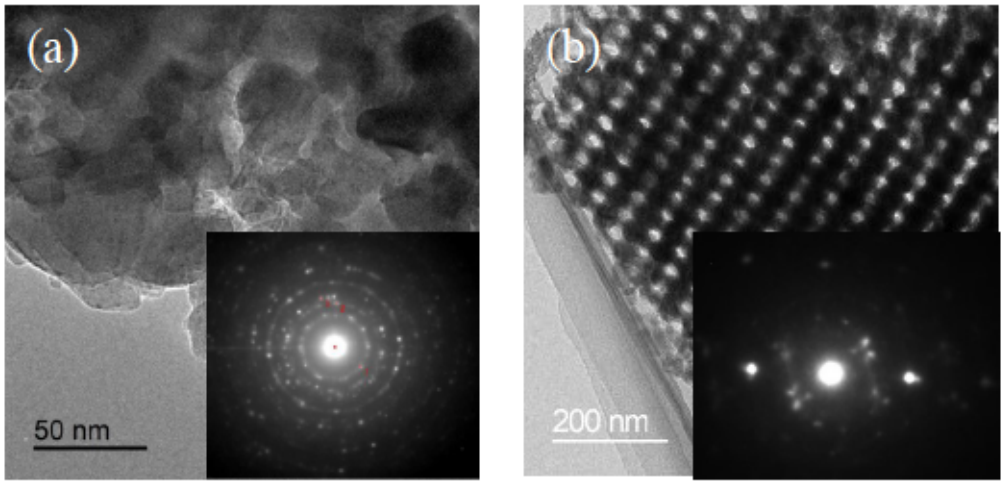

Fig. 2.9 TEM images and ED patterns of (a) nanoparticle 10 at% Nb doped TiO_2 after heating at 600 °C for 5 h under H_2 atmosphere and (b) macroporous Nb doped Ti_4O_7 after heating at 900 °C for 5 h under H_2 atmosphere.

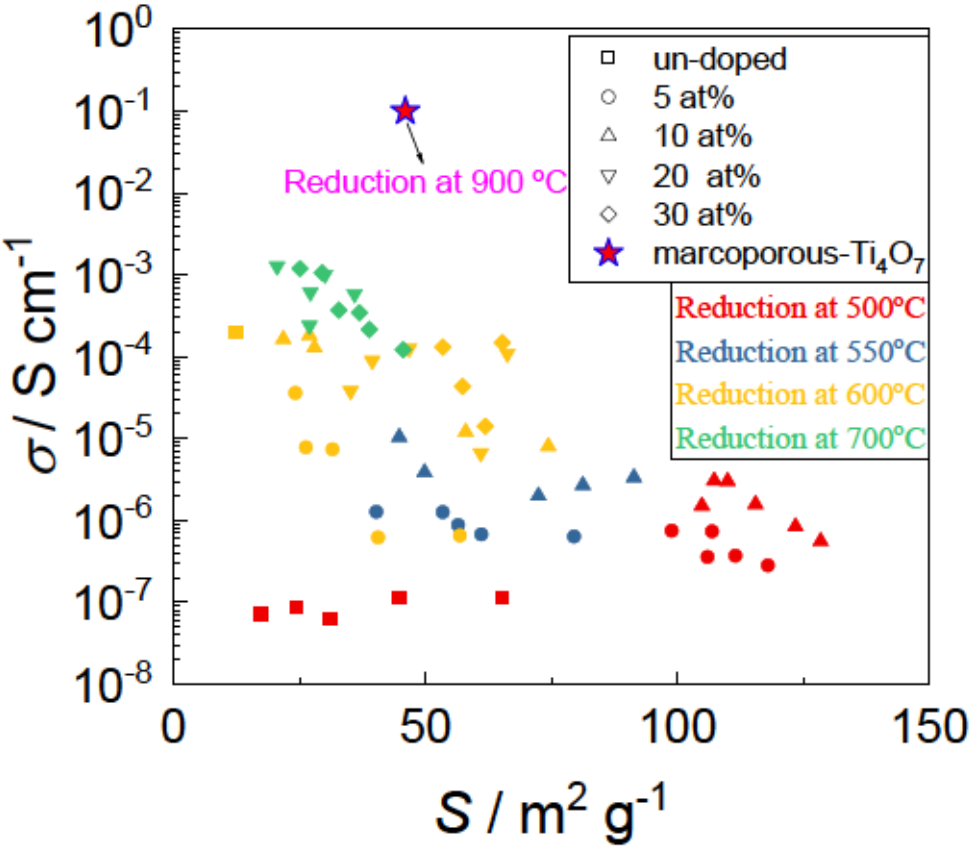

Fig. 2.10 Relationship between the BET surface area and the conductivity of all samples heat-treated under H_2.

Table 2.2 ED pattern

10 at% Nb-doped TiO_2		
Spot#	d-Spacing (nm)	
1	0.3229	rutile
2	0.2521	Ti_3O_5
3	0.2325	anatase or Ti_3O_5

Considering that in the conductivity test, even if high pressure has been applied, there were inevitable pores in the test sample, and the contact resistance between the sample and the sample was also very large, resulting in the measured conductivity value and theoretical conductivity. Here, we corrected the experimental data and calculate the theoretical conductivity of each sample. In this calculation, the theoretical density was calculated from this formula:

$$\rho_{theo}=ZM/NV \tag{2.5}$$

Here, Z is the number of atoms in each unit cell, M is the molar mass, Nis Avogadro's constant, and V is the unit cell volume.

Then calculated the conductivity at full compaction based on the theoretical density, where the change in conductivity at high pressure was assumed to be linear. The Calculation is according to the following formula:

$$\sigma_{theo}=\sigma / \rho_{theo} \tag{2.6}$$

Here, σ was the measured conductivity, σ_{theo} was theoretical conductivity.

Generally, the higher the specific surface area, the easier it is to create a large number of uncompacted gaps. As shown in Fig. 2.11 (a), we calculated the relationship between density and specific surface area. The horizontal axis in the figure is the ratio of the measured density to the theoretical density, and the vertical axis is the specific surface area. There was no obvious correlation between density and specific surface area. The measured density of the supports prepared by the two methods was about half of the theoretical density, indicating that under this test condition, the difference caused by the specific surface area of the sample can be ignored. Figure 2.11 (b) is the relationship between the corrected theoretical conductivity and specific surface area, and the conductivity data of bulk and single crystal films are added for comparison.[99-101] The distribution of electrical conductivity has not changed, and the highest was still the macroporous structure Nb-doped Ti_4O_7. However, compared with the bulk material, the conductivity still has several orders of magnitude difference, which was mainly since the actual synthesized support was not a uniform Ti_4O_7 single phase, which contains part of γ-Ti_3O_5 and anatase TiO_2. Furthermore, we found that when the prepared carrier reaches the level of single crystallinity, its conductivity is expected to be further increased. If a uniform Ti_4O_7 single crystal macroporous structure carrier can be prepared, its electrical conductivity can theoretically reach a very high level.

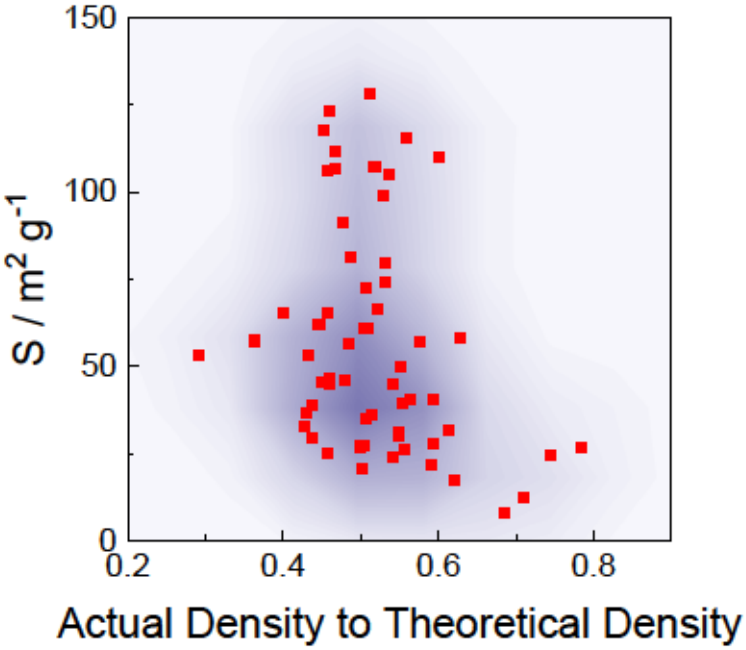

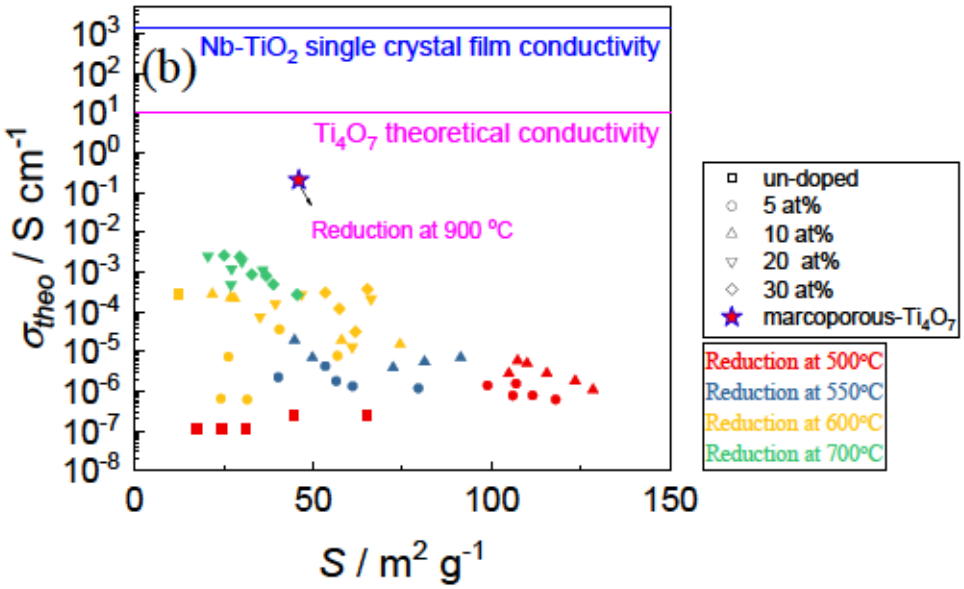

Fig. 2.11 (a) The relationship between the ratio of the measured density to the theoretical density and the specific surface area; (b) relationship between the BET surface area and the corrected conductivity of all samples heat-treated under H_2.

It was necessary to find a suitable parameter that has broad applicability to govern the conductivity. Figure 2.12 shows the typical XPS of (a) Nb3d spectrum of the 30 at% Nb-doped TiO_2 which has been done the heat treatment at 700 °C for 15 min under a pure H_2 atmosphere. The valence states of niobium can be obtained by peak splitting. The proportions of different valences and the ratio of Nb^{4+} (R_{Nb}^{4+}) were calculated from the results obtained by peak separation. Since it is hard to interpret the dependence of the entire conductivity range, we focused on a relatively high conductivity above 10^{-5} S cm^{-1}. Figure 2.12 (b) plotted the conductivity and R_{Nb}^{4+}. A strong correlation can be found between the two parameters. In fact, several factors can affect the conductivity of the support, such as surface state, contact resistance, etc. In the high conductivity range, the contact resistance can be neglected here because the conductivity test was carried out at a pressure of up to 60 MPa, and the specific surface area of the sample was significantly reduced at high temperatures. As we know, Nb-doped TiO_2 is an n-type semiconductor characterized by the carrier density and flat-band potential. For Nb-doped TiO_2 bulk, the semiconductor properties control the ECSA because of the depletion layer formation. [102] Here, A new method based on the physical chemistry of nanoscale metal oxide particles to investigate the electrical conductivity of such small-scale of metal oxides is needed. Furthermore, the influence of semiconductor properties, such as the depletion layer formation, is negligible since Pt nanoparticles deposited onto the metal oxide support cathodic catalyst applications. [103, 104]

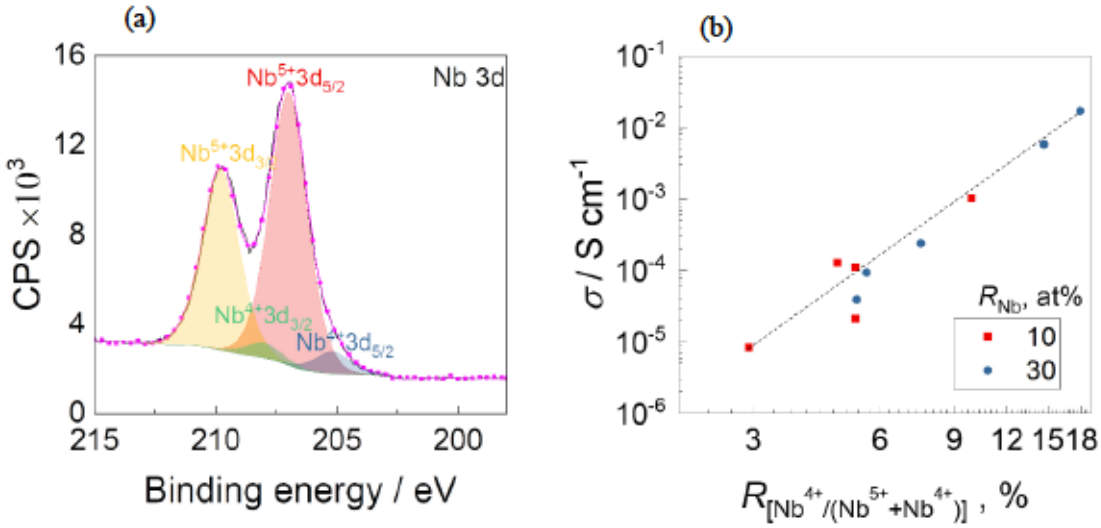

Fig. 2.12 XPS of (a) Nb3d peak of nanoparticle 30 at% Nb-doped TiO_2, which was heated at 700 °C for 15 min under H_2. (b) Relationship between the ratio of Nb^{4+} and the conductivity above 10^{-5} S cm^{-1} in nanoparticle Nb-doped TiO_2 support.

Meantime, we propose the reference conditions for the preparation of conductive nanoparticle Nb-doped TiO_2. As Fig. 2.13 showed that, within the range of BET surface area and conductivity shown in the figure, according to the actual situation such as catalyst loading, etc., high BET specific surface area/low conductivity or low BET specific surface area/high conductivity can be selected. Then, according to the selected specific surface area, the doping amount, heat treatment implementation temperature, and heat treatment implementation time required for preparation can be confirmed in Fig. 2.10 This process is helpful in preparing supports which have controllable BET surface area and conductivity.

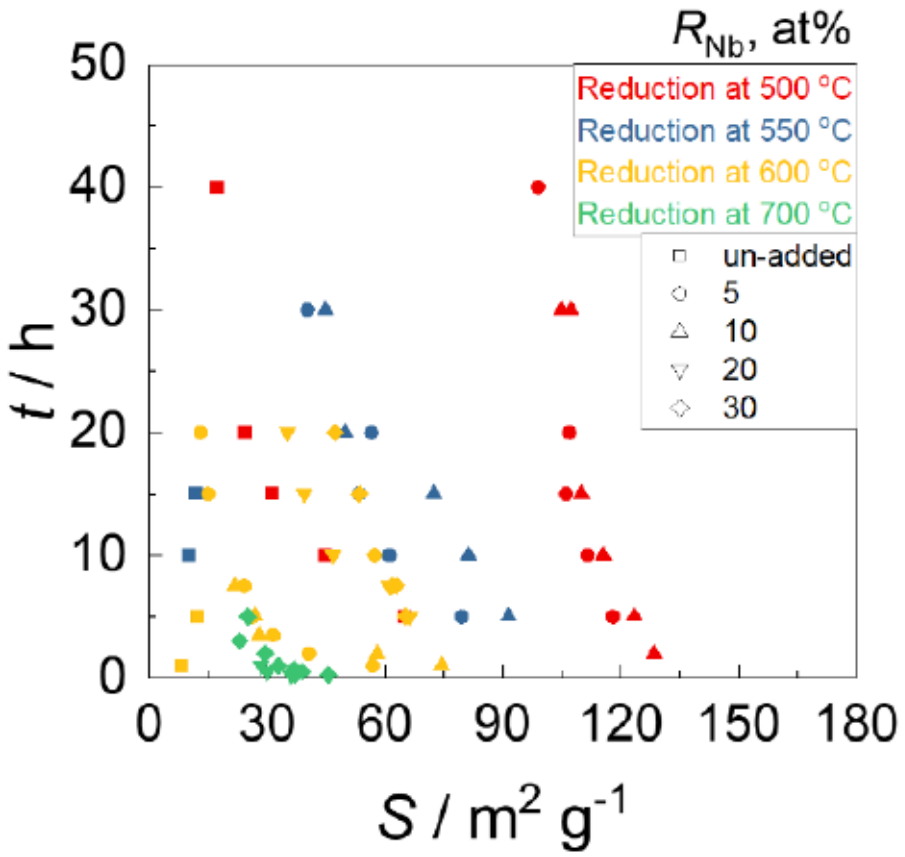

Fig. 2.13 Relationship between the heat-treatment time of all samples and the BET surface area.

A durability test was done as the FCCJ test method. [89] Figure 2.14 (a) 10at% Nb-doped TiO_2, treated at 500 °C for 2 hours under pure H_2 atmosphere, with high specific surface area: 128m^2 g^{-1} and low conductivity: 5.57×10^{-7} S cm^{-1}; (b) 30at% Nb-doped TiO_2, treated at 700 °C for 0.5 hours under pure H_2 atmosphere, with low specific surface area: 39 m^2 g^{-1} and high conductivity: 2.15×10^{-4} S cm^{-1}; (c) Ketjenblack EC-300J, produced by Lion Specialty Chemicals Co., Ltd, which was often utilized as a cathode catalyst support material in PEFC. It could be seen that due to carbon support was oxidized as follows formulation [45]:

$$C+2H_2O \rightarrow CO_2+4H^++4e^- \quad E = 0.207 \text{ V vs. NHE} \tag{2.7}$$

The CV sharp was changed to the glassy carbon rod's CV. Besides, the apparent oxidation current appeared at high potential, which was a disadvantage for PEFC cathode catalyst support. Opposite this, the CV sharp of both conductive oxide support showed not only no noticeable changes happened, but just a little oxidation current at high potential, which meant the titanium conductivity oxide support was harder to be oxidized than the carbon support. Moreover, in Fig. 2.14 (d), the capacitance of oxide support which was calculated in the range of 0.8 - 1.0 V vs. RHE, was almost no changed. The surface state of oxide support had fewer changes than carbon support. 10at% Nb-doped TiO_2 had a higher surface area than 30at% Nb-doped TiO_2 after heat treatment, and the capacitance of 10at% Nb-doped TiO_2 after heat treatment was higher.

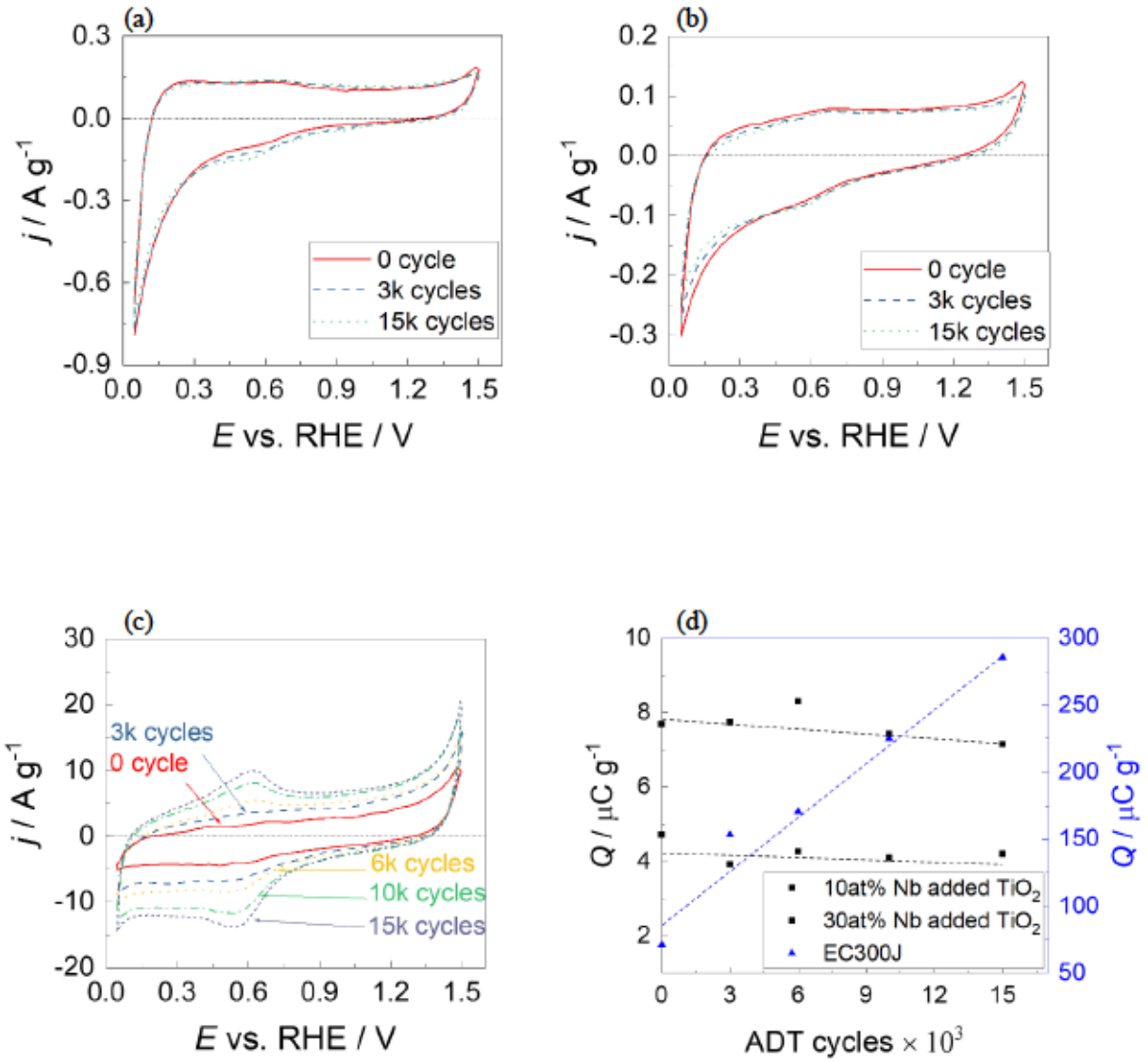

Fig. 2.14 CVs during the ADT of (a) 10at% Nb-doped TiO_2, treated at 500 °C for 2 hours under pure H_2 atmosphere, (b) 30 at% Nb-doped TiO_2, treated at 700 °C for 0.5 hours under pure H_2 atmosphere, and (c) KB in 0.1 M $HClO_4$ under N_2 at 60 °C with a swap rate of 0.5 V s^{-1}. (d) Diversifications in the electric charge of the double layer of 10at% Nb-doped TiO_2 treated at 500 °C for 2 hours under pure H_2 atmosphere, 30 at% Nb-doped TiO_2, treated at 700°C for 0.5 hours under pure H_2 atmosphere, and KB in the given cycle numbers of ADT.

2.4 Conclusion

In this experiment, nanoparticle Nb-doped TiO_2 support and macroporous Nb doped Ti_4O_7 support were successfully synthesized using the hydrothermal method. For nanoparticle Nb-doped TiO_2 support, Conductivity was more affected by heat treatment temperature than heat treatment time when the temperature at 500-700 degrees Celsius; niobium doping can effectively improve the anti-sintering ability during heat treatment, when heat treatment at 600 degrees Celsius, the specific surface area of the undoped sample was higher than that of the undoped sample. The drop was as high as about 90% when the support was undoped, and the 30 at% doped sample only dropped by about 30%. When the dopant amount was 20 at% or above and the temperature was 600 ºC or above, Nb-doped TiO_2 support with 10^{-4} S cm^{-1} or above conductivity could be prepared. For macroporous Nb doped Ti_4O_7 support, due to the effect of crystallization speed, the template method can prepare uniform macroporous Nb-doped Ti_4O_7 support, and the upper limit of dopant of this method was 1 at% in this method; this support had both high specific surface area and conductivity, high conductivity benefitted from the crystal structure and low contact resistance, and this support could be used in low Pt-loading catalyst. The degradation mechanism and Pt behavior on the surface of titanium oxide will be discussed in Chapter 3.

Chapter 3

High durability Pt/Nb-doped Ti_4O_7 carbon-free catalyst in polymer electrolyte fuel cells

3.1 Introduction

In Chapter 2, we have previously reported the synthesis of Nb-doped TiO_2 nanoparticles for use as PEFC cathode supports by the hydrothermal method. In the second chapter, we optimized the preparation method of macroporous structure, adjusted the reduction heat treatment temperature, and successfully prepared macroporous Nb-doped Ti_4O_7. This support will be used in this chapter.

From the viewpoint of stability and ORR activity, titanium oxide-based supports are looked forward to enhancing both the mass activity (MA) and specific activity (SA) of Pt, by the strong metal-support interaction (SMSI). Mukerjee et al. suggested metal-metal and metal-oxygen interactions to propose metal and metal oxide interactions. [106] Lots of studies have reported the interaction between metallic Pt and titanium oxide supports could enhance the MA and durability of Pt. [97-114] In previous research of macroporous Ti_6O_{11} supports, Pt was deposited with the arc plasma deposition (APD) method. [92] Due to the high charge energy of APD, APD-deposited Pt nanoparticles have some unique attributes like controllable particle size [115, 116], high activity [105, 117], and high stability. [105, 118] In the previous research, it exhibited a relatively high SA which reached 6.01 A m^{-2} at 0.9 V vs. RHE. [69] Although the high durability of Pt/titanium oxide catalysts has been widely researched, the explanation for the high performance is not enough. Thus, the deterioration principle of the Pt/metal oxide catalyst has not been widely discussed yet.

To clear the physical properties and degradation characteristics of platium metal in Pt/Ti oxide-based catalysts, we used macroporous Nb-doped Ti_4O_7 [69, 105], which had a low contact resistance as a support, deposited different mass percentages of Pt by APD method to make model catalysts, its degradation characteristics were studied in an acidic environment with a half cell.

3.2 Experimental

3.2.1 Preparation of Pt/Nb-doped Ti_4O_7 electrodes

Pt nanoparticles were deposited onto the surface by arc plasma deposition (APD) method as follows. 4 mg Nb-doped Ti_4O_7, which was introduced in Chapter 2, were suspended in 400 μL 1-hexanol (97%, Wako) by ultrasonic for 20 min to prepare the Nb-doped Ti_4O_7 support powder ink. Next, 10 μL powder ink was cast onto the GC working electrode, with 5.2 mm diameter, and dried at 60 °C for 1h in air. For Pt deposition, APD (APD-P, ADVANCE RIKO, Inc.), with 100 V discharge voltage, 1080 μF capacitor capacity, 3 Hz frequency, and 6.7×10^{-3} Pa (O_2) chamber pressure. Pt amount was adjusted by shot number. Pt/Nb-doped Ti_4O_7 catalyst with the Pt loading amount of 2 wt%, 5 wt%. and 10wt% (ICP-AES) was used for the electrochemical studies.

Since the Pt/Nb-doped Ti_4O_7 catalysts cannot be uniformly dispersed by sonication, Nafion® was not considered to cover their surfaces. In addition, so as to reduce interference on the Pt surface, Nafion® was not used in the preparation of Pt/Nb-doped Ti_4O_7/GC working electrodes. As a contrast, the commercial Pt/C (TEC10E50E, Tanaka Kikinzoku Kogyo) catalyst was used as a control group. The amount of Nafion® doped was halved according to the FCCJ standard method. [89]

3.2.2 Physical characterization

The morphology of supports and catalysts were observed via Scanning Transmission Electron Microscope (STEM, Cs-corrected STEM HD-2700. Accelerating voltage: 200 kV, HITACHI). The evaluation of the catalysts' electric structure before and after ADT was investigated by X-ray photoelectron spectroscopy (XPS, Quantum-2000, PHI). The C–C bond peak attributed to free carbon at 284.8 eV in the C 1s spectrum was used to compensate for the surface charging. The peak areas of the Pt 4f 7/2 and Pt 4f 5/2 components were fixed at 4:3, and a theoretical split of 3.33 eV was used. [119-125]

3.2.3 Electrochemical characterization

Electrochemical was conducted by a 3-electrode cell in 300 mL, 0.1 M $HClO_4$ electrolyte with a potentiostat (PS08, TOHO Technical Research). Counter electrode and reference electrode were

served by a GC plate and an RHE, respectively.

An accelerated durability test (ADT) was conducted at a potential scan rate of 0.5 V s^{-1} within the potential range at 1.0 - 1.5 V vs. RHE at 60 °C, according to the start/stop durability test for a given number of cycles, that recommended by the FCCJ. [89]

CVs were carried out in 300mL, 0.1 M $HClO_4$ solution with saturant nitrogen bubbling at 60 °C, with a swap rate of 0.5 V s^{-1}. The ECSA was calculated by measuring the integration of the electrical charge on the hydrogen desorption (Q_H) from 0.05 V to 0.4 V in the CVs. The conversion factor (q_H = 0.21 mC cm^{-2}) was used to measure the corresponding surface areas. The ECSA was calculated as the following equation:

$$\text{ECSA} = \frac{Q_H}{m \times q_H} \tag{3.1}$$

Here, Q_H is the electrical charge, m is the weight of Pt, and q_H is the conversion factor for monolayer theoretical adsorption value of H_2 on the Pt surface.

The ORR slow-scan voltammetry (SSV) measurements were performed in 0.1 M $HClO_4$ under saturant oxygen bubbling during the ADT with a 5 mV s^{-1} scan rate and 0.2 – 1.2 V scan range. In order to remove as much interference as possible for getting stable curves, 4 cycles of SSV were carried out, and the fourth cycle was used for calculation generally.

3.3 Results and discussion

3.3.1 Physical characterization of Pt/Nb-doped Ti_4O_7 catalysts

Figure 3.1 (a1), (b1), and (c1) showed the annular dark-field STEM (ADF–STEM) images of the Pt/Nb-doped Ti_4O_7 catalysts with the Pt loading as 2, 5, and 10 wt% which were before the electrochemical test. For each catalyst, from the STEM photos, it can be found that Pt was deposited on the Nb-doped Ti_4O_7 support surface. Due to the fixed relative positions of the Pt target and the electrode, it was difficult for Pt to be uniformly distributed on the support surface. The morphology, size, and density of platinum are affected by the number of APD depositions. Specifically, for the 2 wt% Pt loading catalyst, due to the high charge energy applied in APD[126], Pt may interact strongly with the oxide support, and form the disordered hemispherical particles, which were shown in Fig. 3.1 (a1) and Fig. 3.2 (a and b), and as the image in Fig. 3.1 (a3), the bottom surface average diameter of the contact area/hemisphere was 1.4 nm. When the deposition amount reached to 5 wt%, the morphology was changed from hemispherical to island-like (Fig. 3.1 (b1) and 3.3 (a and b)). Further, When the Pt loading amount was added to 10 wt%, it tent to be film-like (Fig. 3.1 (c1) and 3.4 (a and b)). It can be found that as the amount of Pt deposition increases, the morphology of Pt tent to be flatter. Here, it was not adequate to use the average particle size to represent the size of island-like and thin-film Pt deposits; therefore, the average thickness is used in this study, and the average thicknesses of the catalysts are 2.4 and 3.3 nm, respectively (Fig. 3.1(b3) and (c3)). For APD-deposited Pt, the morphological characteristics of Pt are mainly extended in the horizontal direction with the increase of the deposition amount, and the increase in the vertical direction was minimal. The difference between the 5 and 10 wt%_Pt/Nb-doped Ti_4O_7 catalysts is their ratio of the edge–to–plane in Pt deposits.

Figure 3.1(a2, b2, c2) are the ADF-STEM images of the Pt/Nb-doped Ti_4O_7 catalyst after electrochemical testing. As shown in Fig. 3.1(a2), (a3), and 3.2(c, d), the Pt nanoparticles at 2 wt%_Pt/Nb-doped Ti_4O_7 were agglomerated, and the average bottom diameter increased to 3.5 nm. For 5 wt%_Pt/Nb-doped Ti_4O_7, some Pt deposits connected and formed the chain bead-like and the mean. thickness increases from 2.4 nm to 4.0 nm, which are shown in Fig. 3.1(b2), (b3), and 3.3(c and d). For 10 wt%_Pt/Nb-doped Ti_4O_7, as shown in Fig. 3.1(c2), (c3), and 3.4(c and d), the morphology

was still film-like after electrochemical testing, and the thickness is slightly increased to 4 nm.

Figure 3.5 reveals the comparison of the average size before and after the electrochemical test. Although the thickness increased slightly, it did not agglomerate into large particles, and the APD deposited Pt deposits did not thicken over 4 nm, indicating that 4 nm may be the APD deposition stable thickness. The island-like Pt was not connected to form film-like Pt with large planes, which may be considered that ascribed to the strong interaction between Pt and Nb- Ti_4O_7 produced by APD. This distinctive morphological change may be owing to the surface energy of the crystal planes, which leads to the difference in Pt affinity. [126, 127]

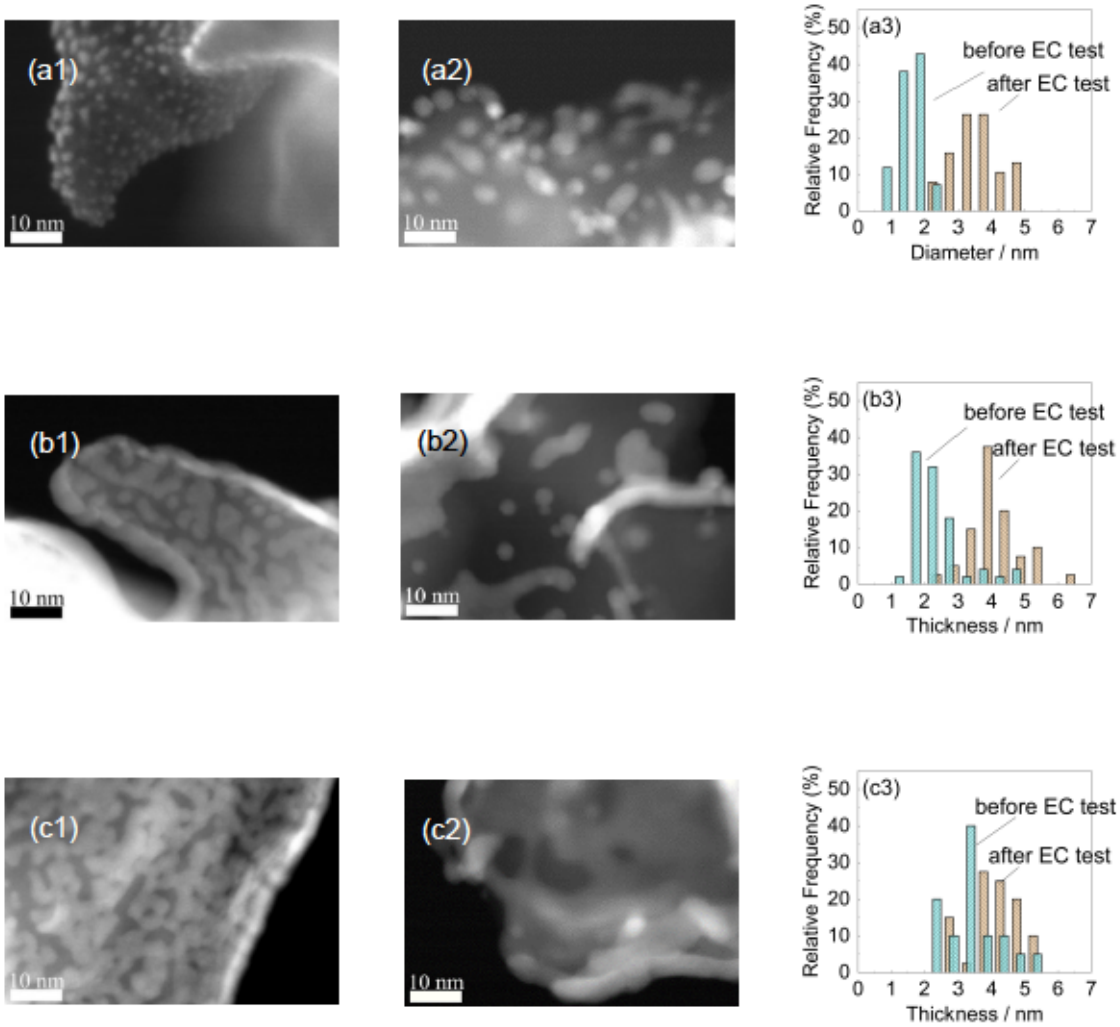

Fig. 3.1. ADF–STEM images of Pt/Nb-doped Ti_4O_7. (a1) 2 wt%_Pt/Nb-doped Ti_4O_7 images before the electrochemical test, (a2) 2 wt%_Pt/Nb-doped Ti_4O_7 images after the electrochemical test, (b1) 5 wt%_Pt/Nb-doped Ti_4O_7 images before the electrochemical test, (b2) 5 wt%_Pt/Nb-doped Ti_4O_7 images after electrochemical test, (c1) 10 wt%_Pt/Nb-doped Ti_4O_7 images before the electrochemical test, (c2) 10 wt%_Pt/Nb-doped Ti_4O_7 images after electrochemical test, (a3, b3, c3) bottom diameter distribution or thickness distribution of Pt deposits before and after the electrochemical test.

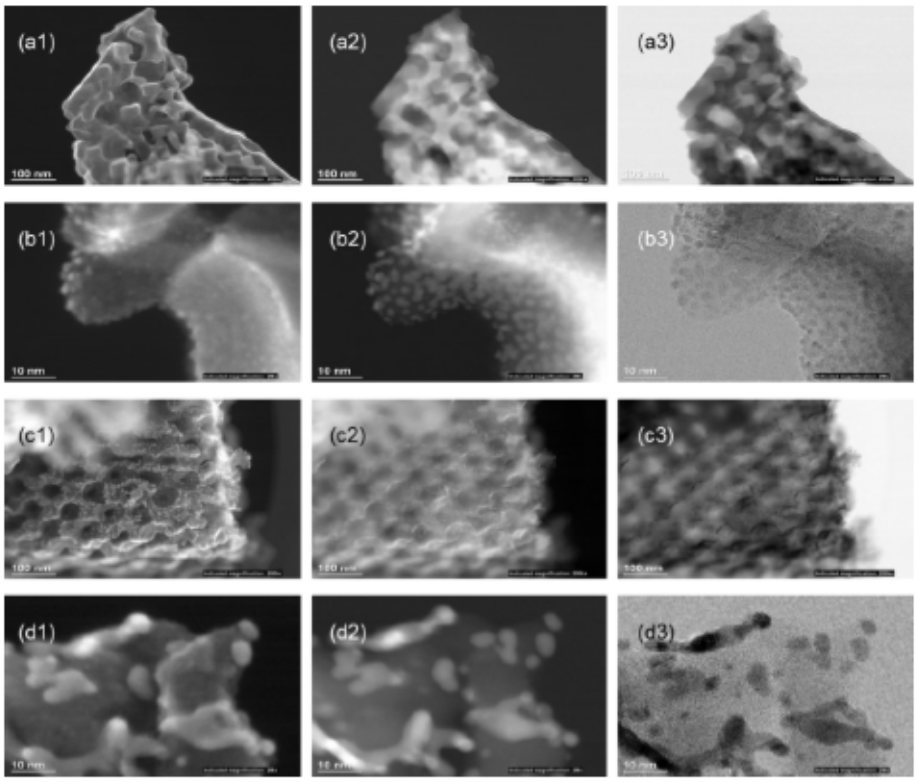

Fig. 3.2. STEM images of 2 wt%_Pt/Nb-doped Ti_4O_7: (a1, b1) SEM images before electrochemical test, (a2, b2) ADF–STEM images before electrochemical test, (a3, b3) BF–STEM images before electrochemical test, (c1, d1) SEM images after electrochemical test, (c2, d2) ADF–STEM images after electrochemical test, (c3, d3) BF–STEM images after electrochemical test.

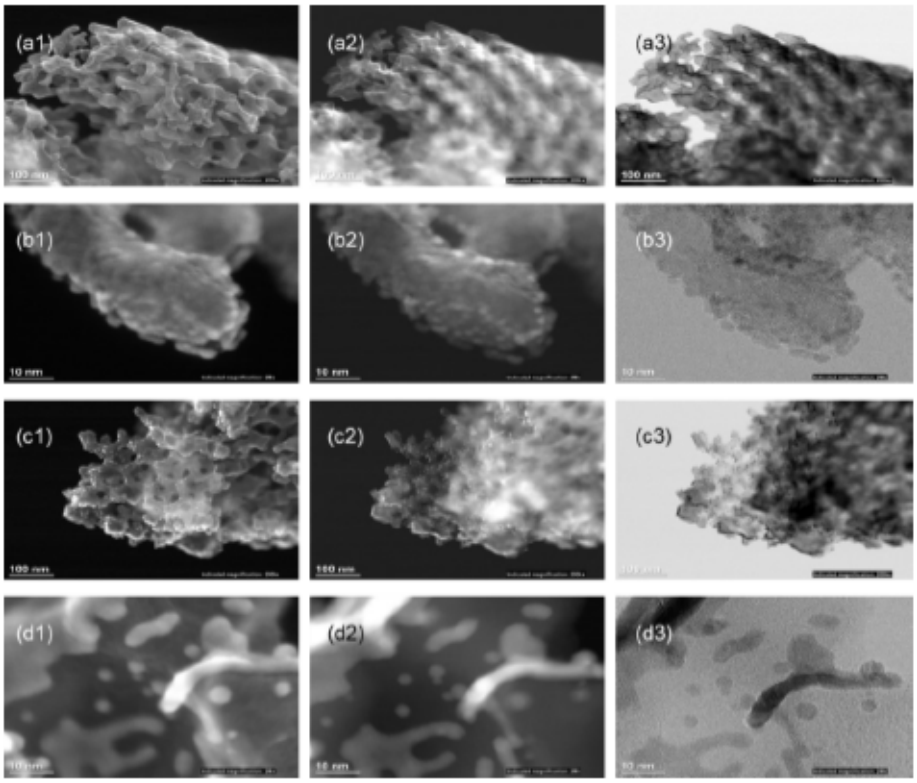

Fig. 3.3. STEM images of 5 wt%_Pt/Nb-doped Ti_4O_7: (a1, b1) SEM images before electrochemical test, (a2, b2) ADF–STEM images before electrochemical test, (a3, b3) BF–STEM images before electrochemical test, (c1, d1) SEM images after electrochemical test, (c2, d2) ADF–STEM images after electrochemical test, (c3, d3) BF–STEM images after electrochemical test.

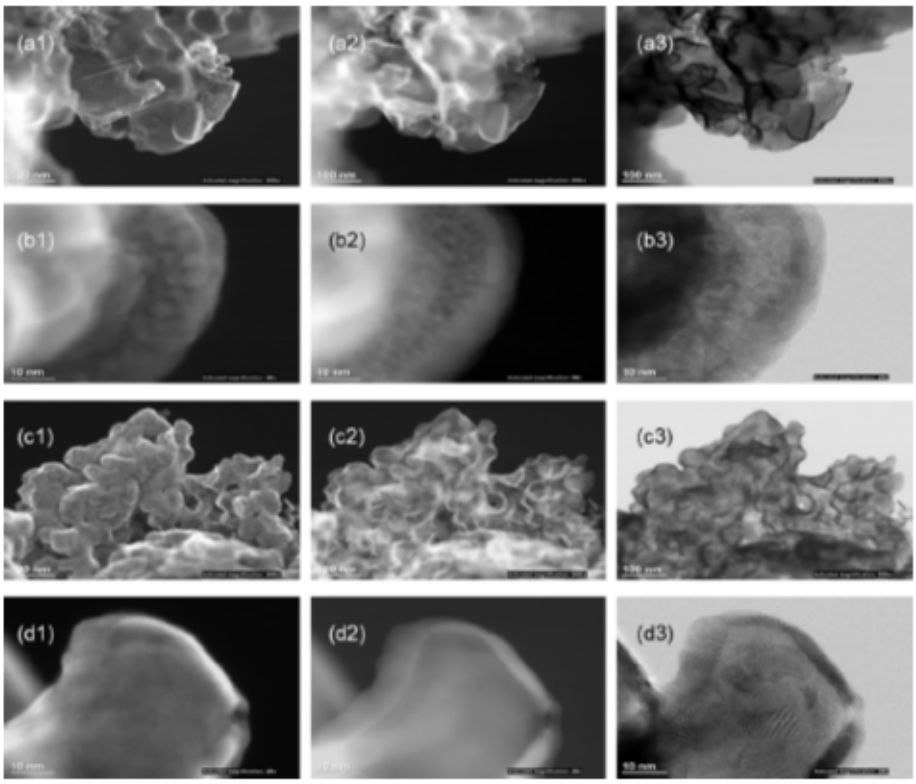

Fig. 3.4. STEM images of 10 wt%_Pt/Nb-doped Ti_4O_7: (a1, b1) SEM images before electrochemical test, (a2, b2) ADF–STEM images before electrochemical test, (a3, b3) BF–STEM images before electrochemical test, (c1, d1) SEM images after electrochemical test, (c2, d2) ADF–STEM images after electrochemical test, (c3, d3) BF–STEM images after electrochemical test.

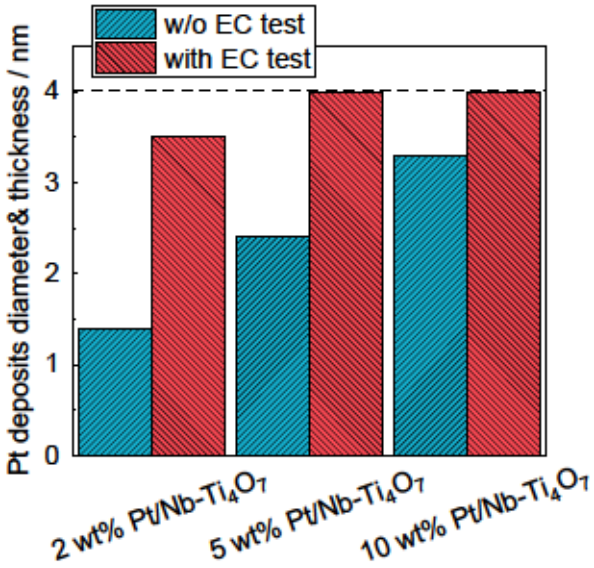

Fig. 3.5. The diameter and thickness of Pt deposits of Pt/Nb-doped Ti_4O_7 before and after the electrochemical test.

Figures 3.6 (a-d) are the CV changes of the catalysts during ADT. The prime CVs of all the catalysts exhibited representative Pt characteristic curves. About the strong hydrogen adsorption peak, especially in 2 wt% Pt/Nb-doped Ti_4O_7, it was suggested that some adsorbed hydrogen would transfer onto the support by spillover. [128-130] As the report, Pt-TiO_2 has a factor for measurement of spillover range from 1.7 to 2.0, and the experimental value with a smaller particle size showed a higher factor for measurement of spillover intensity. [129, 130] Miyazaki et al. suggest that GC rod which irradiated by Pt ions was damaged to depths up to 17 nm from the top of the GC rod surface. [131] It could be considered that some of the Pt nanoparticles penetrated the Nb-doped Ti_4O_7 support and formed the flat Pt deposits. Thus, hydrogen spillover was occured in 2 wt%_Pt/Nb-doped Ti_4O_7. In addition, about the anomalous peak at 0.6 – 0.65 V vs. RHE, A. Sleightholme et al. have suggested possible explanations that the origin of this peak would be the oxide species were formed on the Pt surface. The strength of this peak had a tendency to be greater at a higher temperature. [132] As shown in Fig. 3.6 (c), 10 wt%_Pt/Nb-doped Ti_4O_7 shows a redox peak around 0.31 V in 0.1 M $HClO_4$. Since the Pt morphology tent to be film-like as the deposition amount increases, the Pt (1 0 0) face would be extended, which explained the appearance of the redox peak around 0.31V in 0.1 M $HClO_4$. [133] Meanwhile, in the CV of 5 wt%_Pt/Nb-doped Ti_4O_7, there is a hydrogen adsorption-desorption peak around 0.1 V, which is caused by Pt(1 1 0) in 0.1 M $HClO_4$. [133] In conclusion, the ratio of Pt(1 1 0) to Pt(1 0 0) in 5 wt%_Pt/Nb-doped Ti_4O_7 was higher than 10 wt%. The change in shapes of CVs of all Pt/Nb- Ti_4O_7 catalysts was smaller than Pt/C, reflecting higher durability. Further, V. Komanicky et al. reported that structural changes on the surface of Pt single crystals with low Miller indices occur during potential cycling in acidic media, and Pt(1 1 0) is hardly dissolved in potential range at 0.65 V - 1.15 V vs. RHE. It explained this smaller change in morphology of catalysts with a high deposition amount. [134]

Figures 3.6 (e–h) show the decrease of ECSAs during the ADT. The initial ECSAs of Pt/Nb- Ti_4O_7 and Pt/C catalysts with deposition amounts of 2, 5, and 10 wt% were 45, 29, 28, and 91 m^2 g^{-1}, respectively. The ECSA of 5 and 10 wt%_Pt/Nb- Ti_4O_7 were small due to the island-like and film-like Pt. The ECSA of 2 wt%_Nb- Ti_4O_7 decreased rapidly in the first 1000 ADT cycles and then stabilized, which was caused by the slight agglomeration of Pt in 2 wt%_Nb- Ti_4O_7 in the early ADT. 5 and 10 wt%_Pt/Nb- Ti_4O_7 catalysts exhibited a high ECSA durability. In total, Pt deposited by APD would

slightly agglomerate in ADT. Unlike Pt/C catalysts, Pt did not agglomerate into large-diameter spherical particles but tent to connect horizontally, and conformity films.

Figures 3.6 (i–l) are the position of oxide reduction peak potential ($E_{Pt-O\ Reduction}$) during the ADTs. $E_{Pt-O\ Reduction}$ reveals the adsorption energy for oxygenated species, which is related to blocking active sites of ORR activity. [135, 136] As the images in Figs. 3.6 (m–p), before the ADTs, Pt/Nb-doped Ti_4O_7 catalysts had higher $E_{Pt-O\ Reduction}$ than Pt/C. The shift to the high potential side means a adsorption energy decline for the oxygenated species. With Pt deposits size increased, the $E_{Pt-O\ Reduction}$ would shift to the higher potential, but the potential shift extents were more petite than Pt/C. This also shows that Pt/Nb- Ti_4O_7 has good durability. Figure 3.7 plotted the relationship between ECSAs and the $E_{Pt-O\ Reduction}$. The plots with the green right–hand and blue upper are the data of the before and after ADT, respectively. Comparable to previously reported results, a smaller Pt size leads to larger ECSA and more vital oxygen adsorption capacity, which would form stronger Pt–O bonds. [106]

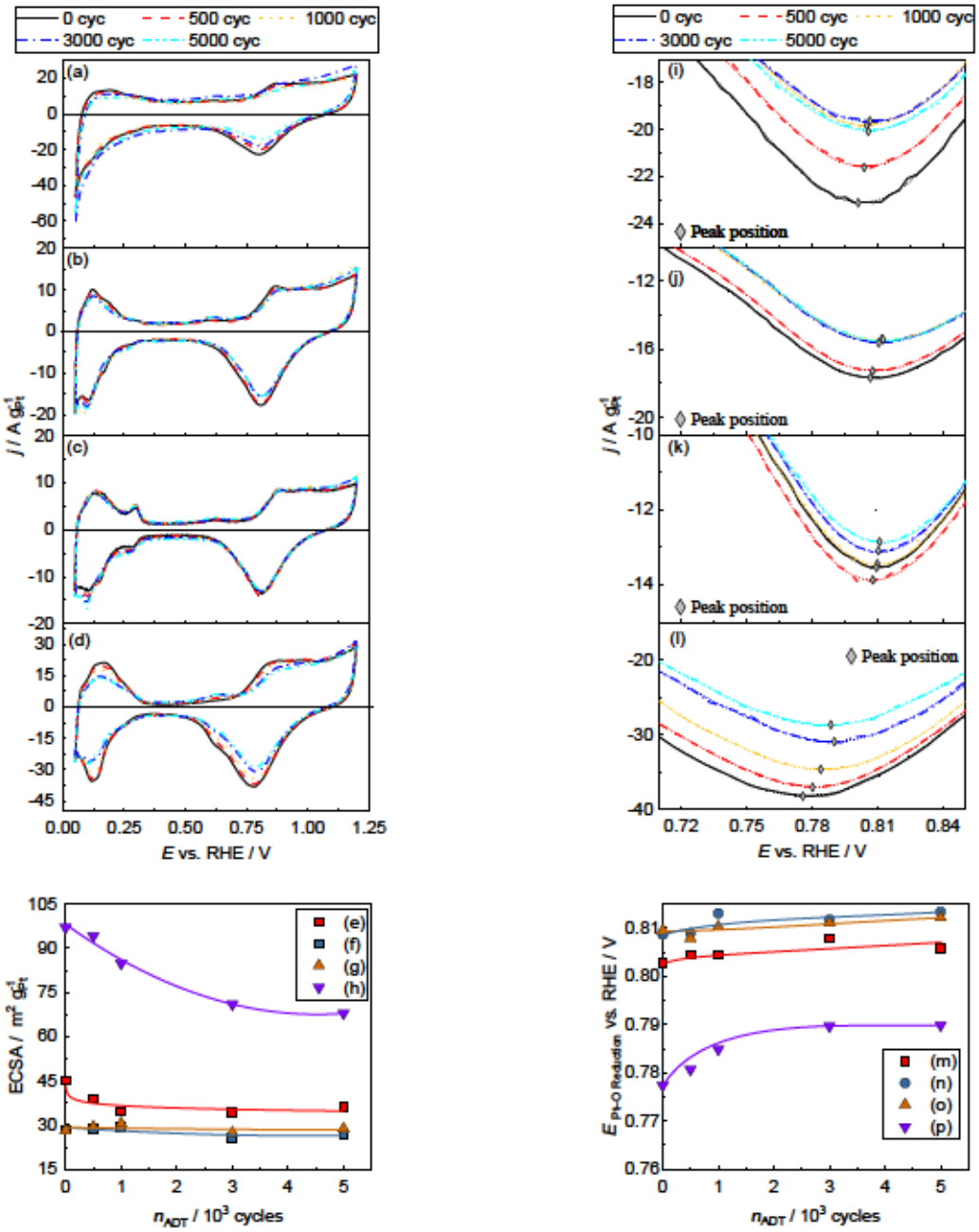

Fig. 3.6. CVs of (a) 2 wt%_Pt/Nb-doped Ti_4O_7, (b) 5 wt%_Pt/Nb-doped Ti_4O_7, (c) 10 wt%_Pt/Nb-doped Ti_4O_7, and (d) Pt/C during ADT; decrease in ECSAs (e) 2 wt%_Pt/Nb-doped Ti_4O_7, (f) 5 wt%_Pt/Nb-doped Ti_4O_7, (g) 10 wt%_Pt/Nb-doped Ti_4O_7, and (h) Pt/C as a function of ADT cycles (n_{ADT}); Pt–O reduction peak shifts of (i) 2 wt%_Pt/Nb-doped Ti_4O_7, (j) 5 wt%_Pt/Nb-doped Ti_4O_7, (k) 10 wt%_Pt/Nb-doped Ti_4O_7, and (l) Pt/C during ADTs and the shifts in Pt–O reduction peaks of (m) 2 wt%_Pt/Nb-doped Ti_4O_7, (n) 5 wt%_Pt/Nb-doped Ti_4O_7, (o) 10 wt%_Pt/Nb-doped Ti_4O_7, and (p) Pt/C as a function of ADT cycles (n_{ADT}).

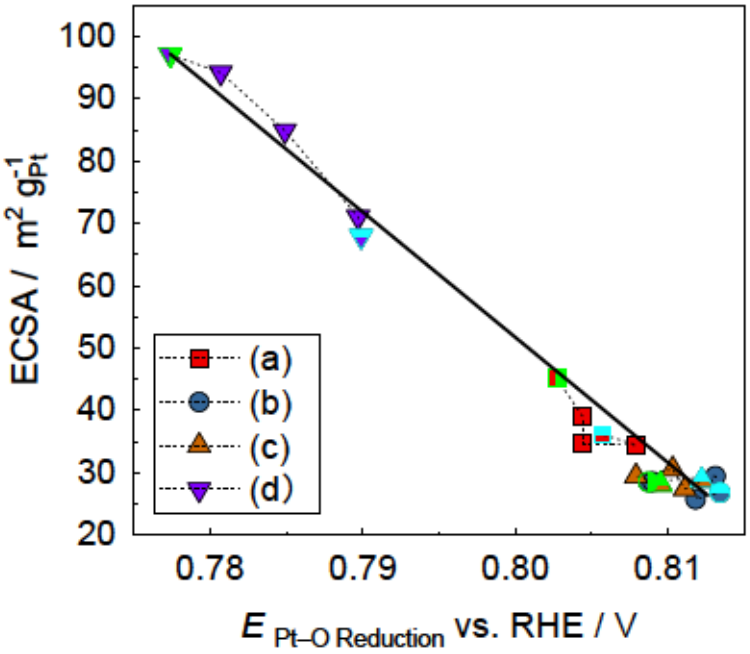

Fig. 3.7. Decline in ECSAs with $E_{\text{Pt-O Reduction}}$ shift to high potential side during ADTs (a) 2 wt%_Pt/Nb-doped Ti_4O_7, (b) 5 wt%_Pt/Nb-doped Ti_4O_7, (c) 10 wt%_Pt/Nb-doped Ti_4O_7, and (d) Pt/C.

Figures 3.8 (a–d) show the Tafel plots of the MAs during ADTs, and the decreases of the MA and SA at 0.9 V vs. RHE with ADT are shown in Figs. 3.8 (e–h) and (i–l). the initial MAs for the ORR of 2, 5, 10, and Pt/C at 0.9 V are 117 A g^{-1}, 72 A g^{-1}, 36 A g^{-1}, and47 A g^{-1}, respectively. Due to the fine Pt deposits size of Pt/C catalyst, its SA was relatively low. For 2 and 5 wt%_Pt/Nb- Ti_4O_7, although the ECSA was smaller than Pt/C, the MA was high due to the high SA. SMSI between Pt and oxide supports of 2 wt%_Pt/Nb-doped Ti_4O_7 enhanced ORR activity. [107] The SA of 10 wt%_Pt/Nb-doped Ti_4O_7 was about half as much as the 2 wt% catalysts, because the former had a larger Pt(1 0 0) plane area and a relatively lower SA for ORR. From the CV shape, it can be qualitatively analyzed that the ratio of Pt(1 1 0) to Pt(1 0 0) in 5 wt%_Pt/Nb- Ti_4O_7 is higher than the 10 wt% sample. In addition, SA in 0.1 M $HClO_4$ increased in the order of Pt (1 1 0) > Pt (1 1 1) > Pt (1 0 0). [133] This made 5 wt%_Pt/Nb-doped Ti_4O_7 have high SA. As Fig. 3.8 (e) showed, the MA of the 2 wt%_Pt/Nb-doped Ti_4O_7 catalyst decreased in the first 1000 cycles and stabilized after that. In Fig. 3.8(i), in spite of the SA of 2 wt%_Pt/Nb- Ti_4O_7 has a limited decrease, its MA decreased significantly, which was due to the decrease of both ECSA and SA. In contrast, although the ECSA of Pt/C had fallen sharply, its MA has continued to decline. The SA increasing of Pt/C caused this with the increase of Pt deposits size. When 2 wt%_Pt/Nb- Ti_4O_7 was smaller than 2 nm, there was an SMSI between Pt and Nb- Ti_4O_7. As Pt agglomerates, the interaction became weak, decreasing SA by degrees. After 1000 ADT cycles, both ECSA and SA were almost stabilizing, and SA dropped to be the same as that of the 5 wt% sample.

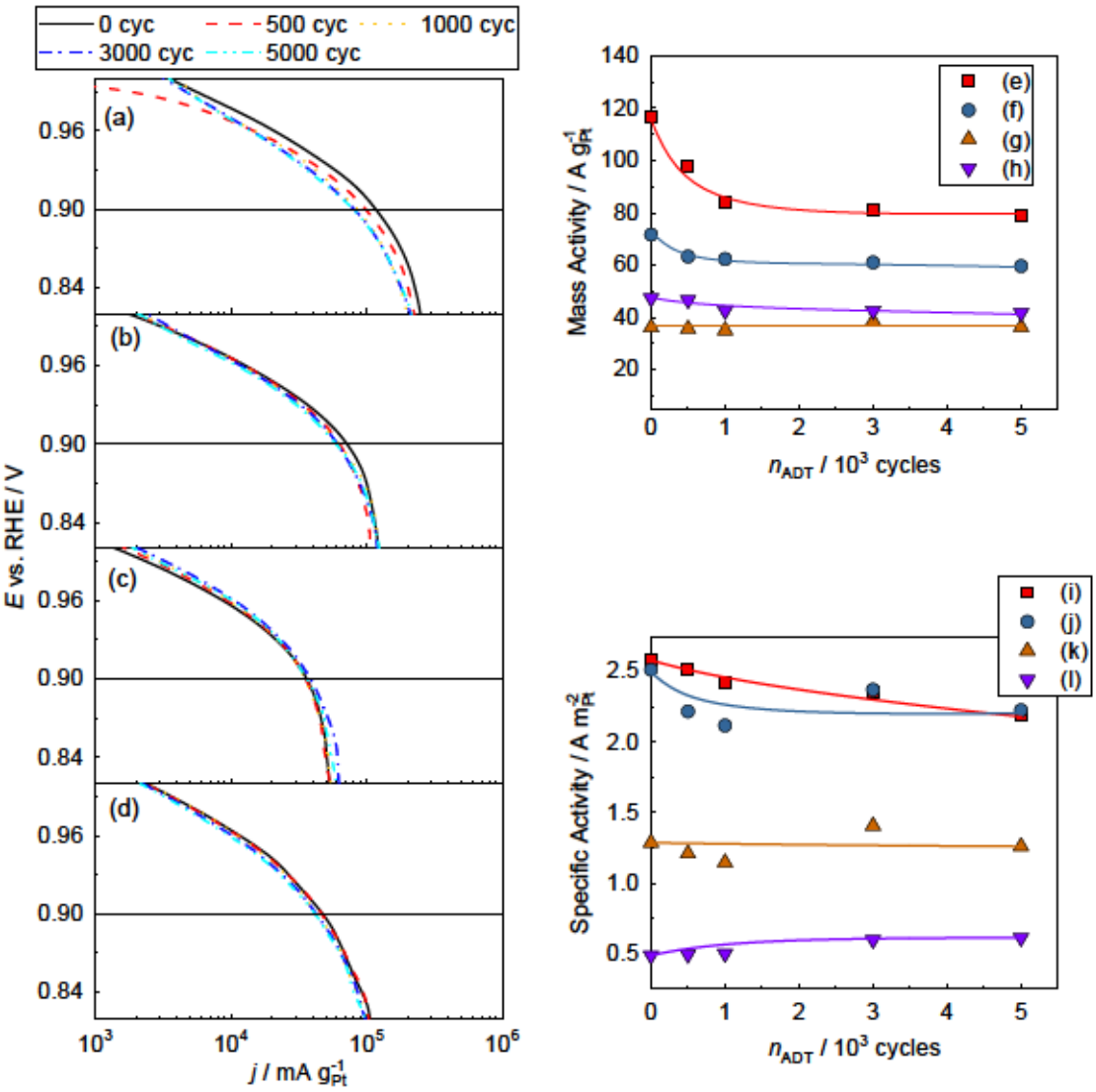

Fig. 3.8. Tafel plots of MA of Pt/Nb-doped Ti_4O_7 and Pt/C during ADTs, (a) 2 wt%_Pt/Nb-doped Ti_4O_7, (b) 5 wt%_Pt/Nb-doped Ti_4O_7, (c) 10 wt%_Pt/Nb-doped Ti_4O_7, and (d) Pt/C; the decrease of MA at 0.9 V vs. RHE as a function of ADT cycles (n_{ADT}): (e) 2 wt%_Pt/Nb-doped Ti_4O_7, (f) 5 wt%_Pt/Nb-doped Ti_4O_7, (g) 10 wt%_Pt/Nb-doped Ti_4O_7, and (h) Pt/C; and decrease in SA at 0.9 V vs. RHE as a function of ADT cycles (n_{ADT}): (i) 2 wt%_Pt/Nb-doped Ti_4O_7, (j) 5 wt%_Pt/Nb-doped Ti_4O_7, (k) 10 wt%_Pt/Nb-doped Ti_4O_7, and (l) Pt/C.

As mentioned above, the different point in agglomeration between the Pt/Nb- Ti_4O_7 catalysts may be aroused by the difference in affinity. Sheng et al. have reported the relationship of surface energy of Pt that {111} < {100} < {110} facet. [126, 137] Herein, the order of surface energies can be considered as 5 wt% > 10 wt% > 2 wt%_Nb-doped Ti_4O_7. Further, high surface energy results in support retention by bonds, which leads to the support being easily wetted. [138]

Meanwhile, Nie et al. reported the spatial heterogeneity of electron transfer on a metallic nanoplate prism. [139] When the interfacial electric field is varied according to the microdynamics model, the dipole moment and polarizability of the intermediate species can be modified, leading to locally enhanced electron transfer at its corners and edges. Due to 5 wt%_Nb-doped Ti_4O_7 having a higher ratio of edge to plane than 10 wt%_Nb-doped Ti_4O_7, and from the morphology, chain-like Pt in 5 wt%_Nb-doped Ti_4O_7 had more corners, which would lead to higher ORR current.

Figure 3.9 exhibits the relationship between the ECSA and SA of the catalysts. The plots with the green right–hand and blue upper are the data of the initial and after ADT, respectively. Here, the curve was drawn according to the initial SA × actual ECSA = 47, which could be fitted with the data of Pt/C catalysts for comparison. [83, 140] The plots on the high ECSA side of the curve indicate that the initial Pt/C MA was more significant, and the trajectories of each catalyst showed its electrochemical durability. The trajectory of Pt/C moved away from the curve, which means that the MA of Pt/C piecemeal decreases from its initial value. The trajectories of 2 and 5 wt%_Pt/Nb-doped Ti_4O_7 were always on the right side of the curve, indicating that their MA is still higher than the initial MA of Pt/C after ADT. Table 3.1 summarized the catalysts' original electrochemical performance and durability and compared them with the reported results.

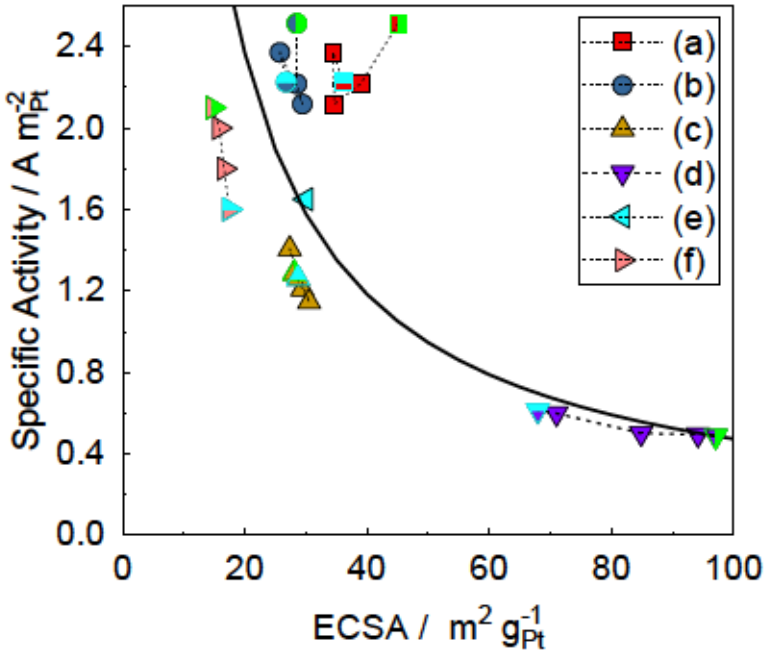

Fig. 3.9. Effects of ADT showing specific activity increase with ECSA decreasing at 0.9 V of (a) 2 wt%_Pt/Nb-doped Ti_4O_7, (b) 5 wt%_Pt/Nb-doped Ti_4O_7, (c) 10 wt%_Pt/Nb-doped Ti_4O_7, (d) Pt/C in this work, (e) Pt/oxide catalyst in ref 113, and (f) Pt/oxide catalyst in ref 140. The "green right–hand half" triangles are the initial results, and the "blue upper half" triangles are after 5000 cycles of ADT. The curve was drawn based on the data of Pt/C catalysts in this study and in ref 100.

Table 3.1. Comparison with other Pt/metal oxides catalysts

	Support	Pt wt%	Before ADT ECSA $m^2 g^{-1}$	Before ADT MA $A g^{-1}$ @ 0.9 V vs. RHE	Before ADT SA $A m^{-2}$ @ 0.9 V vs. RHE	After ADT ECSA $m^2 g^{-1}$	After ADT MA $A g^{-1}$ @ 0.9 V vs. RHE	After ADT SA $A m^{-2}$ @ 0.9 V vs. RHE	ADT
This study@ 60 °C	Nb-doped Ti_4O_7	2	45	117	2.59	36	79	2.19	1.0–1.5 V 500 mV s^{-1} (5k cyc)
		5	29	72	2.51	27	60		
	Ketjen black	10	28	36	1.29	29	36		
		46.43	97	47	0.49	68	41		
Ref (140)	Nb-doped TiO_2 Fibers	40 ALD cycles	14.74		2.1			1.6	0.6–1.0 V 100 mV s^{-1} (30k cyc)
Ref (114) @ 25 °C	TiO_2	20	14.17	1.83	0.129		1.02		0.6–1.0 V 25 mV s^{-1} (5k cyc)
	TiO_2–HT *HT=heat treatment*		10.22	1.01	0.099		3.69		
	TiO_2–HFT *HFT=heat treatment and hydrofluoric acid treatment*		15.19	4.23	0.276				
	TiO_2–FT *FT=directly hydrofluoric acid treatment*		15.67	2.07	0.132				
	$TiNbO_2$			13	0.65				
	$TiNbO_2$–HFT			24	1.3				
Ref (109) @ 25 °C	TiO_x	17.93		1.37	0.49		0.47		0.6–1.0 V 25 mV s^{-1} (5k cyc)
		18.03		0.97	0.35				
Ref (113) @ 25 °C	Nb-doped TiO_2	20	42.5	70	1.65				
Ref (83)	Ti_4O_7	39.28	39.28		9.73				

3.3.2 Electronic states of Pt/Nb-doped Ti_4O_7

At first, we determined the stability of the carrier before and after durability by XPS. Since the amount of Nb doping was very small and there was Pt deposition on the surface, the signal intensity of Nb in XPS was very low, so only the valence changes of Ti before and after the durability test were compared. As Fig. 3.10 shows that, Ti 2p XPS spectra were detected. The peaks can be separated into Ti^{4+} and Ti^{3+} according to the symmetrical peak shape. Since the support used in this experiment was mainly composed of Ti_4O_7, whether the titanium oxide is gradually oxidized during the durability test becomes the focus. If Ti_4O_7 is oxidized to titanium dioxide, the electrical conductivity will be greatly reduced, which will lead to a decrease of catalyst performance. Comparing the proportion of Ti^{3+} before and after ADT, they were 11.16% and 10.65%, respectively. It means that the calculated valence was 3.8884 and 3.8935, respectively. It could be found that the calculated valence is higher than Ti_4O_7 theoretical calculated value, which is 3.5. It was considered that the synthetic support was not Ti_4O_7 pure phase. Compared before and after the durability test, the proportion of Ti^{3+} did not decrease seriously, indicating that the titanium oxide carrier has good durability.

In order to inspect the differences in the electronic states of the Pt deposits in those catalysts before and after the electrochemical tests, as shown in Figs. 3.11 (a–h). Pt 4f XPS spectra were detected. The valence state ratios of Pt are shown in Figs. 3.12 (a and b). Pt was separated according to Pt0, Pt2+, and Pt^{4+}. From Figs. 3.11 (a–f), it can be observed that the peaks of 2, 5, and 10 wt%_Pt/Nb-doped Ti_4O_7 shifted to the lower binding energy direction by about 0.6 eV, [117] which was caused by the increase in electron density on Pt atoms caused by SMSI. [117] This is the same as other reports of Pt/TiO_x, demonstrating the existence of SMSI in Pt and Nb-doped Ti_4O_7. Fig. 3.12 (a) shows the proportion of Pt with different valences before electrochemical testing. The proportion of metallic Pt in 5 and 10 wt%_Pt/Nb-doped Ti_4O_7 was higher than that in 2 wt%_Pt/Nb-doped Ti_4O_7 and Pt/C, which was due to the electron donation of the Nb-doped Ti_4O_7 support to the deposited Pt. Meanwhile, fine Pt particle size (<2 nm) resulted in higher adsorption energies for oxygen-containing species. Therefore, the Pt nanoparticles (average: 1.4 nm) of 2 wt%_Pt/Nb-doped Ti_4O_7 were partially oxidized, resulting in a smaller proportion of metallic Pt. Figure 3.12 (b) shows the proportion of Pt with different valences after electrochemical testing. As the Pt size of 2 wt%_Pt/Nb-doped Ti_4O_7 increases,

the shape changes to an island-like shape, which causes the adsorption energy decreases. The Pt valence state composition in all Pt/Nb-doped Ti_4O_7 catalysts reached a similar number, demonstrating that the Pt valence state composition prepared by the APD method Pt/Nb-doped Ti_4O_7 has a higher ratio of metallic Pt, and the SMSI between Pt and Nb-doped Ti_4O_7 still exists after ADT.

Although fine Pt nanoparticles are beneficial to ECSA from an ECSA point of view, it decreases durability. From a stability point of view, Pt deposits with a thickness of about 4 nm are relatively stable, and island-like Pt deposits with a thickness of about 4 nm and abundant edges/corners enhance the ORR activity.

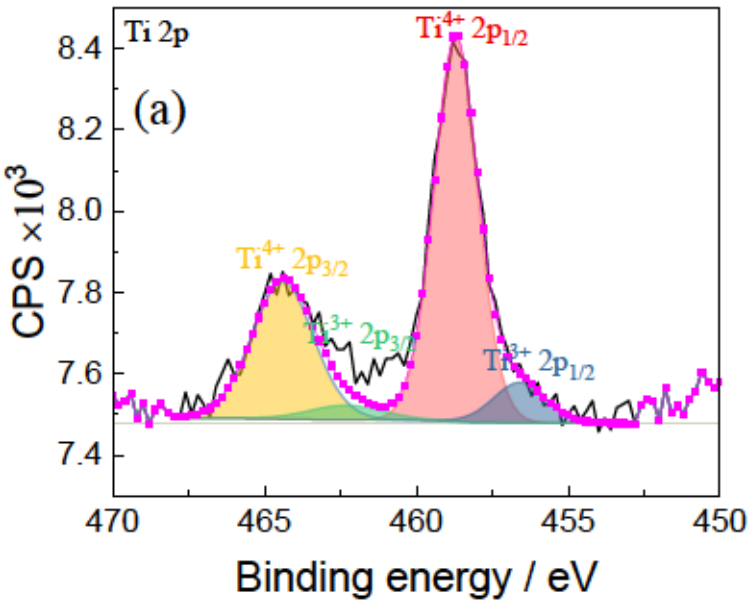

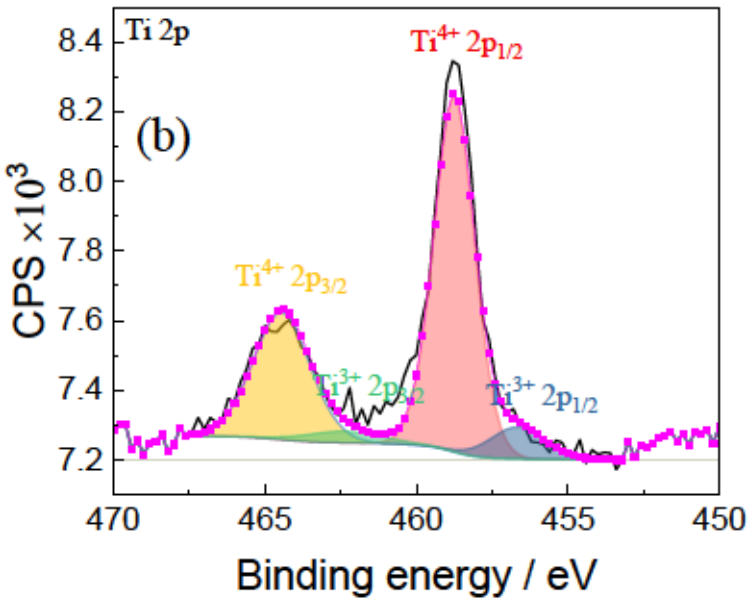

Fig. 3.10. Ti 2p XPS spectra of 5 wt% Pt/Nb-doped Ti_4O_7 before electrochemical test: (a) before ADT, (b) after ADT.

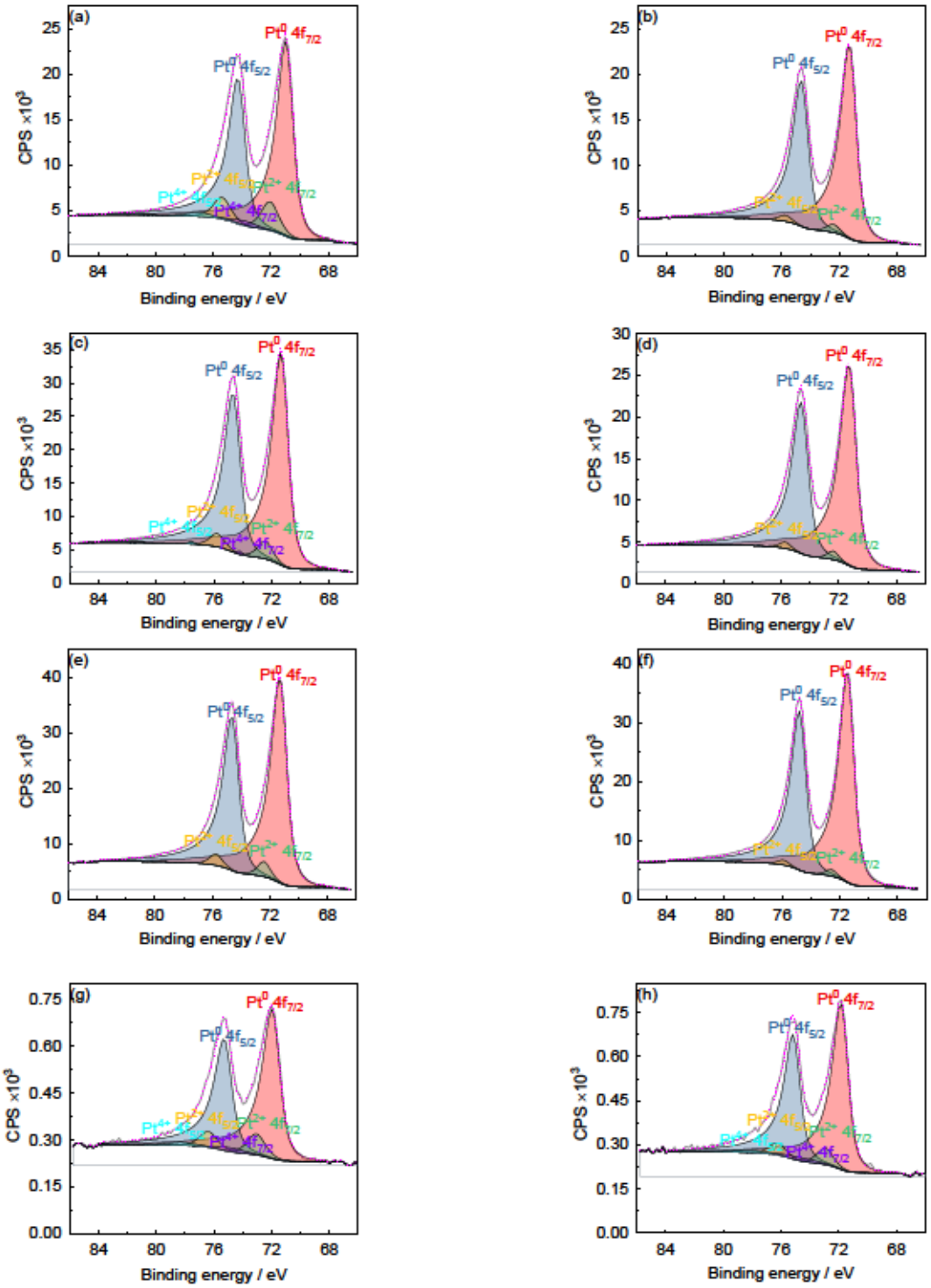

Fig. 3.11. Pt 4f XPS spectra of Pt/Nb-doped Ti_4O_7 before electrochemical test: (a) 2 wt%_Pt/Nb-doped Ti_4O_7, (b) 5 wt%_Pt/Nb-doped Ti_4O_7, (c) 10 wt%_Pt/Nb-doped Ti_4O_7, and (d) Pt/C; Pt 4f XPS spectra of Pt/Nb-doped Ti_4O_7 after electrochemical test: (e) 2 wt%_Pt/Nb-doped Ti_4O_7, (f) 5 wt%_Pt/Nb-doped Ti_4O_7, (g) 10 wt%_Pt/Nb-doped Ti_4O_7, and (h) Pt/C.

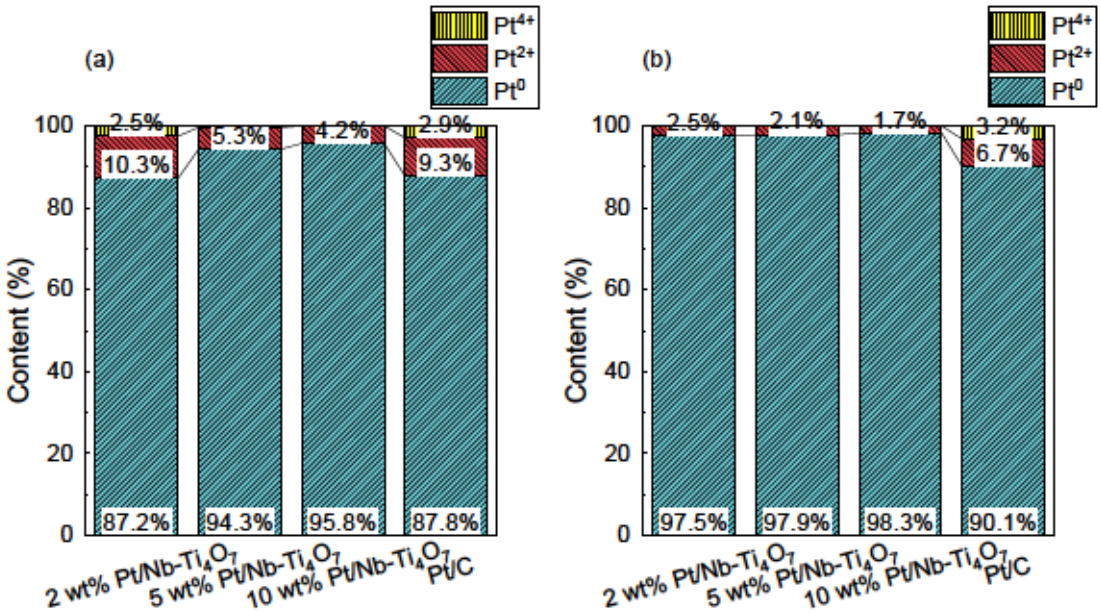

Fig. 3.12. (a) Percentages of different valences calculated by XPS before the electrochemical test; (b) percentages of different valences calculated by XPS after the electrochemical test.

3.4 Conclusion

As model Pt/titanium oxide catalysts, 2, 5, and 10 wt% Pt were deposited on macroporous Nb-doped Ti_4O_7 support by the APD method. The morphologies of 2, 5, and 10 wt% Pt/Nb-doped Ti_4O_7 were hemispherical, island-like, and film-like. The initial mean. sizes were approximately 1.4 nm, 2.4 nm, and 3.3 nm, respectively. After ADT, the shapes transformed to island-like, chain bead-like, and film-like, respectively. Due to its high affinity, when ADT of Pt/Nb-doped Ti_4O_7 catalyst was performed, platinum aggregated in the horizontal direction, but the increase in the vertical direction was small, which leaded to a small decrease in ECSA. It was considered that this is because the affinity between platinum and the titanium oxide was high. Moreover. 4 nm was considered as a stable thickness in APD prepared Pt/Nb-doped Ti_4O_7 catalyst.

Chapter 4

Summary

Fuel cells need to further improve the durability of catalysts as a next-generation clean energy technology. In this study, we investigated the physicochemical factors governing the surface area and conductivity of Nb-doped titanium oxide and the behavior of platinum on a Pt-supported Nb-doped Ti_4O_7 catalyst. In this work, the factors affecting the conductivity and specific surface area of Nb-doped titanium oxides support were discussed and the degradation characteristics of Pt/Nb–Ti_4O_7 were analysed.

In Nb-doped titanium oxide support, the nanoparticle Nb-doped TiO_2 and macroporous Nb-doped Ti_4O_7 support were synthesized by hydrothermal method. In this support, Nb dopant could improve the sintering resistance ability and conductivity with the dopant amount improved. On the other hand, hydrothermal synthesis with silica colloidal template, and done the heat treatment at high temperature could prepare the Nb-doped Ti_4O_7 with both high conductivity and specific surface area.

In Pt/ Nb-doped Ti_4O_7 catalyst, 4 nm was considered as a stable thickness. With the Pt amount increased the shape of Pt was also changed from hemisphere to film-like. 2 and 5 wt% Pt/Nb-Ti_4O_7 showed high durability and activity in ADT. It was considered that a high-performance carbon-free catalyst can be synthesized by depositing island-shaped platinum uniformly on titanium oxide at an appropriate density.

At last, it was considered that high durability Pt/titanium oxide based catalyst has positive significance for the popularization of PEFC devices such as FCV and I wish this research provided the primary data for high durable carbon-free Pt catalyst in PEFC.

Chapter 5

Outlook for social implementation

PEFC is an ideal power generation technology with zero-emission characteristics. Carbon-free catalysts can improve the durability of PEFCs and are helpful not only for hydrogen vehicles but also for distributed power generation. A low-cost, high-conductivity, high-specific surface area titanium oxide support manufacturing method that can be manufactured on a large scale and a method for supporting a highly active platinum-based catalyst could accelerate the spread of PEFC devices with high durability and high performance.

In the short term, with the adjustment of Honda's strategy for fuel cell vehicles, it was considered problematic to use hydrogen directly as a final consumer product to expand the market by relying on passenger cars gradually. In the new national development plan dominated by Japan, hydrogen is more inclined to link upstream renewable energy power generation and downstream markets as a fuel and a chemical feedstock. At present, almost all hydrogen production comes from primary energy, and green hydrogen production methods such as water electrolysis have a vast potential market.

As a medium-term goal, in the future, it could be imaged and expected that some extensive oil refining and chemical production enterprises will gradually strengthen hydrogen production to reduce the cost of hydrogen, and some countries and regions such as Japan will strengthen pipeline construction, like Europe, to further reduce the transportation cost of hydrogen through pipeline transportation. Meantime, as a new energy carrier, the hydrogen market trading system will also mature, which is not only simple manufacturing and sales but also includes technical trading, ocean transportation, futures trading, etc. with the spread of PEFC, carbon emissions from automobiles, and environmental pollution are expected to improve. With the large-scale use of hydrogen, we can expect the development of a new green energy business centered on the production, transportation, and sales of hydrogen. By realizing a hydrogen-implemented society, we will take a step toward a sustainable, environment-friendly society.

Here, we can boldly look forward to the future social vehicles will be dominated by electric vehicles and hydrogen fuel vehicles, of which passenger vehicles may be mainly electric vehicles, while commercial vehicles that require higher power, such as trucks, vans, mining vehicles, and forklifts, as well as trains on non-electrified lines will be dominated by hydrogen fuel. Cars will say goodbye to emissions and engine noise. All kinds of PEFC power generation equipment will also be popularized

with the popularization of intelligent grids, not only in Japan but all over the world. Primary energy such as oil and coal is no longer used as energy but continues to play its role in human production and life as an important chemical raw material. In the future, it is conceivable that, with the continuous development of science and technology, the city of the future may be similar to that in "Cyberpunk 2077". It completely replaces manual driving, and the car and the car, the car and the signal light, the car and the surrounding buildings can all interact with each other, thereby significantly reducing the accident rate. Civil aviation aircraft using PEFC as a power system will become the leading force in the future aviation industry. They would be fast and quiet, and passengers no longer have to put up with the engine's roar. The space shuttle that directly uses hydrogen as fuel will frequently travel between the earth and the moon and even between the earth and Mars. The footprint of humankind will be extended to more distant places with new energy methods. But unlike "Cyberpunk 2077", in the future, with the popularization of various zero-emission vehicles, the world will not be a wasteland but a highly modernized, sustainable, and environmentally friendly garden city.

References

[1] Original by Marx Karl, B. Fowkes trans. Das Kapital, Capital. New York: Knopf Doubleday, 1 (1977) 446.

[2] D. Enrique, The four drafts of Capital. Towards a new interpretation of the dialectical thought of Marx, Rethink. Marx., 13 (2001) 10–25.

[3] R. U. Ayres, Technological transformations and long waves. Part I. Technological forecasting and social change. 37 (1990) 1-37.

[4] H. W. Dickinson, A short history of the steam engine. Cambridge University Press, 2 (2011) 185-206.

[5] R. L. Hills, Power from steam: A history of the stationary steam engine. Cambridge University Press, 13 (1993) 258-281.

[6] C. Zou, Q. Zhao, G. Zhang, B. Xiong, Energy revolution: From a fossil energy era to a new energy era, Natural Gas Industry B, 3 (2016) 1-11.

[7] Second Industrial Revolution: The Technological Revolution. https://richmondvale.org/en/blog/second-industrial-revolution-the-technological-revolution (viewed on Aug 02 2022)

[8] BP. Statistical Review of World Energy 2021. https://www.bp.com/content/dam/bp/business-sites/en/global/corporate/pdfs/energy-economics/statistical-review/bp-stats-review-2021-full-report.pdf (viewed on Aug 02 2022)

[9] D. Jones. Global Electricity Review 2022. https://ember-climate.org/insights/research/global-electricity-review-2022/ (viewed on Aug 02 2022)

[10] Mauna Loa Observatory, Hawaii (Scripps UCSD). Scripps CO_2 Program. https://scrippsco2.ucsd.edu/ (viewed on Aug 02 2022)

[11] IPCC, 2014: Climate Change 2014: Synthesis Report. Contribution of Working Groups I, II and III to the Fifth Assessment Report of the Intergovernmental Panel on Climate Change IPCC, Geneva, Switzerland, 151 pp.

[12] R. Pielke, M. G. Burgess, J. Ritchie, Most plausible 2005-2040 emissions scenarios project less than 2.5 degrees C of warming by 2100, SocArXiv, 23 Mar. 2021. Web.

[13] NASA, Anticipating Future Sea Levels (2021), https://earthobservatory.nasa.gov/images/148494/anticipating-future-sea-levels (viewed on Aug 02 2022)

[14] EG&G Technical Services. Inc, Fuel Cell Handbook (Seventh Edition), 3 (2004) 16-19.

[15] EIA, INTERNATIONAL ENERGY OUTLOOK 2016 https://www.eia.gov/outlooks/ieo/pdf/0484(2016).pdf (viewed on Aug 02 2022)

[16] T. Kousksou, P. Bruel, A. Jamil, T. El Rhafiki, Y. Zeraouli, Energy storage: applications and challenges, Sol. Energy Mater Sol. Cells, 120 (2014) 59-80.

[17] Xinhua News, China's first salt cavern compressed air energy storage starts operation (2022). https://english.news.cn/20220527/87bea9710d1343ceb5f641087805d2ac/c.html (viewed on Aug 02 2022)

[18] S. Zachary. Largest pumped-hydro facility in world turns on in china. 2022. https://cleantechnica.com/2022/01/04/largest-pumped-hydro-facility-in-world-turns-on-in-china (viewed on Aug 02 2022)

[19] J. L. William, Hydrogen. https://www.britannica.com/science/hydrogen (viewed on Aug 02 2022)

[20] M. R. Hoffmann, Döbereiner's Lighter, American scientist 86 (1998) 326-329.

[21] J. Emsley, Nature's Building Blocks. Oxford: Oxford University Press. 2 (2001) 183–191.

[22] B. I. Tsenter, V.M. Sergeev, A.I. Kloss, Hermetically sealed nickel-hydrogen storage cell, US Patent 3669744.

[23] H. Y. Sohn, Y. Mohassab, Development of a novel flash ironmaking technology with greatly reduced energy consumption and CO_2 emissions, J. Sustain. Metall., 2 (2016) 216-227.

[24] H. Y. Sohn, D.–Q. Fan, A. Abdelghany, Design of novel flash ironmaking reactors for greatly reduced energy consumption and CO_2 emissions, Metals, 11 (2021) 332.

[25] M. Carcassi, F. Fineschi, Deflagrations of H_2–air and CH_4–air lean mixtures in a vented multi-compartment environment, Energy 30(8) (2005) 1439-1451.

[26] P. Jens, M. Unteutsch, and A. Loevenich, The future cost of electricity-based synthetic fuels, 6 (2018), 60-64.

[27] F. G. Albrecht, D. H. König, N. Baucks, R. Dietrich, A standardized methodology for the techno-economic evaluation of alternative fuels – A case study, Fuel, 194 (2017) 511–526

[28] Element Energy Ltd, Hydrogen supply chain evidence base - Prepared for the UK Department for Business, Energy & Industrial Strategy, https://assets.publishing.service.gov.uk/government/uploads/system/uploads/attachment_data/file/760479/H2_supply_chain_evidence_-_publication_version.pdf (viewed on Aug 02 2022)

[29] N. Muradov, Low to near-zero CO_2 production of hydrogen from fossil fuels: Status and perspectives, Int. J. Hydrog. Energy, 42(20) (2017) 14058-14088.

[30] The government of Japan, Creating a "Hydrogen Society" to Protect the Global Environment, (2017). https://www.japan.go.jp/tomodachi/2017/spring-summer2017/creating_a_hydrogen_society.html (viewed on Aug 02 2022)

[31] The gas turbine industry commitments to drive Europe's transition to a decarbonized energy mix" (press release), 23 January 2019, https://powertheeu.eu/wp-content/themes/euturbines/dl/EUTurbines-press-release-on-the-Commitments.pdf (viewed on Aug 02 2022)

[32] M. Cifrain, K. Kordesch, W. Vielstich, A. Lamm, H. A. Gasteiger, Hydrogen/oxygen (air) fuel cells with alkaline electrolytes, Handbook of fuel cells–fundamentals, Technology and Applications, 1 (2003) 267-280.

[33] L. Lhotseng, Fuel Cell Thermodynamics, IntechOpen, (2019) 8-9.

[34] A. T. Haug, R. E. White, J. W. Weidner, W. Huang, S. Shi, T. Stoner, N. Rana, Increasing proton exchange membrane fuel cell catalyst effectiveness through sputter deposition, J. Electrochem. Soc., 149 (2002) A280.

[35] K.–L. Huang, Y.–C. Lai, C.–H. Tsai, Effects of sputtering parameters on the performance of electrodes fabricated for proton exchange membrane fuel cells, J. Power Sources., 156 (2006) 224-231.

[36] S. Mukerjee, S. Srinivasan, A. J. Appleby, Effect of sputtered film of platinum on low platinum loading electrodes on electrode kinetics of oxygen reduction in proton exchange membrane fuel cells, Electrochim. Acta, 38 (1993) 1661-1669.

[37] A. Esmaeilifar, S. Rowshanzamir, M. Eikani, E. Ghazanfari, Synthesis methods of low-Pt-loading electrocatalysts for proton exchange membrane fuel cell systems, Energy 35(9) (2010) 3941-3957.

[38] T. R. Ralph, Catalysis for low temperature fuel cells, Platin. Met. Rev., 46 (2012) 146-164

[39] E. Antolini, J. Salgado, L. Santos, G. Garcia, E. Ticianelli, E. Pastor, E. Gonzalez, Carbon supported Pt–Cr alloys as oxygen-reduction catalysts for direct methanol fuel cells, J. Appl. Electrochem., 36(3) (2006) 355-362.

[40] B. Chen, Research and development of fuel cell technology in China, Asia-Pacific Power and Energy Engineering Conference. IEEE., (2011) 1-4.

[41] F. Zhao, Z. Mu, H. Hao, Z. Liu, hydrogen fuel cell vehicle development in china: an industry chain perspective, Energy Technol., 8 (2020) 2000179.

[42] Specifications of Volvo S60. https://www.volvocars.com/us/compare-specs/s60 (viewed on Aug 02 2022)

[43] Specifications of Telsa Model 3. https://www.tesla.com/model3/design (viewed on Aug 02 2022)

[44] Specifications of Toyota Mirai. https://toyota.jp/mirai/ (viewed on Aug 02 2022)

[45] L. Roen, C. Paik, T. Jarvi, Electrocatalytic corrosion of carbon support in PEMFC cathodes, Electrochem. Solid State Lett., 7 (2003) A19-A22.

[46] N. Macauley, D. D. Papadias, J. Fairweather, D. Spernjak, D. Langlois, R. Ahluwalia, K. L. More, R. Mukundan, R. L. Borup, Carbon corrosion in pem fuel cells and the development of accelerated stress tests, J. Electrochem. Soc., 165 (2018) F3148-F3160.

[47] New Energy and Industrial Technology Development Organization. Technology Development Roadmap (FCV/Mobile), (2017). https://www.nedo.go.jp/content/100944012.pdf (viewed on Aug 02 2022)

[48] F. R. Rodriguez, The role of carbon materials in heterogeneous catalysis, Carbon, 36 (1998) 159-175.

[49] X. Wang, W. Li, Z. Chen, M. Waje, Y. Yan, Durability investigation of carbon nanotube as catalyst support for proton exchange membrane fuel cell, J. Power Sources, 158 (2006) 154-159.

[50] S. Mukerjee, S. Srinivasan, Enhanced electrocatalysis of oxygen reduction on platinum alloys in proton exchange membrane fuel cells, J. Electroanal. Chem., 357 (1993) 201-224.

[51] P. Yu, M. Pemberton, P. Plasse, PtCo/C cathode catalyst for improved durability in PEMFCs, J. Power Sources, 144 (2005) 11-20.

[52] B. C. Prado, S. A. Linares, R. F. Rodriguez, C. S. M. D. Lecea, Effect of carbon support and mean Pt particle size on hydrogen chemisorption by carbon-supported Pt ctalysts, J. Catal., 128 (1991) 397-404.

[53] Z. Zhang, J. Liu, J. Gu, L. Sub, L. Cheng, An overview of metal oxide materials as electrocatalysts and supports for polymer electrolyte fuel cells, Energy Environ. Sci., 7 (2014) 2535-2558.

[54] L. Du, Y. Shao, J. Sun, G. Yin, J. Liu, Y. Wang, Advanced catalyst supports for PEM fuel cell cathodes, Nano Energy, 29 (2016) 314-322.

[55] F. Ando, T. Tanabe, T. Gunji, T. Tsuda, S. Kaneko, T. Takeda, T. Ohsaka, F. Matsumoto, Improvement of ORR activity and durability of pt electrocatalyst nanoparticles anchored on TiO_2/cup-stacked carbon nanotube in acidic aqueous media, Electrochim. Acta, 232 (2017) 404-413.

[56] I. A. Pašti, N. M. Gavrilov, S. V. Mentus, Electrocatalytic behavior of Pt/WO_3 composite layers formed potentiodynamically on tungsten surfaces, Int. J. Electrochem. Sci., 12 (2017) 5772-5791.

[57] K. Kakinuma, M. Hayashi, T. Hashimoto, A. Iiyama, M. Uchida, Enhancement of the catalytic activity and load cycle durability of a PtCo alloy cathode catalyst supported on Ta-doped SnO_2 with a unique fused aggregated network microstructure for polymer electrolyte fuel cells, ACS Appl. Energy Mater., 3 (2020) 6922-6928.

[58] F. Xu, D. Wang, B. Sa, Y. Yu, S. Mu, One-pot synthesis of Pt/CeO_2/C catalyst for improving the ORR activity and durability of PEMFC, Int. J. Hydrogen Energy, 42 (2017) 13011-13019.

[59] J. Wang, B. Wang, Z. Wang, L. Chen, C. Gao, B. Xu, Z. Jia, G. Wu, Synthesis of 3D flower-like ZnO/$ZnCo_2O_4$ composites with the heterogeneous interface for excellent electromagnetic wave absorption properties, J. Colloid Interf. Sci., 586 (2021) 479-490.

[60] Z. Gao, Z. Jia, K. Wang, X. Liu, L. Bi, G. Wu, Simultaneous enhancement of recoverable energy density and efficiency of lead-free relaxor-ferroelectric BNT-based ceramics, Chem. Eng. J., 402 (2020) 125951,

[61] P. F. B. D. Martin, E. A. Ticianelli, Electrocatalytic activity and stability of platinum nanoparticles supported on carbon–molybdenum oxides for the oxygen reduction reaction, ChemElectroChem, 2 (2015) 1298-1306.

[62] G. Wang, K. Bhattacharyya, J. Parrondo, V. Ramani, X-ray photoelectron spectroscopy study of the degradation of Pt/ITO electrocatalyst in an operating polymer electrolyte fuel cell, Chem. Eng. Sci., 154 (2016) 81-89.

[63] T. Ioroi, Z. Siroma, S. Yamazaki, K. Yasuda, Electrocatalysts for PEM fuel cells, Adv. Energy Mater., 9 (2019) 1801284.

[64] E. Fabbri, A. Rabis, Y. Chino, M. Uchida, T. J. Schmidt, Boosting Pt oxygen reduction reaction activity by tuning the tin oxide support, Electrochem. Commun., 83 (2017) 90-95.

[65] G. Cognard, G. Ozouf, C. Beauger, L. Dubau, M. H. López, M. Chatenet, F. Maillard, Insights into the stability of Pt nanoparticles supported on antimony-doped tin oxide in different potential ranges, Electrochim. Acta, 245 (2017) 993-1004.

[66] I. M. Jiménez, F. Haidar, S. Cavaliere, D. Jones, J. Rozière, Strong interaction between platinum nanoparticles and tantalum-doped tin oxide nanofibers and its activation and stabilization effects for oxygen reduction reaction, ACS Catal., 10 (2020) 10399-10411.

[67] T. Arai, O. Takashi, K. Amemiya, T. Takahashi, Study of oxide supports for PEFC catalyst, SAE Int. J. Altern. Powertrains, 6 (2017) 145-150.

[68] Y. Kuroda, H. Igarashi, T. Nagai, T.W. Napporn, K. Matsuzawa, S. Mitsushima, K.-i. Ota, A. Ishihara, Templated Synthesis of Carbon-free mesoporous Magnéli-phase titanium suboxide, electrocatalysis, 10 (2019) 459-465.

[69] J. Smith, F. Walsh, R. Clarke, Electrodes based on Magnéli phase titanium oxides: the properties and applications of Ebonex® materials, J. Appl. Electrochem., 28 (1998) 1021-1033.

[70] S. Tominaka, Y. Tsujimoto, Y. Matsushita, K. Yamaura, Synthesis of Nanostructured Reduced Titanium Oxide: Crystal Structure Transformation Maintaining Nanomorphology, Angew. Chem.,

[71] A. Gusev, E. Avvakumov, O. Vinokurova, Synthesis of Ti_4O_7 Magneli phase using mechanical activation, Sci. Sinter., 35(3) (2003) 141-145.

[72] D. Kundu, R. Black, E.J. Berg, L.F. Nazar, A highly active nanostructured metallic oxide cathode for aprotic LiO_2 batteries, Energy Environ. Sci., 8 (2015) 1292-1298.

[73] Y. Ma, T. Nagai, Y. Inoue, K. Ikegami, Y. Kuroda, K. Matsuzawa, T.W. Napporn, Y. Liu, S. Mitsushima, A. Ishihara, Control of surface area and conductivity of niobium-added titanium oxides as durable supports for cathode of polymer electrolyte fuel cells, Mater. Des., 203 (2021) 109623.

[74] V. Kumaravel, S. Mathew, J. Bartlett, S. C. Pillai, Photocatalytic hydrogen production using metal doped TiO_2: A review of recent advances, Appl. Catal. B Environ., 244 (2019) 1021-1064.

[75] N. Rahimi, R. A. Pax, E. M. Gray, Review of functional titanium oxides. I: TiO_2 and its modifications, Prog. Solid. State Ch., 44 (2016) 86-105.

[76] J. Cai, J. Shen, X. Zhang, Y. H. Ng, J. Huang, W. Guo, C. Lin, Y. Lai, Light-driven sustainable hydrogen production utilizing TiO_2 nanostructures: A Review, Small Methods, 3 (2019) 1800184.

[77] S. B. Patil, P. S. Basavarajappa, N. Ganganagappa, M. S. Jyothi, A. V. Raghu, K. R. Reddy, Recent advances in non-metals-doped TiO_2 nanostructured photocatalysts for visible-light driven hydrogen production, CO_2 reduction and air purification, Int. J. Hydrogen Energy, 44 (2019)

[78] Z. Niu, F. Gao, X. Jia, W. Zhang, W. Chen, K. Qian, Synthesis studies of sputtering TiO_2 films on poly (dimethylsiloxane) for surface modification, Colloids Surf. A Physicochem. Eng. Asp., 272 (2006) 170-175.

[79] J. F. Baumard, E. Tani, Electrical conductivity and charge compensation in Nb doped TiO_2 rutile, J. Chem. Phys., 67 (1977) 857-860.

[80] J. Arbiol, J. Cerda, G. Dezanneau, A. Cirera, F. Peiro, A. Cornet, J. R. Morante, Effects of Nb doping on the TiO_2 anatase-to-rutile phase transition, J. Appl. Phys., 92 (2002) 853-861.

[81] Y. Liu, J. M. Szeifert, J. M. Feckl, B. Mandlmeier, J. Rathousky, O. Hayden, D. Fattakhova-Rohlfing, T. Bein, Niobium-doped titania nanoparticles: synthesis and assembly into mesoporous films and electrical conductivity, ACS Nano, 4 (2010) 5373-5381.

[82] S. K. Mukherjee, H. W. Becker, A. P. Cadiz Bedini, A. Nebatti, C. Notthoff, D. Rogalla, S. Schipporeit, A. E. Soleimani, D. Mergel, Structural and electrical properties of Nb-doped TiO_2 films sputtered with plasma emission control, Thin Solid Films, 568 (2014) 94-101.

[83] M. J. Kim, C. R. Kwon, K. S. Eom, J. H. Kim, E. A. Cho, Electrospun Nb-doped TiO_2 nanofiber support for Pt nanoparticles with high electrocatalytic activity and durability, Sci. Rep., 7 (2017) 44411.

[84] C. He, S. Sankarasubramanian, I. Matanovic, P. Atanassov, V. Ramani, Understanding the oxygen reduction reaction activity and oxidative stability of Pt supported on Nb-Doped TiO_2, ChemSusChem, 12 (2019) 3468-3480.

[85] Y. Senoo, K. Taniguchi, K. Kakinuma, M. Uchida, H. Uchida, S. Deki, M. Watanabe, Cathodic performance and high potential durability of Ta-$SnO_{2-\delta}$-supported Pt catalysts for PEFC cathodes, Electrochem. Commun., 51 (2015) 37-40.

[86] X. Lü, X. Mou, J. Wu, D. Zhang, L. Zhang, F. Huang, F. Xu, S. Huang, Improved-performance Dye-Sensitized solar cells using Nb-doped TiO_2 electrodes: efficient electron injection and transfer, Adv. Funct. Mater., 20 (2010) 509-515.

[87] K. M. Choi, K. Kuroda, Double function of tris (hydroxymethyl) aminomethane (THAM) for the preparation of colloidal silica nanospheres and the conversion to ordered mesoporous carbon, ChemComm, 47(39) (2011) 10933-10935.

88] Y. Kuroda, K. Kuroda, Morphosynthesis of nanostructured gold crystals by utilizing interstices in periodically arranged silica nanoparticles as a flexible reaction field, Angew. Chem., 122 (2010) 7147-7151.

[789] A. Ohma, K. Shinohara, A. Iiyama, T. Yoshida, A. Daimaru, Membrane and catalyst performance targets for automotive fuel cells by FCCJ membrane, catalyst, MEA WG, ECS Trans., 41 (2011) 775-784.

[90] R. D. Shannon, Revised effective ionic radii and systematic studies of interatomic distances in halides and chalcogenides. Acta Cryst., A32 (1976) 751-767.

[91] D. A. H. Hanaor, C.C. Sorrell, Review of the anatase to rutile phase transformation, J. Mater. Sci., 46 (2011) 855-874.

[92] A. M. Ruiz, G. Dezanneau, J. Arbiol, A. Cornet, J. R. Morante, Insights into the structural and chemical modifications of Nb additive on TiO_2 nanoparticles, Chem. Mater., 16 (2004) 862-871.

[93] R. M. Pittman, A. T. Bell, Raman studies of the structure of Nb_2O_5/TiO_2, J. Phys. Chem., 97 (1993) 12178-12185.

[94] R. K. Sharma, M. C. Bhatnagar, Improvement of the oxygen gas sensitivity in doped TiO thick films, Sens. Actuators B, 56 (1999) 215-219.

[95] C. Zhang, M. Ikeda, T. Uchikoshi, J.-G. Li, T. Watanabe, T. Ishigaki, High-concentration niobium (V) doping into TiO_2 nanoparticles synthesized by thermal plasma processing, J. Mater. Res., 26 (2011) 658-671.

[96] L. Sheppard, T. Bak, J. Nowotny, C.C. Sorrell, S. Kumar, A. R. Gerson, M. C. Barnes, C. Ball, Effect of niobium on the structure of titanium dioxide thin films, Thin Solid Films, 510 (2006) 119-124.

[97] A. Ishihara, M. Arao, M. Matsumoto, T. Tokai, T. Nagai, Y. Kuroda, K. Matsuzawa, H. Imai, S. Mitsushima, K. Ota, Niobium-doped titanium oxides powders as non-noble metal cathodes for polymer electrolyte fuel cells–Electrochemical evaluation and effect of doped amount of niobium, Int. J. Hydrog. Energy, 45 (2020) 5438-5448.

[98] S. Hussain, H. Erikson, N. Kongi, A. Tarre, P. Ritslaid, A. Kikas, V. Kisand, J. Kozlova, J. Aarik, A. Tamm, Platinum sputtered on Nb-doped TiO_2 films prepared by ALD: highly active and durable carbon-free ORR electrocatalyst, J. Electrochem. Soc., 167 (2020) 164505.

[99] M. Marezio, P. Dernier, The crystal structure of Ti_4O_7, a member of the homologous series Ti_nO_{2n-1}, J. Solid State Chem., 3 (1971) 340-348.

[100] N. Yamada, T. Hitosugi, N. L. H. Hoang, Y. Furubayashi, Y. Hirose, T. Shimada, T. Hasegawa, Fabrication of low resistivity Nb-doped TiO_2 transparent conductive polycrystalline films on glass by reactive sputtering, J. Appl. Phys., 46 (2007) 5275.

[101] D. Takimoto, Y. Toda, S. Tominaka, D. Mochizuki, W. Sugimoto, Conductive nanosized Magneli-phase Ti_4O_7 with a core@ shell structure, Inorg. Chem., 58 (2019) 7062-7068.

[102] A. Ishihara, J. Hirata, T. Nagai, Y. Kuroda, K. Matsuzawa, A. Imanishi, S. Mitsushima, Y. Takasu, K. Ota, Effect of semiconducting properties of oxide-based compounds on oxygen reduction activity in acidic media, ECS trans., 98 (2020) 457-464.

[103] J. Bisquert, F. S. Fabregat, I. S. Mora, G. B. Garcia, E. M. Barea, E. Palomares, A review of recent results on electrochemical determibation of the density of electronic states of nanostructures metal-oxide semiconductors and organic hole conductors, Inorganica Chim. Acta, 361 (2008) 684-698.

[104] K. Kakinuma, K. Suda, R. Kobayashi, T. Tano, C. Arata, I. Amemiya, S. Watanabe, M. Matsumoto, H. Imai, A. Iiyama, M. Uchida, Electronic states and transport phenomena of Pt nanoparticle catalysts Supported on Nb-Doped SnO_2 for polymer electrolyte fuel cells, ACS Appl. Mater. Interfaces, 11 (2019) 34957-34963.

[105] M. Kitahara, Y. Shimasaki, T. Matsuno, Y. Kuroda, A. Shimojima, H. Wada, K. Kuroda, The critical effect of niobium doping on the formation of mesostructured TiO_2: single-crystalline ordered mesoporous Nb-TiO_2 and plate-like Nb-TiO_2 with ordered mesoscale dimples, Chem. Eur. J., 21 (2015) 13073-13079.

[106] Q. Jia, S. Ghoshal, J. Li, W. Liang, G. Meng, H. Che, S. Zhang, Z.-F. Ma, S. Mukerjee, Metal and metal oxide interactions and their catalytic consequences for oxygen reduction reaction, J. Am. Chem. Soc., 139(23) (2017) 7893-7903.

[107] T. Ioroi, H. Senoh, S. Yamazaki, Z. Siroma, N. Fujiwara, K. Yasuda, Stability of corrosion-resistant Magnéli-phase Ti_4O_7-supported PEMFC catalysts at high potentials, J. Electrochem. Soc., 155 (2008) B321.

[108] M. C. Tsai, T. T. Nguyen, N. G. Akalework, C. J. Pan, J. Rick, Y. F. Liao, W. N. Su, B. J. Hwang, Interplay between molybdenum dopant and oxygen vacancies in a TiO_2 support enhances the oxygen reduction reaction, ACS catalysis, 6 (2016) 6551-6559.

[109] A. D. Duma, Y. C. Wu, W. N. Su, C. J. Pan, M. C. Tsai, H. M. Chen, J. F. Lee, H. S. Sheu, V. T. T. Ho, B. J. Hwang, In situ confined synthesis of Ti_4O_7 supported platinum electrocatalysts with enhanced activity and stability for the oxygen reduction reaction, ChemCatChem, 10(5) (2018) 1155-1165.

[110] V. T. T. Ho, C.–J. Pan, J. Rick, W.–N. Su, B.–J. Hwang, Nanostructured Ti0.7Mo0.3O2 support enhances electron transfer to Pt: high-performance catalyst for oxygen reduction reaction, J. Am. Chem. Soc., 133 (2011) 11716-11724.

[111] T.–B. Do, M. Cai, M. S. Ruthkosky, T. E. Moylan, Niobium-doped titanium oxide for fuel cell application, Electrochim. Acta, 55 (2010) 8013-8017.

[112] S. Sun, G. Zhang, X. Sun, M. Cai, M. Ruthkosky, Highly stable and active Pt/Nb-TiO_2 carbon-free electrocatalyst for proton exchange membrane fuel cells, J. Nanotechnol., 2012 (2012) 389505.

[113] N. R. Elezović, B. M. Babić, L. K. Gajić, V. Radmilović, N.V. Krstajić, L. Vračar, Synthesis,

characterization and electrocatalytical behavior of Nb–TiO_2/Pt nanocatalyst for oxygen reduction reaction, J. Power Sources, 195 (2010) 3961-3968.

[114] B. J. Hsieh, M.–C. Tsai, C.–J. Pan, W.–N. Su, J. Rick, J.–F. Lee, Y.–W. Yang, B.-J. Hwang, Platinum loaded on dual-doped TiO_2 as an active and durable oxygen reduction reaction catalyst, NPG Asia Mater., 9(7) (2017) e403.

[115] Y. Agawa, M. Kunimatsu, T. Ito, Y. Kuwahara, H. Yamashita, ECS Electrochem. Lett., 4, F57 (2015).

[116] N. Todoroki, T. Kato, T. Hayashi, S. Takahashi, T. Wadayama, Pt–Ni nanoparticle-stacking thin film: highly active electrocatalysts for oxygen reduction reaction, Acs Catal., 5(4) (2015) 2209-2212.

[117] C. Xu, J. Yang, E. Liu, Q. Jia, G.M. Veith, G. Nair, S. DiPietro, K. Sun, J. Chen, P. Pietrasz, Physical vapor deposition process for engineering Pt based oxygen reduction reaction catalysts on NbOx templated carbon support, J. Power Sources, 451 (2020) 227709.

[118] Z.–Z. Jiang, Z.–B. Wang, Y.–Y. Chu, D.–M. Gu, G.–P. Yin, Ultrahigh stable carbon riveted Pt/TiO_2–C catalyst prepared by in situ carbonized glucose for proton exchange membrane fuel cell, Energy Environ. Sci., 4 (2011) 728-735.

[119] A. Dauscher, L. Hilaire, F. L. Normand, W. Müller, G. Maire, A. Vasquez, Characterization by XPS and XAS of supported Pt/TiO_2 CeO_2 catalysts, Surf. Interf. Anal., 16(1-12) (1990) 341-346.

[120] A. Arico, A. K. Shukla, H. Kim, S. Park, M. Min, V. Antonucci, Appl. Surf. Sci 172 (2001) 33.

[121] T. Huizinga, H. V. T. Blik, J. Vis, R. Prins, XPS investigations of Pt and Rh supported on γ-Al_2O_3 and TiO_2, Surf. Sci., 135(1-3) (1983) 580-596.

[122] E. I. Vovk, A. V. Kalinkin, M. Y. Smirnov, I. O. Klembovskii, V. I. Bukhtiyarov, XPS study of stability and reactivity of oxidized Pt nanoparticles supported on TiO_2, J. Phys. Chem. C, 121 (2017) 17297-17304.

[123] S. Y. Moon, B. Naik, C.–H. Jung, K. Qadir, J. Y. Park, Tailoring metal–oxide interfaces of oxide-encapsulated Pt/silica hybrid nanocatalysts with enhanced thermal stability, Catal. Today, 265 (2016) 245-253.

[124] K. Qadir, S. H. Kim, S. M. Kim, H. Ha, J. Y. Park, Support effect of arc plasma deposited Pt nanoparticles/TiO_2 substrate on catalytic activity of CO oxidation, J. Phys. Chem. C, 116 (2012) 24054-24059.

[125] K. Banno, M. Mizuno, K. Fujita, T. Kubo, M. Miyoshi, T. Egawa, T. Soga, Transfer-free graphene synthesis on insulating substrates via agglomeration phenomena of catalytic nickel films, Appl. Phys. Lett., 103 (2013) 082112.

[126] T. Sheng, N. Tian, Z.–Y. Zhou, W.–F. Lin, S.–G. Sun, Designing Pt-based electrocatalysts with high surface energy, ACS Energy Lett., 2 (2017) 1892-1900.

[127] E. Valenzuela, V. S. Ramos, A. A. A. Lambert, O. Savadogo, Nanostructured TiO_2 doped with Nb as a novel support for PEMFC, J. Mater., 2013 (2013) 706513.

[128] D. Malevich, V. Drozdovich, I. Zharskii, Research of hydrogen spillover on Pt/Ti and (Pt-TiO_2)/Ti electrocatalysts, Studies in Surface Science and Catalysis, Elsevier, (1997), 359-366.

[129] Z.–W. Wei, H.–J. Wang, C. Zhang, K. Xu, X.–L. Lu, T.–B. Lu, Reversed charge transfer and enhanced hydrogen spillover in platinum nanoclusters anchored on titanium oxide with rich oxygen vacancies boost hydrogen evolution reaction, Angew. Chem., 133 (2021) 16758-16763.

[130] R. A. Armengol, J. Lim, M. Ledendecker, K. Hengge, C. Scheu, Correlation between the TiO_2 encapsulation layer on Pt and its electrochemical behavior, Nanoscale Advances, 3 (2021) 5075-5082.

[131] K. Miyazawa, T. Nagai, K. Kimoto, M. Yoshitake, Y. Tanaka, HRTEM-EELS cross-sectional structural analyses of glassy carbon substrate irradiated by platinum ions using a coaxial arc plasma gun, Surf. Interf. Anal., 52 (2020) 23-33.

[132] A. E. Sleightholme, A. Kucernak, An anomalous peak observed in the electrochemistry of the platinum/perfluorosulfonic acid membrane interface, Electrochimi., acta 56 (2011) 4396-4402.

[133] N. M. Marković, R. R. Adžić, B. Cahan, E. Yeager, Structural effects in electrocatalysis: oxygen reduction on platinum low index single-crystal surfaces in perchloric acid solutions, J. Electroanal. Chem., 377 (1994) 249-259.

[134] V. Komanicky, K. Chang, A. Menzel, N. Markovic, H. You, X. Wang, D. Myers, Stability and dissolution of platinum surfaces in perchloric acid, J. Electroanal. Chem., 153 (2006) B446.

[135] M. Inaba, A. Zana, J. Quinson, F. Bizzotto, C. Dosche, A. Dworzak, M. Oezaslan, S.B. Simonsen, L.T. Kuhn, M. Arenz, The oxygen reduction reaction on Pt: why particle size and interparticle distance matter, ACS Catal., 11 (2021) 7144-7153.

[136] B. E. Hayden, D. Pletcher, J. P. Suchsland, L. J. Williams, The influence of support and particle size on the platinum catalysed oxygen reduction reaction, Phys. Chem. Chem. Phys., 11 (2009)

9141-9148.

[137] N. Tian, Z.–Y. Zhou, S.–G. Sun, Platinum metal catalysts of high-index surfaces: from single-crystal planes to electrochemically shape-controlled nanoparticles, J. Phys. Chem. C, 112 (2008) 19801-19817.

[138] P. G. D. Gennes, Wetting: statics and dynamics, Rev. Mod. Phys., 57 (1985) 827.

[139] W. Nie, Q. Zhu, Y. Gao, Z. Wang, Y. Liu, X. Wang, R. Chen, F. Fan, C. Li, Visualizing the spatial heterogeneity of electron transfer on a metallic nanoplate prism, Nano Lett., 21 (2021) 8901-8909.

[140] Q. Du, J. Wu, H. Yang, Pt@ Nb-TiO_2 catalyst membranes fabricated by electrospinning and atomic layer deposition, ACS Catal., 4 (2014) 144-151.

Chapter 6

Acknowledgments

Since 2016, I have been studying in Japan for six years. Thanks to Prof. Mitsushima for his help and guidance over the past six years. Thanks to the strict requirements of Prof. Mitsushima, I can learn a lot of knowledge and change my life.

I was also wondering to thank the scholarship provider Japan chemical industry association (JCIA). The JCIA scholarship helped me study and live in Japan smoothly for three years. Also, I was wondering to thank the grant from the power energy professional training program (PEP).

Thanks to Prof. Ishihara for guiding me. Under the guidance and help of Prof. Ishihara, I successfully carried out the research related to oxide carriers and learned the related knowledge of electrochemistry and metal oxides. Meantime, I was wondering to thank Prof. Ishihara for his valuable comments and suggestions on living and studying in Japan.

Also, I was wondering to thank Prof. Kuroda for his guidance on physical property analysis. I was wondering to thank Prof. Matsuzawa, who gave me lots of advice on living in Japan when I first came to Japan. Also, in the electrochemical test, I was wondering to thank Dr. Nagai, who helped me a lot in the electrochemical test. Meanwhile, I was wondering to thank Dr. Teko W. Napporn. He is a kind man who gave many valuable opinions on electrochemical analysis testing and XPS analysis, which are very helpful to my study and research. Further, I would like to thank all students in our lab, specifically Mr. Igarashi, who was my tutor and helped me a lot when I came to Japan.

Thanks to my mother for her understanding and support. The support from my family is undoubtedly the most prominent pillar of my perseverance. Thank you to my friends, both in Japan and in other countries or regions. Your help is my hope and reliance in the slump of life.

Thanks to all the mentors and friends who warned me when I was successful and encouraged me when I failed.

六年寒窗，有收获，有遗憾，有汗水，有笑容。愿这人生中的难得的宝贵经历，指导并激励我不断向前。不忘初心，砥砺前行。

Chapter 7

Appendix

7.1 Publications and Presentation

Publications:

1. Y. Ma, T. Nagai, Y. Inoue, K. Ikegami, Y. Kuroda, K. Matsuzawa, T.W. Napporn, Y. Liu, S. Mitsushima, A. Ishihara, Control of surface area and conductivity of niobium-added titanium oxides as durable supports for cathode of polymer electrolyte fuel cells, Materials & Design 203 (2021) 109623.
2. Y. Ma, H. Kajima, Y. Shimasaki, T. Nagai, T. Napporn, H. Wada, K. Kuroda, Y. Kuroda, A. Ishihara, S. Mitsushima, Degradation analysis of Pt/Nb–Ti_4O_7 as PEFC cathode catalysts with controlled arc plasma–deposited platinum content, Electrochemistry, 90 2022 057004.
3. Y. Ma, Y. Cheng, Y. Inoue, T. Nagai, Y. Kuroda, K. Matsuzawa, S. Mitsushima, Y. Liu, Y. Wang, A. Ishihara, Titanium oxide nano-particles as supports of cathode catalysts for polymer electrolyte fuel cells, ECS Trans, 92 2019 485.
4. Y. Inoue, K. Matsuzawa, Y. Ma, Y. Ohgi, T. Nagai, Y. Kuroda, S. Yamamoto, A. Ishihara, P-doped SnO_2 powder as a support for PEFC cathode, ECS Transactions, 98 2019 565.

International Presentation:

1. Y. Ma, Y. Cheng, Y. Inoue, T. Nagai, Y. Kuroda, K. Matsuzawa, S. Mitsushima, Y. Liu, Y. Wang, A. Ishihara, Titanium oxide nano-particles as supports of cathode catalysts for polymer electrolyte fuel cells, 236th ECS Meeting, #1150, 2019, Atlanta, GA, USA
2. Y. Ma, H. Kajima, Y. Shimasaki, T. Napporn, T. Nagai, Y. Kuroda, K. Matsuzawa, S. Mitsushima, A. Ishihara, Pt/TiO_x cathode catalysts for Polymer Electrolyte Fuel Cells, PRiME 2020 ECS Meeting, I01D-2296, 2020, Online

Domestic Presentation:

1. Y. Ma, H. Kajima, Y. Shimasaki, T. Nagai, Y. Kuroda, A. Ishihara, S. Mitsushima, Degradation analysis of Pt loading controlled Pt/Nb-Ti_4O_7 catalysts using arc plasma deposition, 電気化学会第 89 回大会, 1H20, 2022, 大阪, 日本